First realization of the EARISS principle : energy and angle resolved ion scattering spectroscopy

van der Meulen, Peter F.H.M.

Award date:
1988

Eindhoven University of Technology.
Department of Applied Physics.
Solid State Division.
Surface Physics Group.

First realization of the EARISS principle: Energy and Angle Resolved Ion Scattering Spectroscopy.

P.F.H.M. van der Meulen.
Masters Thesis.

University coaches:
Prof. Dr. H. H. Brongersma.
Ir. P.A.J. Ackermans.

Eindhoven May 1988.

Summary.

This masters thesis describes the first realization of Energy and Angle Resolved Ion Scattering Spectroscopy (EARISS). The EARISS apparatus uses noble gas ion beams to probe the outermost atomic layers of a surface. These ion beams cause damage to the structure and composition of the surface being studied. Therefore an efficient use of the backscattered ions should be made, thereby keeping the total ion dose as small as possible.

The EARISS analyzer accepts backscattered ions with a fixed scattering angle over a 320^{o} azimuthal angle. The detection system enables us to simultaneously determine the energy and the angle of a backscattered ion. We have shown that countrates of up to $4 \cdot 10^{5}$ detected ions per second may be handled. This means that an improvement of 2 to 4 orders of magnitude in the detection efficiency of the backscattered ions is possible. This enables the study of surfaces which are sensitive to radiation damage caused by the incident ion beam (semiconductors, polymers etc.).

This thesis deals with the difficulties we encountered during the first use of the sickle and ring detector, which is the heart of the detector for the energy and azimuth of the backscattered ions. Some solutions to these problems will be presented and further improvements of the detector will be discussed.

Dankwoord,

Op deze plaats wil ik graag iedereen bedanken die bijgedragen heeft aan de totstandkoming van dit afstudeerwerk.

Ten eerste zijn daar natuurlijk de mensen die in het afgelopen jaar de daadwerkelijke begeleiding op zich hebben genomen, Paul Ackermans, Hans Ottevanger en Hidde Brongersma. Zonder hun inzet en hulp waren we nog niet op de helft geweest van wat er het afgelopen jaar allemaal bereikt is. De vele discussies en het gezamenlijk oplossen van de gerezen problemen hebben geleid tot een leerzaam jaar, waarin toch de humor niet heeft ontbroken.

Vervolgens zijn daar natuurlijk alle mensen die in het eindstadium van het verslagleggen een zeer wezenlijke bijdrage hebben geleverd. De reusachtige tijdsdruk werd mede door de inzet van Rianne, Helga, Marcel, Martijn en Willem succesvol overwonnen.

De andere leden van de groep FOC hebben natuurlijk ook bijgedragen tot een plezierig jaar. Vooral het schilderen van het EARISS rek heeft bijgedragen tot de algemene hilariteit. Daarom wil ik vooral Bert bedanken voor zijn kundige supervisie in deze moeilijke periode.

Natuurlijk kan een zo omvangrijk apparaat als de EARISS niet gebouwd en bedreven worden zonder een kundige technische staf. Bij deze wil ik dan ook vooral Piet, Jos en Peer bedanken voor hun werk bij de CTD en Rien en Gerard voor het maken van allerlei mogelijke en onmogelijke zaken op en om het EARISS apparaat.

Voor het elektronische werk heeft de hulp van vooral van Rein, Freek en Coen veel voor het afstudeerwerk betekend.

Tenslotte wil ik mijn kamergenoot Camiel bedanken voor zijn inzet om toch nog de kleurenplaatjes op tijd in het verslag te krijgen.

Eindhoven 29-4-88, Peter van der Meulen.

Table of Contents.

Chapter 1. General Introduction.

1.1 Introduction

Along with the development of new techniques, surface studies have become of more importance to both the scientific community and researchers in industry. The objective is to get more insight in the phenomena related to surface and interface behaviour.

The properties of surfaces and interfaces can differ largely from the bulk properties. The reason for this lies essentially in the fact that surface atoms lack neighbours on one side. A piece of material freshly cut along a plane of atoms, will in general show three different effects on its newly formed surfaces. Firstly the atoms along the plane will be in a non-equilibrium state of higher energy. These atoms will tend to move to positions where they have less potential energy. This is called surface reconstruction. Secondly the outermost atomic layer may tend to move with respect to the second atomic layer. The interatomic layer distance will then change with respect to layer distances in the bulk. This effect is called surface relaxation. It can also occur for the layer separation between the second and the third atomic layer and sometimes even beyond that. Thirdly some atoms with large surface energies will try to migrate into the bulk, whereas atoms with a smaller surface energy will migrate from the bulk to the surface, thereby reducing the total surface energy. This is called surface segregation.

Segregation, relaxation and reconstruction indicate that both the physical and chemical properties of the surface may differ largely from the bulk. It is for this reason that the knowledge of surfaces and interfaces is important in many industrial and scientific applications, such as corrosion research, catalytic processes, chemical reactions, adhesion, friction, crystal growth, the development of new materials, semiconductor research, and lots of applications that deal basically with materials sticking together or with the prevention of materials sticking together.

1.2 Surface science and ultra high vacuum techniques

Surfaces are normally prepared and studied under carefully controlled circumstances. Freshly made surfaces can be very reactive due to an excess of surface energy. This implies that a fresh surface should not be in contact with air (oxydization) or other gases if the properties of the surface itself are to be studied. Surfaces are therefore mainly prepared and studied in ultra high vacuum systems. This is done in order to be able to study a surface without it getting contaminated during the investigation. At a background pressure of 10^{-4} Pa, and a sticking probability of 1 on a freshly formed surface, this surface would be contaminated with a monolayer of residual gas-atoms in one second. Therefore it should be clear that ultra high vacuum (UHV) systems are required with background pressures not exceeding 10^{-7} Pa. These UHV systems require special precautions and the use of selected materials. The materials are selected on their outgassing behaviour at low pressures. Some typical materials are: deoxydized copper, stainless steel, gold, platinum, quartz and some other ceramics as alumina.

All materials have to be bakeable up to at least 250^{o}C in order to remove contaminants and adsorbates. Repeated bakeout significantly reduces the background pressure in the system.

Most types of pumps used in UHV-systems are ion-getter pumps, titanium sublimation pumps and cryogenic pumps. All these types of pumps are based on the trapping of remaining atoms in or onto some surface.

A UHV-system also requires a sample introduction system together with sample cleaning facilities such as: ion guns for sputtering, heating of the sample for annealing, and the availability of special gases e.g. oxygen for surface oxidization.

1.3 Surface sensitive techniques

Although some surface sensitive techniques date as far back as the early 1920's - Low Energy Electron Diffraction (LEED) was developed in 1927 [1,2] -, the major breakthrough in surface analysis occured along with the development of UHV-systems in the late 1960's.

Most applied techniques are based on an incident beam of particles (neutrals, electrons, ions, photon's etc.) and on the detection of emitted or reflected particles, which could be any of the aforementioned ones. The surface sensitivity of a technique is determined by either the penetration depth of the incident particle or the escape depth of the secondary particle. Some examples of surface analyzing techniques will be described below.

A technique commonly used in surface composition analysis is Auger Electron Spectroscopy (AES, [3,4,5]). A narrow beam of electrons with energies of 1.5 to 2 keV is focussed onto a sample. Such an electron is able to remove another electron from one of the inner shells of an atom in the surface. The created vacancy can than be filled by another electron coming from one of the outer shells (fig. 1.1). The

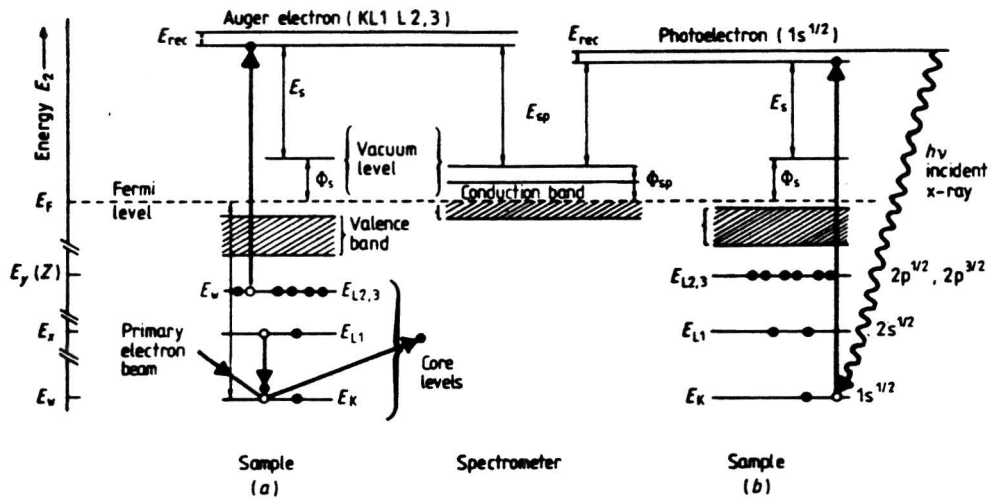

Fig. 1.1. Schematic representation of the energy levels involved in (a) the Auger process and (b) the photoelectron emission process.

transition energy that is released during this process can be absorbed by another electron in the outer shell which will then be emitted from the atom. The kinetic energy of this last electron can be measured. Since this transition is characteristic for the element it was emitted from, it is possible to obtain a quantitative analysis of the surface composition. Closely related to AES is a technique called X-ray Photoelectron Spectroscopy (XPS, also Electron Spectroscopy for Chemical Analysis, ESCA [6,7,8,9]). A soft X-ray source (usually Mg-Kα or Al-Kα) is used to illuminate the substrate. The energy of the incident photons (1 - 1.5 keV) is used to free an electron from one of the inner shells of a substrate atom (fig. 1.1). The energy of the

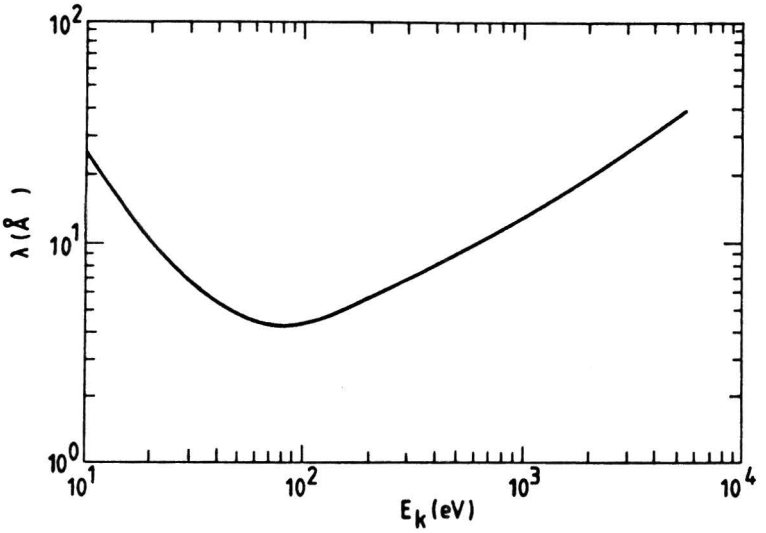

Fig. 1.2. The electron inelastic mean free path in solids as a function of the electron energy. The figure represents an empirical fit for a large set of elements.

emitted electrons is directly related to their previous binding energy and to the energy of the incident photons. By analyzing the energy spectrum of the emitted electrons it is possible to determine the surface composition. Both AES and XPS are surface sensitive due to the fact that the escape depth of the analyzed secondary electrons is about 5 to 10 monolayers (1-2 nm, fig. 1.2).

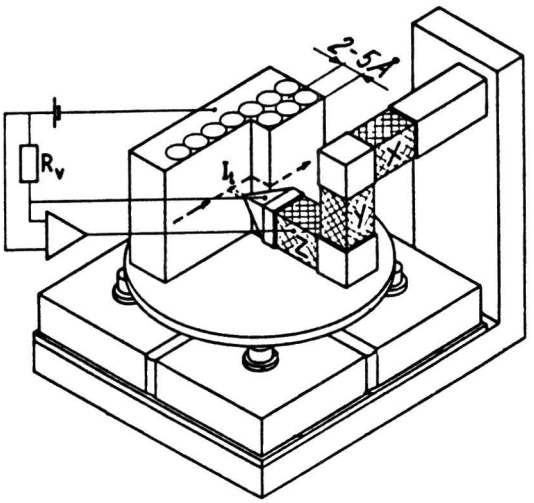

Fig. 1.3. Principle of the scanning tunneling microscope. The tip is brought close to the surface (5Å) by using piezocrystal Z.

A far more recently developed technique is the Scanning Tunneling Microscope (STM, [10,11,12,13]). In this apparatus a very fine tungsten tip is held at a very close distance above a sample (fig. 1.3). When a small voltage is applied across the gap between the tip and the sample a quantummechanical tunnel current through the gap can be observed. The tunnel current varies exponentially with the distance between the tip and the surface. The distance between the tip and the surface atoms can be measured by moving the tip in a lateral direction over the surface thereby keeping the current through the gap constant. The distance can be calculated from the movement which the tip has to make in the z-direction in order to keep the tunnel current constant .

Other common surface analysis techniques make use of ion beams as a primary sources. Both the scattered ions (Ion Scattering Spectrometry, ISS) and sputtered secondary ions (Secondary Ion Mass Spectrometry, SIMS [14,15,16] can be detected. SIMS has been found to have high sensitivity and excellent separation power, however the extremely large differences in sputtered ion yield (over 5 orders of magnitude) and the lack of simple quantitative models make quantification a serious problem.

In ISS three energy regimes can be observed. The low energy region with primary ion energies up to 10 keV is used to probe the outermost atomic layers (LEIS). Medium energy range (MEIS), (10-100 keV) ion-scatterers use channeling and blocking effects to investigate deeper layers of single crystals. In High Energy Ion Scattering (HEIS) mostly H^+ and He^+ ions with energies up to a few MeV are used. These ions penetrate up to 1 μm depth into the sample, which means that this technique is more often used to study interfaces or buried implants of materials.

1.4 Purpose of the work done for this Masters Thesis

In the past few years a novel type of LEIS-apparatus has been developed in the Surface Physics Group of the Eindhoven University of Technology. This Energy and Angle Resolved Ion Scattering Spectrometer (EARISS) is designed to measure simultaneously the surface composition and the surface structure of a sample. Different parts of the apparatus have been shown to function according to our expectations in

the last few years. The purpose for this work was to show that the combined parts of the apparatus function as an integrated system and can be used for the aforementioned analysis. In the next chapter a short introduction to low energy ion scattering will be given. Thereafter we will discuss the concepts and ideas of the EARISS. In chapter 4 we will discuss in more detail the heart of the ion detection system: the microchannel plates. Chapter 5 deals with the two dimensional detection system itself. In chapter 6 we discuss the signal transmission and the analog electrical circuit. Chapter 7 treats the digitization of the measured signals and the subsequent data processing. In chapter 8 we will discuss the first measurements to be performed on the EARISS apparatus. Chapter 9 finally deals with some suggested improvements which will have to be made for better performance and to be able to start actual surface studies.

1.5 References

[1] **C. Davisson and L.H. Germer**, Phys. Rev. 30 (1927) 705.

[2] **H.E. Farnsworth**, Phys. Rev. 33 (1929) 1068.

[3] **H.W. Werner and R.P.H. Garten**, Rep. Prog. Phys. 47 (1984) 221.

[4] **H. Hatsche**, Microscopica Acta 87 (1983) 97.

[5] **S. Hofmann**, Wilson & Wilson's Comprehensive Analytical Chemistry, Vol IX, ed. G. Svehla, Elsevier, Amsterdam (1979) 89.

[6] **D. Briggs**, Electron Spectroscopy, Theory, Techniques and Applications, Vol III, ed. C.R. Brundle and A.D. Baker New York, Academic Press (1979) 305.

[7] **C.J. Powell et al.**, J. El. Spec. Rel. Phen. 17 (1982) 361.

[8] **C.D. Wagner et al.**, Handbook of Photoelectron Spectra, Edin Prairie MN, Perkin Elmer Co. (1978).

[9] **R. Kelly**, Radiation Effects 80 (1984) 273.

[10] **G. Binnig et al.**, Phys. Helvetica Acta 55 (1983) 726.

[11] **G. Binnig and H. Rohrer**, Surf. Sci. 126 (1983) 236.

[12] **G. Binnig et al.**, Phys. Rev. Lett. 56 (1986) 930.

[13] **C.F. Coate**, Physics Today, august (1986) 26.

[14] **H.W. Werner**, Surf. Int. Anal. 2 (1980) 56.

[15] **E. Zinner**, J. Electrochem. Soc. 130 (1983) 199 C

[16] **C.H. Morrison**, Secondary Ion Mass Spectrometry SIMS III, Proc. 3rd Int. Conf. Budapest 1981, Ed. A Benninghoven et al., Berlin, Springer Verlag (1982) 244.

Chapter 2. Low Energy Ion Scattering (LEIS).

2.1 *Introduction*

In a typical Low Energy Ion Scattering (LEIS) experiment (fig. 2.1) noble gas atoms (usually Ne^+, He^+ or Ar^+) hit a surface. The reflected ions are detected and their energy is analyzed. The measured energies are directly related to the masses of the surface atoms whereas the intensities relate to the atomic abundancies in the first atomic layer.

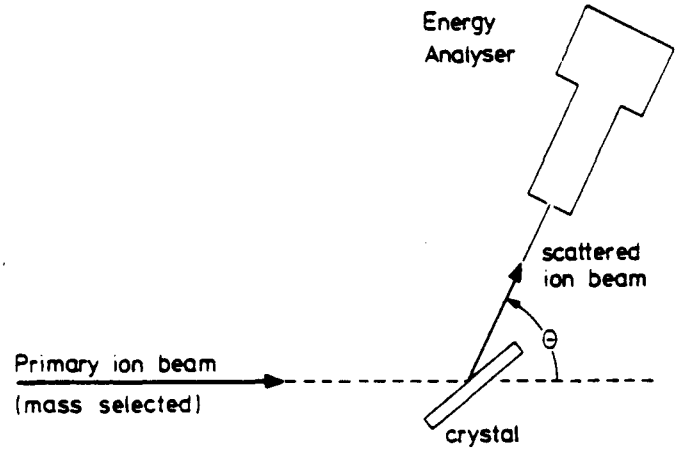

Fig. 2.1. Principle setup of a scattering experiment.

When an ion hits a surface several processes can occur. Firstly the ion can penetrate into the sub-surface layers where it can lose its kinetic energy by multiple scattering from atoms. One or more of these atoms can than be emitted from the surface. This effect is called sputtering. It always occurs in ion beam experiments. Secondly, the incident ion can be reflected from one of the surface atoms (fig. 2.2). This is called (back-) scattering. The scattering process can be understood in terms of a classical, elastic collision [1,2]. This will be explained in the next section.

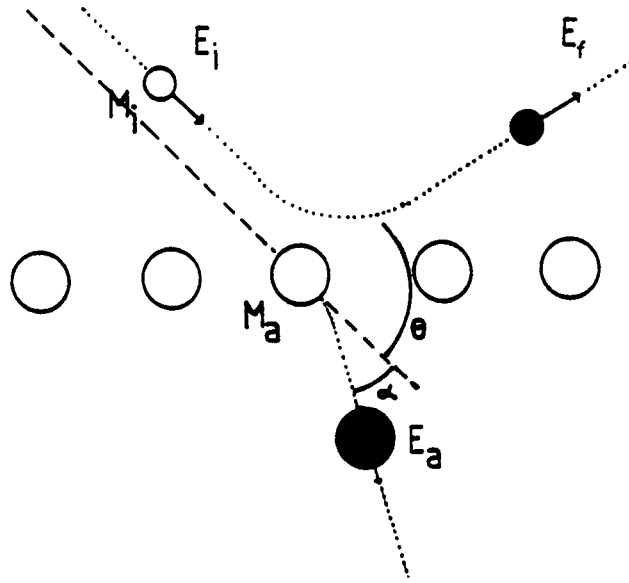

Fig. 2.2. Scattering of a noble gas atom (Energy E_1, mass M_i) from a surface atom (Mass M_a). The ion is scattered over an angle θ with a final energy E_f.

The scattering of an ion from a surface atom is caused by the nucleus-nucleus repulsive forces. The electron-configuration of the particle plays an important role in the neutralization process which we will discuss in paragraph 2.3. Most incident ions (> 99 %) will be neutralized at the surface. This means that scattered-ion yields are usually low. Ions scattered from the second or even deeper atomic layers have an even higher neutralization probability due to the fact that the time they spend in, or near the surface is much longer. It is this neutralization probability which makes LEIS a surface sensitive technique.

2.2 *Theoretical background*

The de Broglie wavelength of ions in the energy range of 1 keV is approximately in the order of $2 \cdot 10^{-13}$ m. This is much smaller than the interatomic distance in solids which usually lies around $2 \cdot 10^{-10}$ m. The consequence of this difference is that diffraction effects play no substantial role in the scattering process. The scattering of an ion

from a surface atom can in essence be understood in terms of an elastic two-particle interaction (binary collision). The nucleus-nucleus repulsive Coulomb-force is dominant in the scattering process. The electron configuration of the incident ion and the surface atom is not an important contribution to the elastic energy-loss of the scattered ion, but it does play a dominant role in the neutralization process.

It can be assumed that surface atoms are at rest during the collision with an ion. This is because the time associated with thermal vibrations of surface atoms (10^{-13} s) is much longer than the interaction time (10^{-15} s) associated with the collision process. It is only at low incident ion energies (< 100 eV) that the two become comparable. Furthermore, the thermal vibration energy is low compared to the incident ion energy (1...10 keV). At 1000 K temperature of the sample, the vibrational energy of the surface atoms is about 10 eV.

The ion-atom collision can now be treated as an elastic, two particle process with the target-particle initially at rest. Using the classical laws of conservation of energy and momentum we can obtain the following expression (fig 2.2):

$$\frac{E_f}{E_i} = \frac{\left[\cos\theta \pm \sqrt{(M_a/M_i) - \sin^2\theta}\right]^2}{(1 + M_a/M_i)^2} \qquad (2.1)$$

Where E is the ion energy, M is the atomic mass and θ is the scattering angle. The subscript i denotes energy of the incident ion and the subscript f denotes the final ion energy after scattering from the surface atom.

In expression (2.1) the + sign should be used for $M_a > M_i$ and the minus sign for $M_a \leq M_i$, provided that $(M_a/M_i)^2 > \sin^2\theta$. From (2.1) it is obvious that the energy of the scattered ions is directly related to the atomic mass of the surface atoms provided that E_f, M_i and θ are known. In our experiments we have a fixed scattering angle of $\theta = 145^\circ$, M_i is very often the atomic mass of Ne^+ (20) and the spread ΔE_i is a usually a few percent of the primary energy E_i.

Inelastic energy losses are caused by direct energy transfer of the incident ions to the electrons of the surface-atoms by electron-electron collisions, or by excitation of electrons or even by ionisation of either the surface atoms or the incident ions. Because of the large mass difference of the nucleii compared to an electron mass, the movement of nuclei and electrons can be described separately. As we discussed above this means that the movement of the nuclei can be treated classically whereas the movement of the electrons should be considered quantum-mechanically. This leads to a formalism in which the ion approaches the atom, their electron clouds penetrate in each other and, depending on the distance of closest approach, one or more electrons interact.

The description of the interaction potential of the ion-atom collision is based on the differential equation given by Thomas and Fermi [3]. This differential equation can only be solved numerically, reason why several authors have tried an analytical approach. One of them is Molière [4], whose approximation is essentially based on the Coulomb-potential between two charged particles corrected by a correction factor. Another approach was made by Firsov [5], who used the same Coulomb-potential corrected by a screening function for a correction of the nuclear screening by the electron cloud.

Thermal vibrations and inelastic energy losses are not yet fully understood. Both effects lead to broader peaks in the LEIS-spectra, whereas inelastic energy-losses may also lead to a shift in the energy spectrum.

2.3 *Neutralization*

The quantification of LEIS-spectra, and thus the determination of atomic abundancies in the first monolayer, is complicated by two effects: neutralization and the scattering cross-section. The scattered ion yield Y^+ is given by:

$$Y^+ = Y\ P^+ \qquad (2.2)$$

In this expression Y is the scattering yield of the primary ions at the target atoms and P^+ is the corresponding ion fraction of scattered

particles: $P^+ = 1 - P_n$, where P_n is the neutralization probability. Both Y and P^+ depend on the ion-target combination under study. Y can be calculated from the scattering cross section σ by using:

$$Y \doteq \sigma(M_i, M_a, E_i, \theta, ...) \qquad (2.3)$$

The scattering cross-section σ can be calculated on the basis of a repulsive, screened Coulomb potential (e.g. the Thomas-Fermi-Molière approximation combined with a Firsov screening function as mentioned in the previous section).

Since $Y \div Z_a$ and $P^+ \div 1/Z_a$ (Z_a being the atom-number of the target atom), the scattered ion yield $Y^+ = YP^+$ is approximately constant [6], with Z_a. In a first order approximation the scattering cross-section σ will vary with $\sin^{-4}(\theta/2)$ [7].

The neutralization process can be seen as an Auger neutralization. An electron of the target atom neutralizes the ion and a second electron can absorb the transition energy and be emitted. The effect is that inelastic energy-losses occur. The probability of an electron-transfer from the atom to the ion, decreases exponentially with the ion-atom distance, and it also depends on the time the two electron clouds overlap. Analogous to the law of Lambert-Behr in classical optics we can define an expression for the neutralization probability P^+:

$$P^+ = A \exp(-v_o/v_=) \qquad (2.4)$$

where $v_=$ is the velocity of the ion parallel to the surface and v_o is a scaling velocity dependent on the ion-atom system. The high neutralization probability P^+ and the short mean free path $\lambda = 10^{-4}$ nm of the ion in the solid, result in an extreme monolayer sensitivity with a detection limit of 10^{-3} of a monolayer. This extreme surface sensitivity can be alliviated by the use of alkali ions [8], which is often done in order to be able to study the structure of the second and even the third monolayer.

2.4 *Surface structure information*

When we study the first monolayer of a crystal, using LEIS, we can obtain information about the surface composition as we have seen above. Besides this compositional information it is also possible to obtain information on the surface structure by making use of effects as shadowing and double collisions. These effects will be described below.

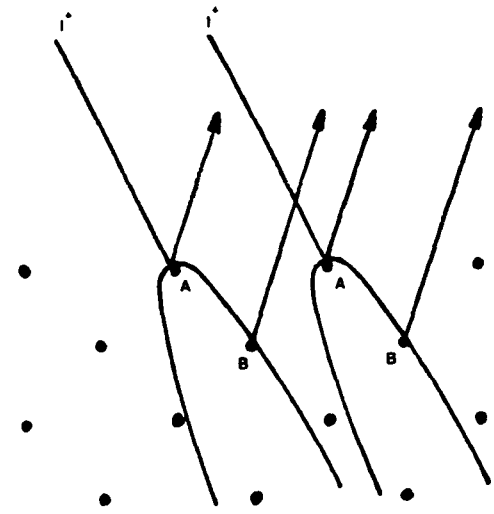

Fig. 2.3. Each atom has a shadow cone: a region in which no ions can penetrate. If the incident angle is such that the atoms B lie in the shadow cone of the atoms A, then no scattering from B is detected. An enhanced intensity on the edge of the shadow cone makes double collisions detectable (fig 2.5).

Shadowing occurs when incident ions can collide with two different atoms (A and B) in a surface (fig. 2.3). Every atom has its own shadow cone in which region no ions can penetrate. If we rotate the surface and choose the right incident angle in order that the atoms B are in the shadow cone of the atoms A, it is no longer possible to detect ions scattered from atoms B. Brongersma and Buck [9] have studied this effect for a Ni(001) crystal with a S c(2 x 2) surface layer (fig. 2.4 a,b). In the <110> direction no shadowing of Ni-atoms occurs, whereas

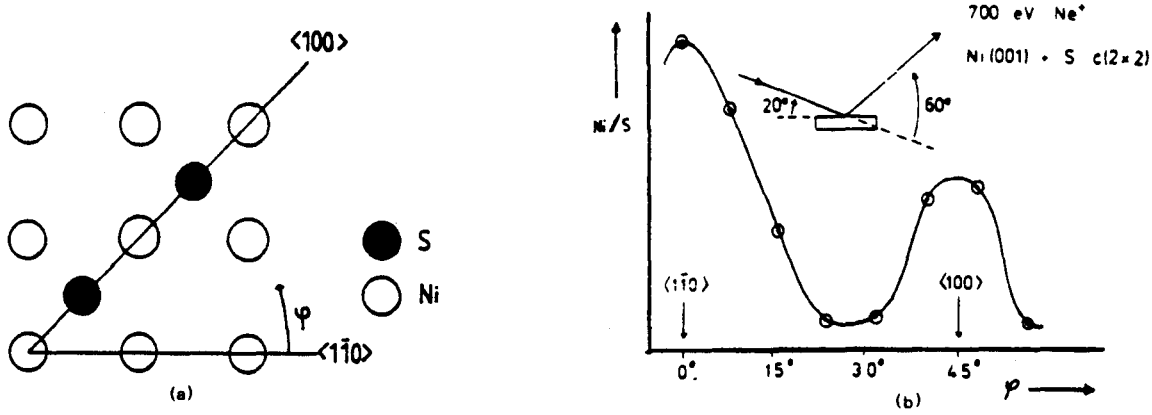

Fig. 2.4.a. Structure of the Ni (001) + S c(2x2) surface. The sulphur atoms are located .12 nm above the first nickle layer.

Fig. 2.4.b. Ratio of the intensities of the Ni- and S-signal as a function of the azimuthal angle φ. The angle of incidence and the scattering angle are fixed.

in the <100> direction the Ni-peak disappears due to the shadowing of the Ni-atoms by the sulphur atoms in the top layer.

Another effect that occurs when using shadowing effects is the focussing of ions along the edge of the shadow cone (fig. 2.5). The ion intensity at this edge will be higher than the intensity

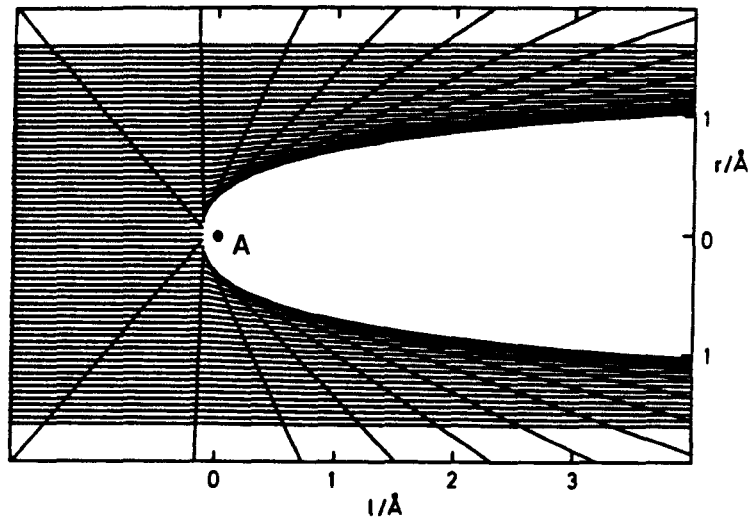

Fig. 2.5. Trajectories of incident and scattered ions at the scattering atom A. The enhanced ion intensities are found at the edge of the shadow cone.

elsewhere. This focussing effect can be used to enhance the intensity of primary ions onto a second atom (B) in order to obtain double collisions (fig 2.6.a), or blocking effects (fig 2.6.b).

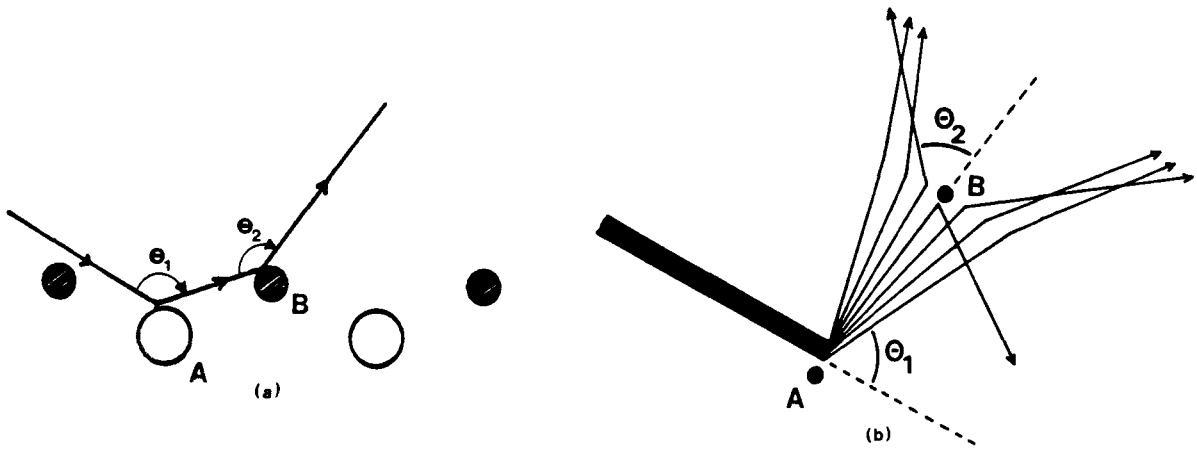

Fig. 2.6.a. Schematic representation of a double collision at a surface. The sum of the scattering angles θ_1 and θ_2 is equal to the angle between the primary ion beam and the detector.

Fig. 2.6.b. Schematic representation of the blocking of ions scattered from atom A by atom B. No ions scattered from A will be detected.

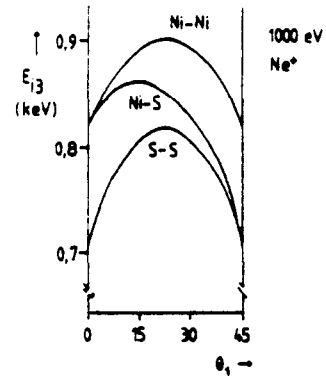

Fig. 2.7. Intensity maxima for double collisions as a function of the second scattering angle θ_2 at a Ni-S surface. The total scattering angle $\theta_1+\theta_2$ was 45^o.

These double collisions are the second effect that can be used in order to obtain structural information (fig. 2.7). If inelastic energy losses are negligible, it is possible to use (2.1) for each individual collision. At a fixed angle between ion-source and detector it is now possible to vary the angle of the incident ion beam by rotating the sample, thereby varying the ratio of the scattering angles θ_1 and θ_2

(fig. 2.6.a). The intensity maxima for the different double collisions that are possible (A-A, A-B, B-B, fig. 2.7), show at what position the atoms A and B are located. Despite of the fact that double collisions have very high neutralization probabilities, we can study them by making use of focussing and small scattering angles. The scattering cross-section varies with $\sin^{-4}(\theta/2)$ (§2.3) so that the gain in cross-section at small scattering angles θ more or less balances the loss due to neutralization (2.4), which is caused by the larger parallel velocity $v_{=}$.

2.5 *Mass resolution*

Experimental LEIS-spectra will always show broadened peaks, due to effects in the used ion source, the scattering process at the surface and energy analyzer imperfections. If we use a perfectly parallel, mono-energetic ion beam and a perfect energy analyzer, all contributions to peak-broadening will arise from inelastic energy losses and thermal vibrations (§2.3).

The question whether atomic masses M_a and $M_a + \Delta M_a$ can still be separated if we do neglect inelastic effects and thermal vibrations, largely depends on the scattering angle θ and the mass-ratio M_a/M_i. From 2.1 we deduct:

$$\frac{\Delta E_f}{\Delta M_a} = \frac{E_f}{M_a} \cdot \frac{2(M_a/M_i)}{M_a/M_i + 1} \cdot \frac{M_a/M_i + \sin^2\theta - \cos\theta\sqrt{(M_a/M_i)^2 - \sin^2\theta}}{(M_a/M_i)^2 - \sin^2\theta + \cos\theta\sqrt{(M_a/M_i)^2 - \sin^2\theta}} \qquad (2.5)$$

Hellings [10] has shown that an optimum mass resolution is obtained for relatively large scattering angles ($\theta > 135^{\circ}$) and small (but not extremely small) values of the mass-ratio M_a/M_i. A larger scattering angle has the disadvantage that the scattering cross-section decreases, thus the scattered ion yield will be lower.

2.6 *Practical aspects, LEIS and EARISS*

As mentioned above LEIS has the disadvantage of high

neutralization of primary ions at the surface. Thus scattered ion

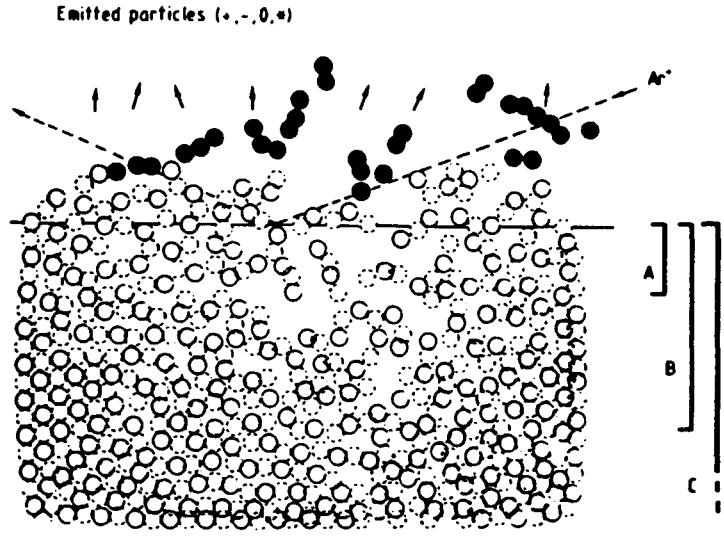

Fig. 2.8. Energy transfer in a scattering process. The incident Ar^+ ion will disturb the atomic order in the surface region. Sputtered atoms (Black dots) receive enough energy to be emitted from surface region A. Large dislocations occur in region B, whereas reversible lattice disorder occurs in region C.

yields are relatively low. Another unwanted effect is sputtering (§2.1) (fig. 2.8). This causes damage to the surface, and structural information can be lost. Sputtering yields can also differ for different elements [11,12], which makes quantification a serious problem.

It can be concluded on these arguments that a low primary ion dose is necessary, which implies that we have to make an efficient use of scattered ions. Energy and Angle Resolved Ion Scattering Spectroscopy (EARISS) offers this possibility. Most conventional LEIS-apparatuses have an ion detector with a small opening angle [10], and an electrostatic energy analyzer which is only able to detect one energy at a time. This means that energy scans have to be collected at several positions of the sample, thus implying long measuring times and comparatively high ion beam damage.

The EARISS-apparatus (or simply EARISS) has a nearly full azimuthal opening (320^o) and it has an energy analyzer that does not necessarily require scanning of the energy spectrum. This means that ions of one fixed scattering angle are effectively collected over a nearly full azimuth and their energy is analyzed at the same instant, thus diminishing measuring times by about 4 orders of magnitude.

Effectively we could speak of the EARISS detector having 10,000 conventional ion detectors, if we determine the resolution in both the angular and the energy to be 1%. This results in low damage conditions whereas the usual LEIS-advantages such as very high surface sensitivity, a simple mass identification and structural information by use of shadowing or double collisions are still part of the technique. The EARISS apparatus will be discussed in the next chapter.

2.7 References

[1] **H.H. Brongersma**, J. Vac. Sci. Techn. 11 (1974) 231.

[2] **E.S. Mashkova and V.A. Molchanov**, Medium Energy Ion Reflections from Solids, North Holland Publishing, Amsterdam (1985).

[3] **I.M. Torrens**, Interatomic Potentials, Academic Press, London (1972).

[4] **G. Molière**, Zeitschrift für Naturforschung 20 (1947) 133.

[5] **O.B. Firsov**, Soviet Physics JETP 6 (1958) 534.

[6] **H.H. Brongersma and T.M. Buck**, Nucl. Instr. Meth. 132 (1976) 559.

[7] **H.A. Enge et al.** Introduction to Atomic Physics, Addison Wesley, London (1974).

[8] **E. Taglauer and W. Heiland**, Inelastic particle-surface collisions, Proc. 3rd workshop Feldkirchen-Westerham, Springer-Verlag, Berlin (1980).

[9] **H.H. Brongersma and T.M. Buck**, Nucl. Instr. Meth. 149 (1978) 149.

[10] **G.J.A. Hellings**, Energy and Angle Resolved Ion Scattering Spectroscopy. Ph. D. Thesis, Eindhoven (1986).

[11] **E. Zinner**, J. Electrochem. Soc. 130 (1983) 199C.

[12] **M.P. Seah**, Surf. Int. Anal. 2 (1980) 222.

Chapter 3. The EARISS-apparatus.

3.1 *Introduction*

The Energy and Angle Resolved Ion Scattering Spectrometer EARISS was developed in recent years at the Eindhoven University of Technology in the Surface Physics Group. Its purpose was to improve the detection efficiency of conventional LEIS apparatuses, by making a more efficient use of the scattered ions. Its energy analyzer and detection system are constructed in such a way that the detection of energy and azimuthal distributions is possible simultaneously, thus eliminating the need for energy scans and target rotation. This results in low damage conditions during the experiments.

EARISS uses a fixed scattering angle of $\theta = 145^{o}$ when the central ion source is used (§3.3). The azimuthal opening of the analyzer is about 320^{o} (§3.4). This means that a cone of scattered ions is accepted by the analyzer. The detector/analyzer system determines both the azimuthal angle and the energy of the scattered ions. In this way mass- and structural information of the sample being studied, are collected at the same time. In the next paragraphs we will discuss the location of all components in the vacuum system (§3.2), the central ion source (§3.3), the energy analyzer (§3.4) and the detection system (§3.5).

3.2 *The vacuum system*

A UHV system for surface analysis will usually contain different analyzing and preparation techniques mounted on one central UHV-chamber.

The EARISS-apparatus (fig. 3.1.a,b) does have several of these features. The central vacuum chamber is constructed as a sphere in order to facilitate the access of different techniques to the surface of the sample which is placed at its center. The target is placed on a manipulator which allows translation along the x, y and z axis and two rotations: one around the y-axis and one around the z-axis. The central ion source is placed at the top of the central vacuum chamber. It is capable of producing He^{+}, Ne^{+} and Ar^{+} ion beams (an alkali-ion

source will be installed in the future). A sputter ion gun allows the in situ cleaning and depth profiling of the sample. The sample can be heated up to 800°C for annealing purposes. The result of the cleaning of the sample can be studied using the LEED-apparatus situated on the left of the vacuum chamber (fig. 3.1.b). Along the y-axis we have a sample introduction system which is used to transfer

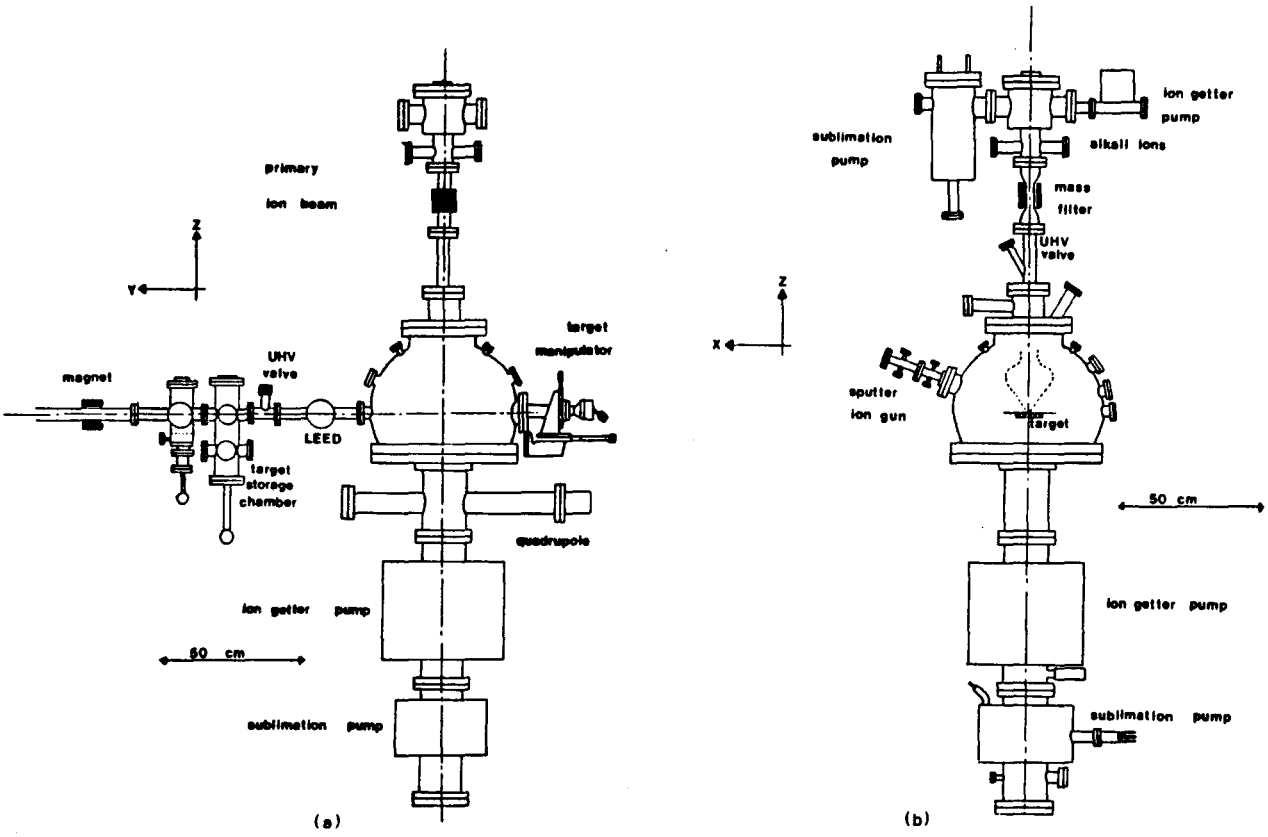

Fig. 3.1.a. The EARISS-apparatus. The primary ion source is located at the top of the central vacuum chambers. The target can be translated and rotated using the manipulator. The target introduction system is located on the left.

Fig. 3.1.b. The EARISS apparatus. The figure shows the location of the sputter ion gun and the target. The analyzer is shown with a dotted line.

samples into the vacuum system. It is possible to store several samples in a separate storage chamber.

The quadrupole mass analyzer which is located below the central

vacuum chamber is used to obtain a mass-spectrum of the residual gases.

Not shown in this picture are the gas-inlets for reactive gases meant to oxidize the surface or adsorb monolayers of a gas. The system is pumped by several ion getter pumps and a few titanium sublimation pumps which have LN_2-cooled screens.

In the future several other surface sensitive techniques will be mounted in other vacuum chambers which will then be interconnected to this system. These chambers will contain facilities for Spot Profile Analyzing (SPA-LEED), Reflected High Energy Electron Diffraction (RHEED) and ellipsometry. On the right of figure 3.1.a a Time Of Flight (TOF) analyzer will be installed which will be operational in the near future.

3.3 *The central ion source*

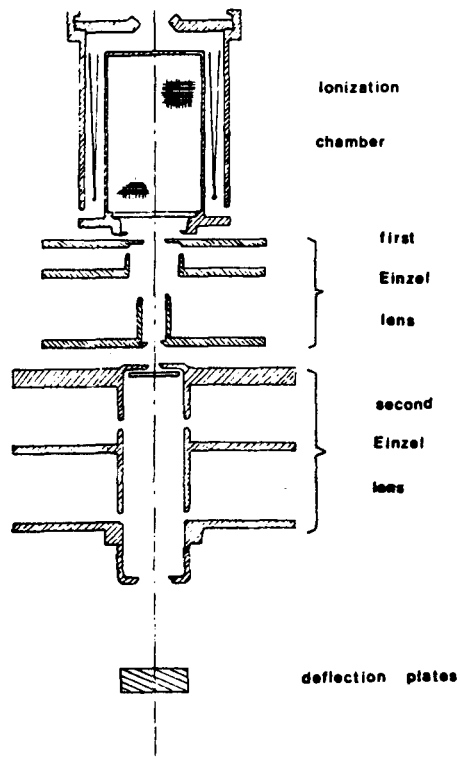

Fig. 3.2. The central ion source. The ionization chamber contains a set of filaments around a cilindrical grid. The ions produced inside the grid are extracted by the first Einzel lens. They pass through the second Einzel lens and a set of deflection plates.

The energy spread of the peaks in the scattered ion energy spectrum depends largely on the quality of the central ion source. Primary ions (He^+, Ne^+ or Ar^+) are produced in an ionization chamber containing the appropriate gas at a pressure of 10^{-4} to 10^{-2} Pa. Ions are produced by accelerating electrons from a filament (fig. 3.2) through a cylincrical metal grid. The electrons have enough kinetic energy to ionize the gas inside the metal grid. These ions are then extracted and focussed by the first Einzel lens. Next the ions are focussed by a second Einzel lens, after which they pass a set of lateral deflection plates. These are used to deflect the ions slightly into the direction of the sample. The ionization chamber, the extraction plate and the first Einzel lens are at a high potential corresponding to the ion energy. The other lenses are at a low potential.

The ion beam is then mass-seperated by a Wien filter (not shown). This filter consists of crossed magnetic and electrostatic fields which eliminate charged particles in the beam with another mass to charge ratio than the desired one. The mass separation $\Delta M_i/M_i$ is about 10%. Following the mass-filter there is an aperture with a variable opening size (openings of 0.3, 1 and 3 mm). After that the ions pass through two more Einzel lenses and four deflection plates. These lenses and deflection plates determine the spotsize and spotlocation on the sample surface. The energy spread was measured to be relatively low ($\Delta E/E \leq 1\%$). Due to the number of filters and lenses, the beam intensities are rather low ($\approx$ 100 nA at 3 keV Ne^+). As a consequence a sputter Ar^+-ion gun is needed to clean and profile the surface (§3.2).

3.4 *The energy analyzer*

Ions coming from the central ion source hit the target surface at a normal incidence. Ions will be backscattered in a 2π solid angle. The ions scattered over 145° can be accepted by the entrance slits of the energy analyzer (fig. 3.3). These slits have a circular shape. They will accept all ions over a full 360° azimuthal range. The second slit has three 2° holes in it. These holes are needed to support the

inner part of the energy analyzer. Since the ion beam can not be focussed infinitely sharp, there will always be some ions having a small radial velocity. This leads to spiralling tracks in the slit/analyzer system. In the future these tracks will be eliminated by the azimuth selector. This selector intercepts ions with too large azimuthal velocities. Hellings [1] has shown that either the size of the primary ion beam should be kept below 0.5 mm diameter, or an azimuth selector should be used. This selector will consist of a set of thin plates with narrow slits in a radial direction. Up to five plates will be placed accurately behind each other in order to insure the selection of ions moving in the same meridian plane. Spiralling ions may effect the azimuthal angular resolution but they will have no significant effect on the energy resolution

If the slits are nearly closed, the spread in the scattering angle will be quite limited. This means that the spot on the target from where we detect backscattered ions will be very small. If this spot coincides with the ion beam center, spiraling ion tracks will be kept to a minimum.

After the ions have passed the second slit, they pass through an electrostatic zoomlens [2,3]. This lens has two functions. Firstly it can focus the ions on the entrance of the analyzer system. Secondly it can accelerate or decelerate ions in the direction of their movement, thereby changing their energy. The zoomlens consists of five elements. The first is held at a ground potential. The second and third elements are mainly used for focussing purposes. The fourth element is used to accelerate or decelerate the ions. The last element is a so called Herzog element. It is used to reduce fringing fields at the analyzer entrance. Its potential is always the same as that of the fourth element: the two are interconnected. The zoomlens is mostly used to vary the entrance energy of the analyzer, thereby selecting a part of the energy spectrum. An ion coming from the target with an energy E_f which passes through the zoom lens with a potential V_3 on the last section of the lens (elements four and five) will enter the analyzer with an energy E_a:

$$E_a = E_f - qV_3 \qquad (3.1)$$

Where q is the charge of the ion (usually equal to the elementary charge e = 1.6 10^{-19}C), and V_3 is negative when positive ions are accelerated in the zoomlens.

The real energy selection is done in the double toroidal energy analyzer (fig. 3.3) [1]. It consists of four segments which are sections of a torus. Plates A and B deflect the ions towards the central axis of the analyzer. Plates C and D deflect the ions into a paraxial track and focus them onto the detector.

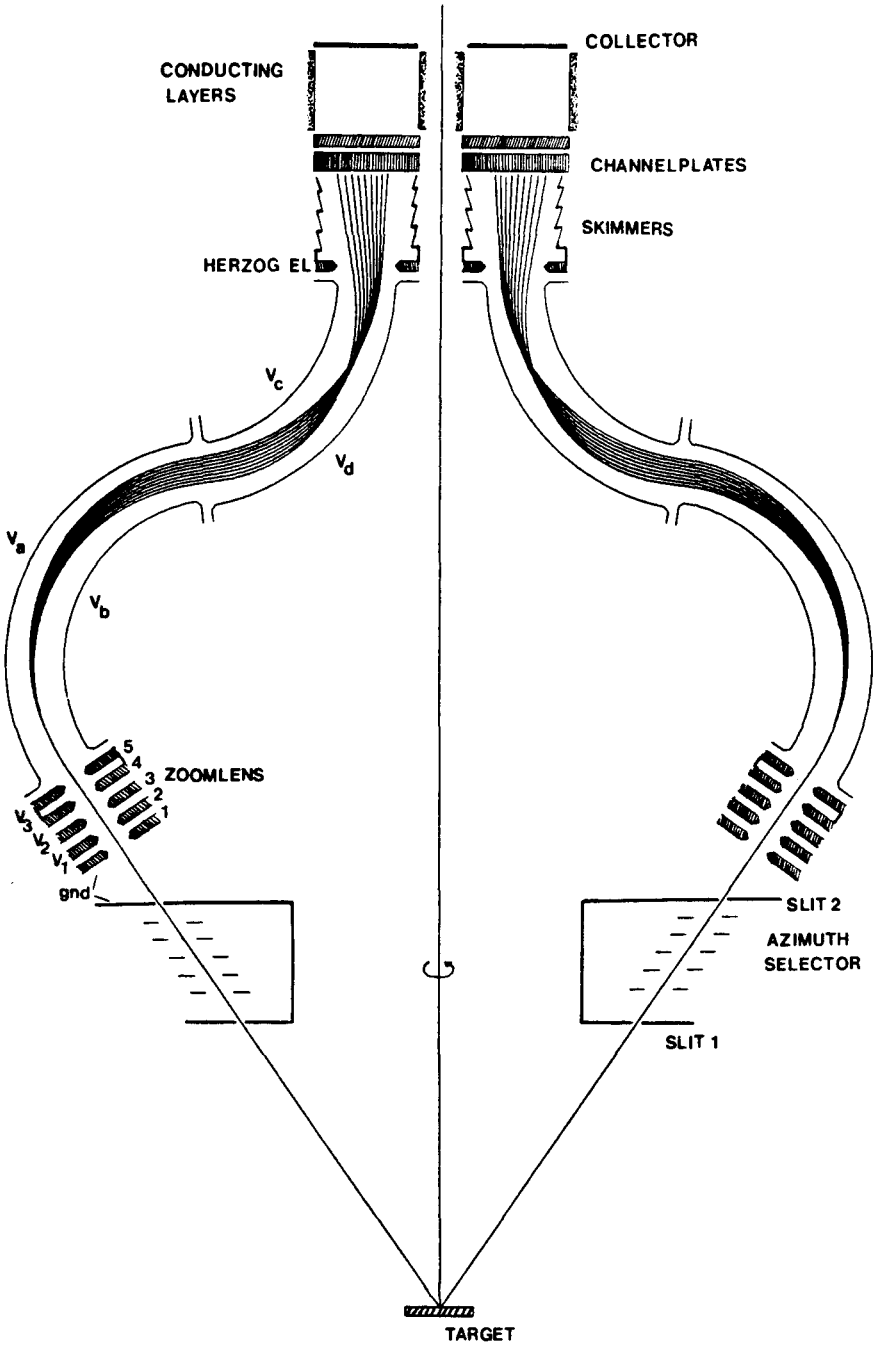

Fig. 3.3. The zoomlens and analyzer of the EARISS apparatus. Backscattered ions pass through the slits and the azimuth selector (not installed yet) after that they are focussed and accelerated in the zoomlens. Their energy is distributed radially over the first channel plate by the analyzer elements a, b, c and d. The Hertzorg element reduces fringing fields. The skimmers capture ions leaving the analyzer at too large angles. The channel plates produce an electron cloud for each ion. This electron cloud is postaccelerated towards the collector where its point of impact is measured. The gap between the second MCP and the collector is flanked by the inner and outer conducting layers.

The energy analyzer is calculated and constructed in such a way that only those ions in a small energy spectrum δ_E around a central pass-energy E_p will hit the detector. Ions entering the analyzer with an energy E_a (3.1) will come out of the analyzer if:

$$E_p - \delta_E \leq E_a \leq E_p + \delta_E \qquad (3.2)$$

Where δ_E is about 6%.

The potentials on the plates are related to the potential V_3 on the last zoomlens plate. The potentials on the analyzer plates should now be set as follows [1]:

$$\begin{aligned} V_a &= 2E_p * 0.13853 \\ V_b &= -2E_p * 0.17069 \\ V_c &= -2E_p * 0.13672 \\ V_d &= -2E_p * 0.17574 \end{aligned} \qquad (3.3)$$

Where all potentials are relative to V_3.

By scanning the potential V_3 we are able to scan the energy spectrum (the pass energy E_p is constant). Ions with a larger energy will not be deflected as much in the analyzer as ions with a lower energy. This means that the energy of the ions is converted to a radial energy distribution at the end of the analyzer, with high energy ions coming close to the axis of the detector and low energy ions coming close to the outer edge of the detector.

At the end of the analyzer sections we have mounted another Herzog element which has the potential as V_3, plus or minus 200V. The ions travel a short distance (field free region) before they reach the detector. This region is bounded by skimmers which capture all ions leaving the analyzer with too large deflection angles. This skimmers are connected to the Einzel lens. In figure 3.4.a,b the deflection plates and the zoomlens are clearly visible.

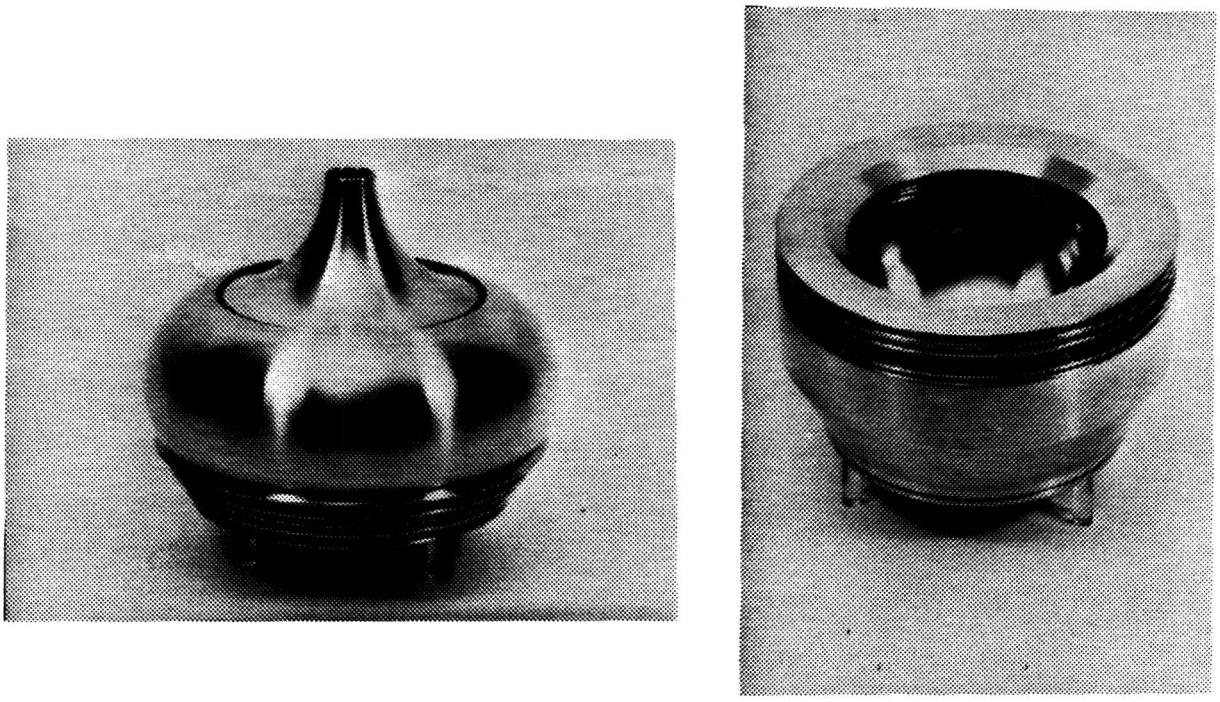

Fig. 3.4.a,b. The toroidal analyzer segments and the elements of the zoomlens.

3.5 *The detection system*

As we have discussed in the last section, the energy analyzer converts the energy spread of the ions in a radial distribution. This means that, when the exact location of each incoming ion on the detector is measured, we will have an energy distribution in the radial direction and an azimuthal distribution as a one to one projection of the structure of the sample surface.

The function of the detection system is now to determine for each ion its exact point of impact. This has to be done at a very high countrate ($> 10^5$ counts/s) in order to make full use of the detection efficiency. The detector assembly (fig. 3.5) consists of a set of microchannel plates (Chapter 4) and a charge collector (Chapter 5). The channel plates are sensitive to ion impacts. They produce an electron cloud ($\simeq 10^6$ electrons) for each incident ion. The electron cloud falls onto the charge collector where strip sets determine its center. The measured center of the charge cloud corresponds to the point of impact of the ions on the first channel plate.

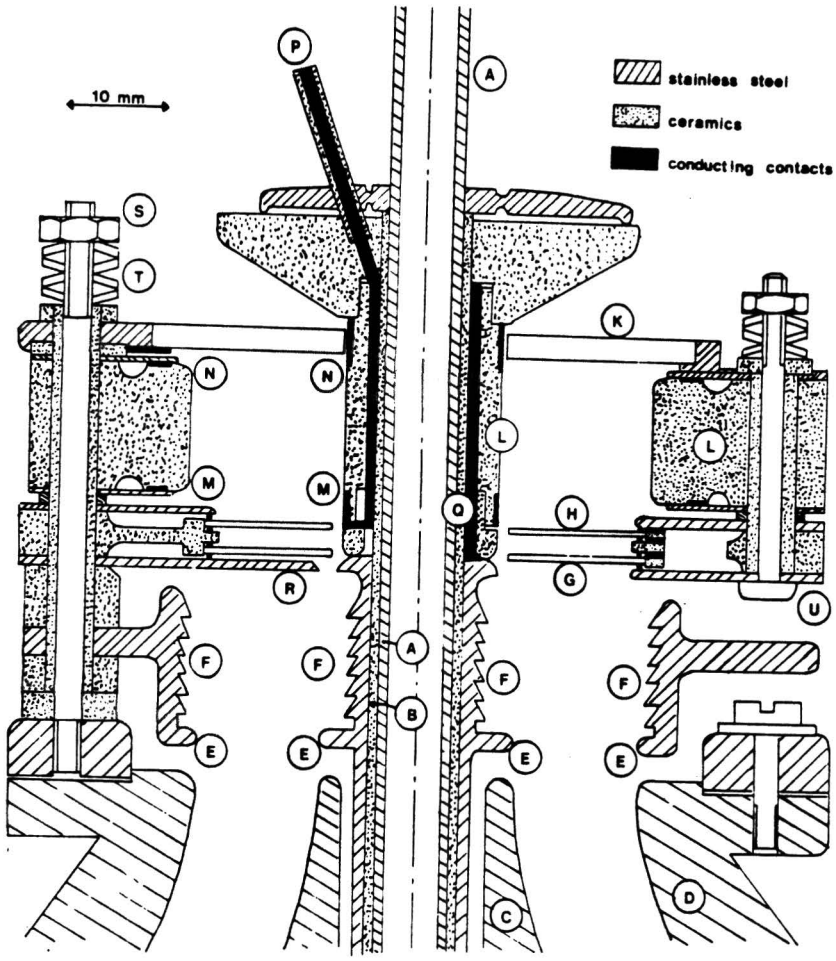

Fig. 3.5. The detector array showing the pipe (A) through which the primary ion beam passes. The pipe is isolated from the high voltage on the detector by ceramic material first MCP (G) after passing through the last Herzog element (E) and the skimmers (F). The electron clouds emitted from the second MCP (H) are measured on the charge collector (K). The inner and outer conducing layers (L) are electrically connected at the bottom (M) to the back of the second MCP and at the top (N) to the detector holder (K). The mixed angle of the charge collector is shield by the strip (R).

A three dimensional picture of the whole analyzer and detector assembly is given in figure 3.6.

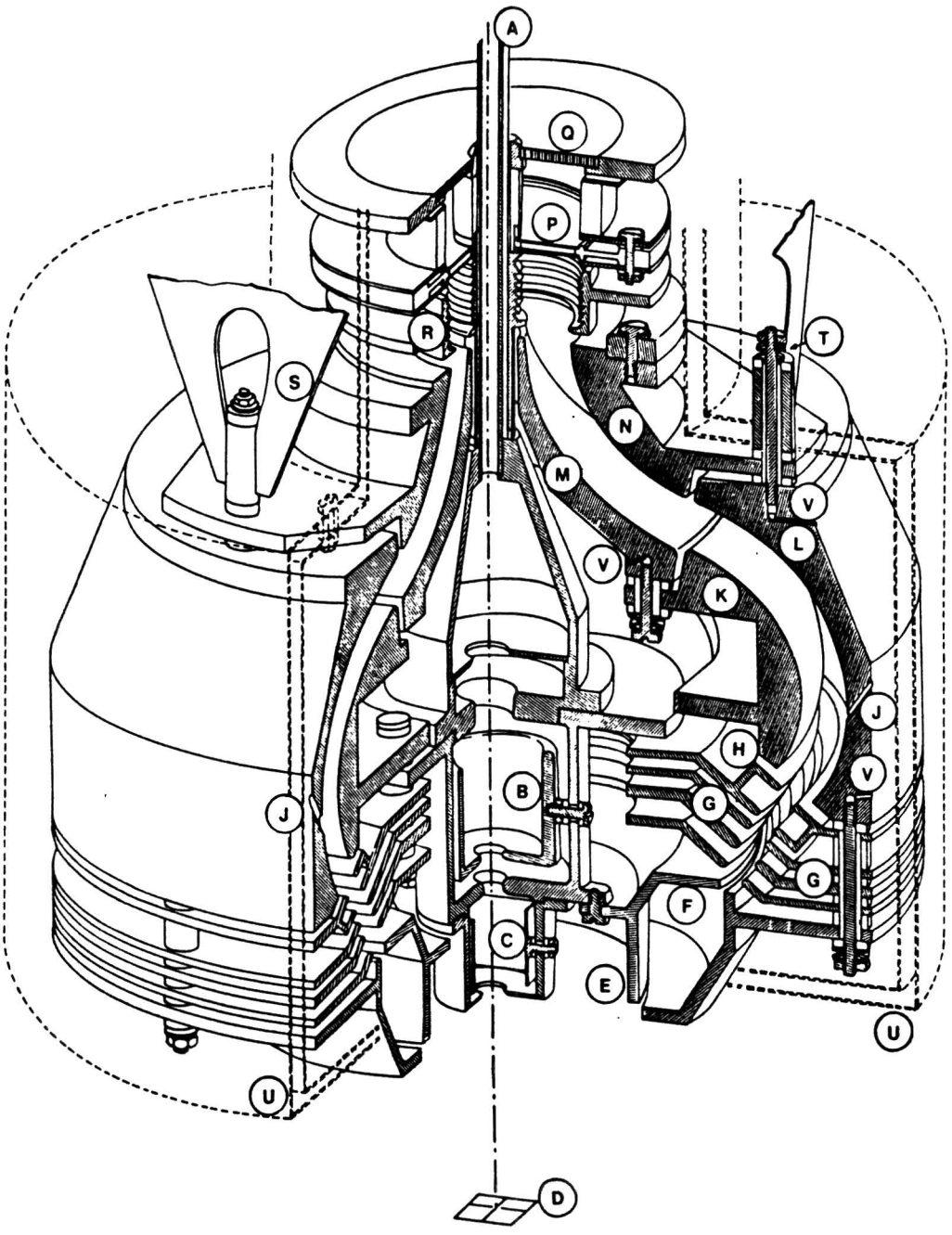

Fig. 3.6. Three-dimensional view of the EARISS-energy analyzer and detection system. The primary ions coming from the central ion source, move along the stainless steel tube A, through the last Einzel lens B and the deflection plates C onto the sample D. The scattered ions are accepted by the circular slits E and F after which they are postaccelerated by the zoomlens G. The last element of the zoomlens H determines the energy of the particles entering the analyzer. All charged particles are deflected by elements K and L whereas neutrals can pass through one of the four holes J. They can be used to determine the relative amounts of neutrals and ions. After the ions pass the second set of elements M and N they hit the

channel plates P. An electron cloud produced by these channel plates will hit the charge collector Q where the charge is used to determine the radial and azimuthal position of the charge cloud and hence of the incident ion. The skimmers R are used to eleminated ions leaving the analyzer at too large angles.

3.6 *References*

[1] **G.J.A. Hellings**, Energy and Angle Resolved Ion Scattering Spectroscopy, Ph.D. Thesis, Eindhoven (1986).

[2] **C.P.M. v. Heyst**, Calculations on an electrostatic zoomlens using a charge density method, Master Thesis, Eindhoven University of Technology (1986).

[3] **S.W. Boelens**, Het ontwerpen van de versnellens en de azimuth selector voor de EARISS, Master Thesis, Eindhoven University of Technology (1983).

Chapter 4. Microchannel Plates.

4.1 Introduction

Microchannel plates (MCP's) are an essential part of the EARISS detection system. They convert the signal coming from an incident ion into a measurable electron cloud. The electron cloud can be detected by the charge collector.

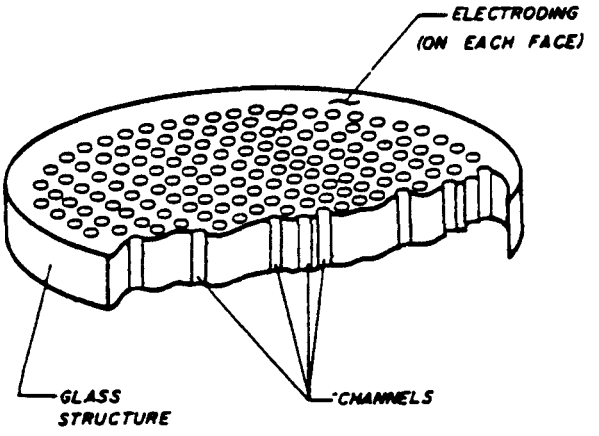

Fig. 4.1. Schematical representation of a microchannel plate. The channel diameter is 12 μm, the channel pitch is 15 μm. the plate diameter is 46 mm.

A MCP consists of a thin glass plate with a matrix of very small channels (12 μm diameter, 15 μm pitch). (fig. 4.1). Each of these channels behaves in the same way as a single channel electron multiplier, or channeltron [1]. The channels are internally cladded with a material that easily emits secondary electrons when excited by some primary particle (These could be ions, neutrals, electrons, photons etc.). The secondary electrons are accelerated towards the end of the channel. However since the channel has limited dimensions, they will frequently hit the walls thereby causing them to release more secondary electrons (fig. 4.2). This causes a cascade or avalanche of electrons which finally escapes from the channel as a small charge cloud containing about 10^3-10^4 electrons depending on the length-diameter ratio of the channel and the voltage across the channel plate.

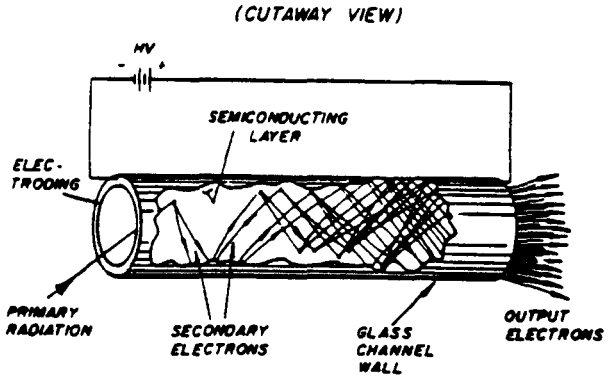

Fig. 4.2. Electron avalange caused by primary radiation in a single channel electron multiplier.

Two of these MCP's are used in the EARISS-detector so that gains of 10^6-10^7 electrons per incident ion can be reached. This setup of two MCP's is called a chevron configuration [2].

Since only one channel is excited at each ion incidence, the place where the ion hits the MCP surface is the same as where the electron cloud leaves the MCP. Thus the radial- and azimuthal information are conserved during the amplification process.

In the next sections we will discuss the gain of the chevron configuration (§4.2), the pulse height distribution of the electron clouds (§4.3), the enlarging of the charge cloud in free space (§4.4) and some common operation problems we have encountered during the operation of the MCP's (§4.5).

4.2 Specifications and gain

The chevron configuration used in the EARISS-apparatus consists of two Philips-Mullard microchannel plates, type G12-46DT/0 and G12-46/13. Both have an outer diameter of 46 mm of which 42 mm is effectively useful. A hole has been made in both channel plates, through which the primary ion beam passes. (fig. 4.3.a). Both channel plates have 12 μm channels with a 15 μm pitch. The first channel plate, on which the ions impinge is 1 mm thick. The second MCP has a 0.5 mm thickness. The latter plate has its channels placed under a 13^o angle with respect to the surface normal. Characteristics of both channel plates are shown in tabel 4.1.

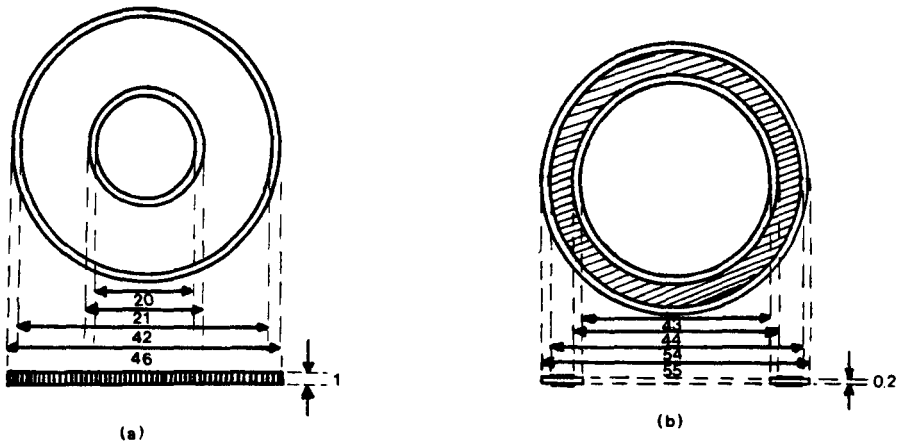

Fig. 4.3.a. Dimensions of the channelplates in mm. The hole is meant for the primary ion beam.

Fig. 4.3.b. Gold plated glass ring used for applying a voltage between the channel plates (dimensions in mm).

	G12-46/13		G12-46DT/0	
Plate diameter	46.0	mm	46.0	mm
Usefull diameter	42.0	mm	42.0	mm
Plate thickness	0.5	mm	1.0	mm
Channel diameter	12.5	μm	12.5	μm
Channel pitch	15.0	μm	15.0	μm
Open area	60	%	60	%
Electrode material	Ni-Cr + Pt		Ni-Cr + Pt	
Plate resistance	30-100	MΩ	60-200	MΩ
Channel angle	13^{o}		0^{o}	
Lenght/diameter	40		80	
Maximum temp.	300	^{o}C	300	^{o}C
Gain	$3\ 10^{3}$ (1000kV)		10^{4} (1200kV)	

Table 4.1. Specifications of the used microchannel plates.

The gain of a single channel electron multiplier is given by [1]:

$$G = \left[\frac{A \cdot V}{2\alpha V_o^{1/2}}\right]^{4V_o\alpha^2/V} \qquad (4.1)$$

Where: V is the voltage across the channel,

V_o is the initial energy of the emitted secondary electrons ($\approx$ 1 eV),

α is the length to diameter ratio,

A is a constant (A $\simeq$ 0.2).

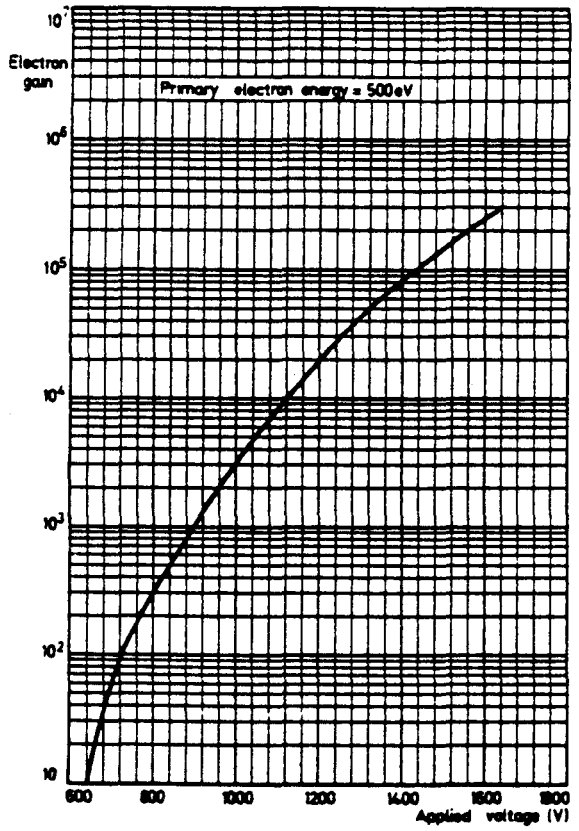

Fig. 4.4. Electron gain of a cascade of two microchannel plates as a function of the applied voltage per plate.

In figure 4.4 we have plotted a typical gain curve of a microchannel plate [2]. The channel plates are separated by a thin glass ring (0.2 mm thick). This ring has a circular gold contact on both sides. (fig. 4.3.b). It is used to apply a voltage across the gap between the channel plates. Furthermore it functions as a contact for the high voltage which has to be applied to the channel plates. The first channel plate will produce a small charge cloud (10^3 electrons) for each of the incident ions. This charge cloud escapes from one channel into the region between the plates. The electrons in the cloud have an initial velocity. This velocity plus the space charge forces are the cause of the charge cloud expansion.

By varying the voltage across the gap we can influence the time the electrons need to cross the region. Thus we can directly influence the size of the charge cloud when it strikes the second channel plate. This will be discussed in more detail in §4.4.

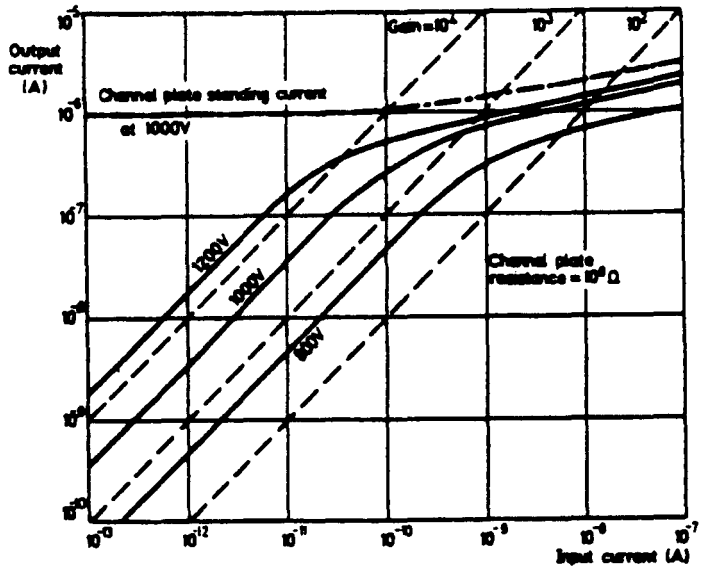

Fig. 4.5. Output current of a single channel plate as a function of the input current at different voltages across the plate. The output current increases linearly with the input current until the output current reaches a value of about 10% of the standing current through the plate. This is called current saturation.

In a channel plate two saturation effects may occur: current and space-charge saturation. Current saturation occurs when the channel plate input current reaches the order of 10% of the DC-current through the plate [2] (fig. 4.5). Effectively this means that the channels do not get enough time to recover from a previous trigger of the channel. This recovery time can be calculated as follows. The effective usefull area of the channel plate is calculated from figure 4.3.a to be: $\pi(21^2-10.5^2)$ = 1040 mm^2. Since the hexagonal matrix consists of channels with a 15 μm pitch we have 5128 channels per mm^2. In total we have about $5.3 \cdot 10^6$ channels. The resistance of the channel plates was measured to be 600 MΩ and 50 MΩ for the 1 mm and 0.5 mm plate respectively. Their channels thus have a resistance of $3 \cdot 10^{15}$ and $2.6 \cdot 10^{14}$ Ω respectively.

Assuming that the MCP's are filled for 40% with Corning 8161 glass (relative dielectric constant $\epsilon_r = 8.3$), we can calculate the plate's capacitance C using:

$$C = \frac{\epsilon_o(0.4\ \epsilon_r + 0.6)\cdot A}{d} \qquad (4.2)$$

Where: ϵ_o is the dielectric constant of vacuum ($8.85\cdot10^{-12}$ C/V),
A is the effective surface area (1040 mm^2),
ϵ_r is the relative dielectric constant (8.3), and
d is the channel plate's thickness.

In our case C is calculated to be about 40 pF for the 1 mm plate and about 70 pF for the 0.5 mm plate. The capacitance per channel is then $7\cdot10^{-18}$ F and $13\cdot10^{-18}$ F respectively. The recovery time τ_r can be calculated with:

$$\tau_r = R_{channel}C_{channel} \qquad (4.3)$$

Where: $R_{channel}$ is the channel resistance and
$C_{channel}$ is its capacitance.

Using the calculated values we obtain τ_{r1} = 22 ms and τ_{r2} = 4.5 ms. From the above calculations it results that channels should not be triggered more often than once every 200 ms; thus limiting the countrate per channel to about 5 counts/s. For the channel plate as a whole, we should not exceed a countrate of $\approx 3.0\cdot10^7$ cts/s (at $6\cdot10^6$ channels effectively), assuming we have an homogeneous input distribution. Another way of expressing this maximum number is per unit surface area: this would amount to a maximum of 22,000 ions s^{-1} mm^{-2}.

Space charge saturation is another effect that can occur at larger amplifications. In that case the number of electrons in a channel is so large that their negative space charge prevents other electrons to escape from the walls of the channel. Because of the large number of electrons which have formed the charge cloud, the wall remains

positive. As we have calculated above this positive charge is recovered in a characteristic time of a few ms. Since the total pulse duration of the firing of a charge cloud from a channel is about 1 ns [3], the positive charge on the wall is a further barrier for the escape of secondary electrons from the wall.

The consequence of the negative space charge and the positive charge remaining on the wall will be that the electrical field originating from the applied high voltage is nearly completely compensated. Therefore the electrons in the cloud will no longer be accelerated towards the end of the channel and the size of the charge cloud will remain constant. As a result the pulse height distribution of a channel plate operating in a space charge saturated mode will show a preferred charge cloud size. These pulse distributions will be discussed in the next section.

The detection efficiency of a MCP is defined as the fraction of the incident particles which produces a measurable charge cloud at the other end of the channel [4]. It depends on three factors: the secondary electron emission coefficient, the geometry of the channel and the gain of the MCP.

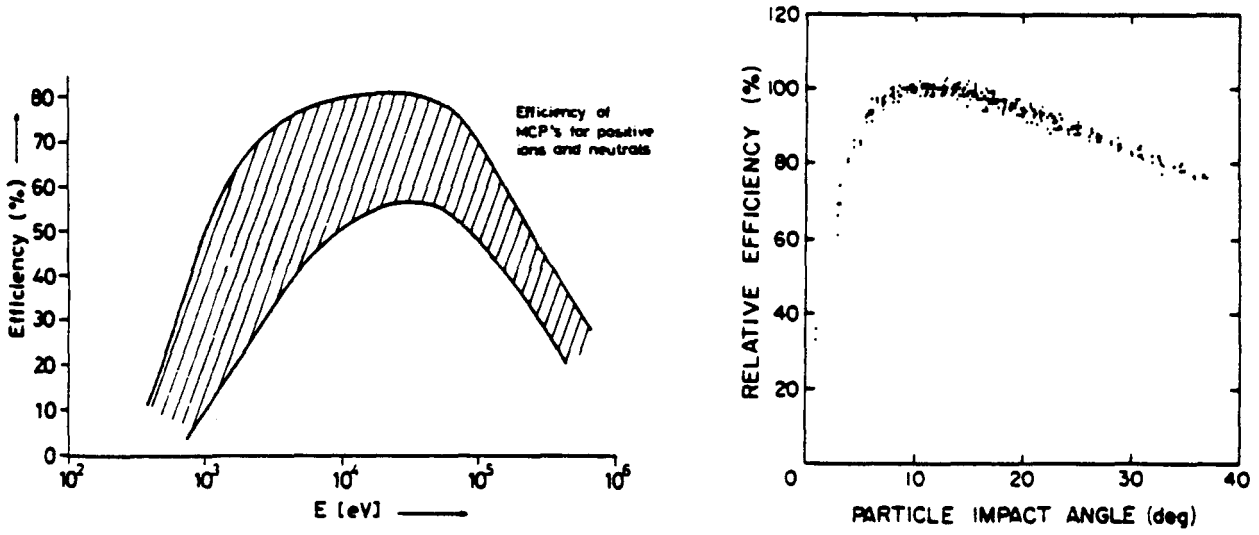

Fig. 4.6.a. The detection efficiency of a microchannel plate as a function fo the energy of incident positive ions and neutrals.

Fig. 4.6.b. The detection efficiency for ions of a microchannelplate as a function of the impact angle.

The secondary electron emission coefficient of the channel wall depends largely on the kind of the primary particle, its angle of incidence and its energy. The detection effiencies for noble gas ions and its dependence on energy and incident angle is shown in figure 4.6.a,b. From these figures it can be seen that there is an optimum efficiency at 10 keV ion energy and a 15^{o} impact angle. The energies we have used usually varied from 1 to 5 keV. However, the energy spread of the ions leaving the analyzer is about 6% of the analyzer pass-energy (§3.4). This means that differences in detection efficiency due to energy variations of the detected ions will not be very large. Much more important is the difference in detection efficiency due to variations in impact angle. The ions leaving the energy-analyzer will hit the first channel plate under angles varying from -6^{o} to $+12^{o}$ (fig. 4.7). Those ions with impact angles close to 0^{o} will have a relatively small detection efficiency (fig. 4.6.b) due to the fact that they can penetrate very deeply into the channel before they hit the channel wall.

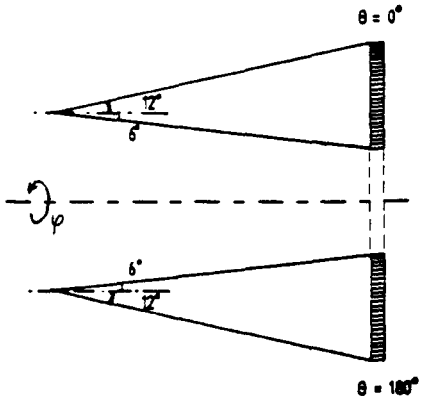

Fig. 4.7. The ions leaving the analyzer impinge on the first channel plate with angles between -6^{o} and $+12^{o}$.

This effect is demonstrated in figure 4.8 in which we have plotted the detected countrate versus the potential V_3 on the zoomlens. This potential can be used to scan the energy distribution of 2 keV Ne^{+} ions scattered from a Pt surface. The dip in the central peak of the figure is caused by the reduced detection efficiency for ions with incident angles close to 0^{o} with respect to the MCP-normal.

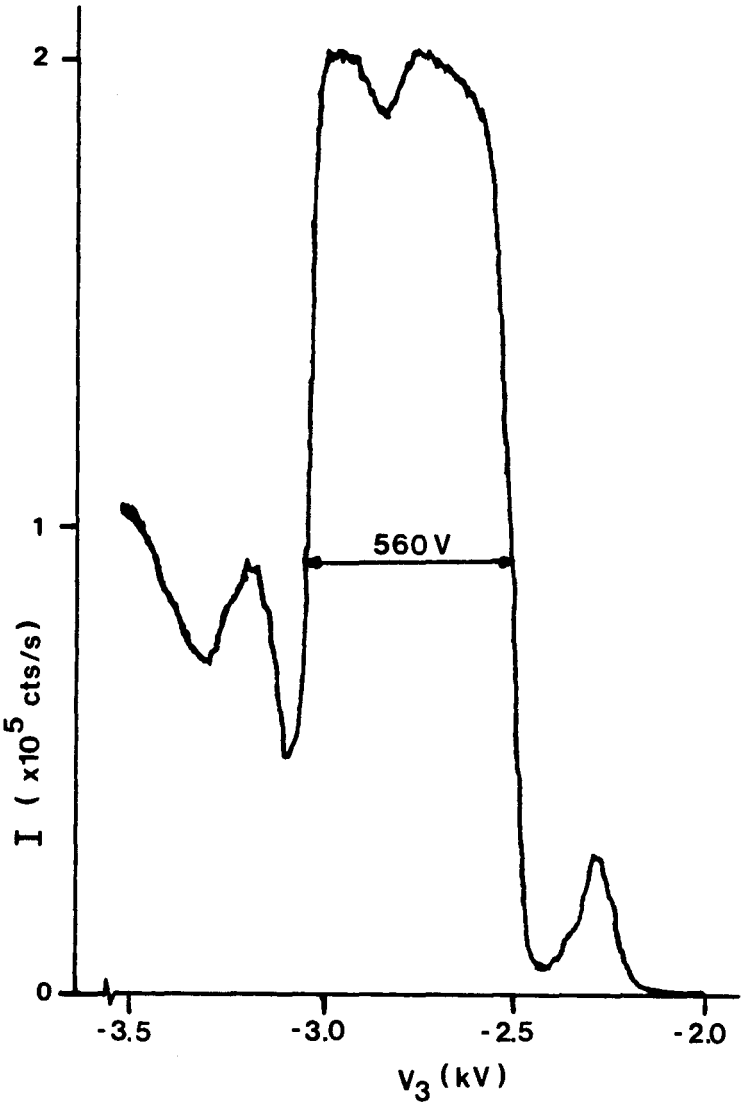

Fig. 4.8. The detected count rate of incoming ions as a function of the potential V_3 on the zoomlens. The mean peak shows a dip due to the normal incidence of the ions. The small peaks before and after the main peaks arise from neutrals. The background rises towards high acceleration voltages due to the detection of sputtered ions.

We have chosen the second MCP in our chevron construction to have channels with a 13^{o} angle with respect to the MCP-normal. This was done to prevent ionic feedback. Ionic feedback is an effect which occurs at high gain MCP configurations. When an escaping charge cloud has enough energy, it is able to ionize atoms from the residual gas. These ions will be accelerated in the opposite direction, where they are able to produce another cloud of secondary electrons. This effect depends on both the size of the charge cloud and on the background

pressure in the system. A continuous discharge is possible if the pressure reaches values of above 10^{-3} mbar. Generally, there are two ways to prevent ionic feedback: it is possible to use curved channels (J-shaped channels in MCP's or spiralized channels in channeltrons) or to use channels with an angle with respect to the surface normal. Both solutions try to minimize the length of the path an ion can travel before it hits the channel wall, thereby minimizing the possible size of the second charge cloud. Amplifications of the order of 10^8 are possible. It should be noted that we have taken the second solution. Curved MCP's were not readily available at the time the detector was constructed.

4.3 *Pulse height distributions*

As we have discussed in the last section, space charge saturated channels have a preferred electron-cloud size. In unsaturated channels the formation of charge clouds is a purely statistical process. This is the reason that the pulse height distribution of unsaturated channels is an exponential function [1]:

$$n(q) = n_o \exp(-q/q_o) \qquad (4.4)$$

Where n(q) is the number of counts with charge size q, and n_o, and q_o are some normalizing factors.

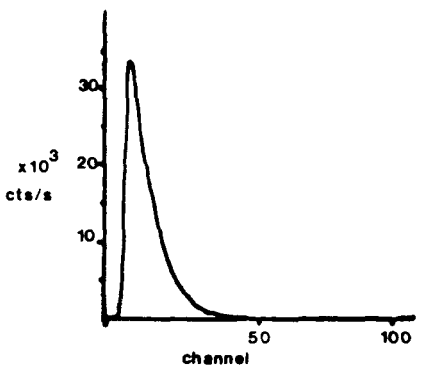

Fig. 4.9. Unsaturated pulse height distribution of the chevron construction.

An unsaturated pulse height distribution is shown in figure 4.9. The electron clouds escaping from the first channel plate have an unsaturated pulse height distribution. When they pass the region in between the channel plates they spread out due to their initial velocity distribution and due to space charge forces. By tuning the voltage across the gap between the MCP's, we are able to influence the size of the electron cloud when it arrives at the second channel plate. Thereby we are able to focus or defocus the charge cloud. This means that we have a way of varying the number of electrons that excite the channels of the second channel plate. As a result we can drive the channels of the second channel plate into space charge saturation by applying a larger voltage to the interplate region. This is shown in figure 4.10, where we have plotted the pulse height distribution of our chevron configuration operating in a space saturated mode. It is clearly shown that certain charge cloud sizes prevail.

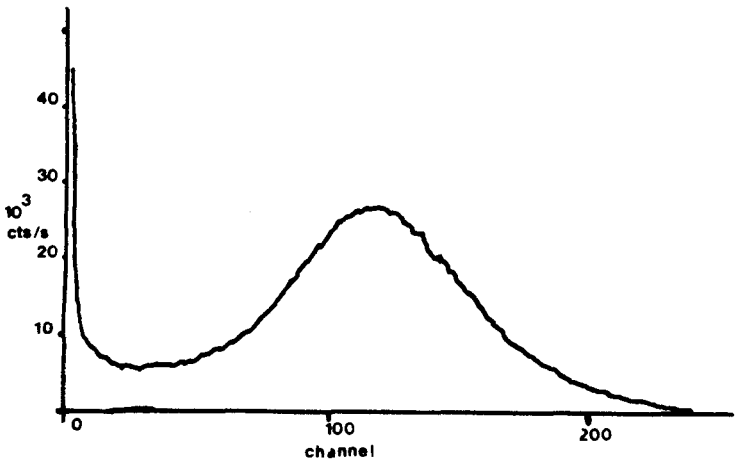

Fig. 4.10. Saturated pulse height distribution of the chevron construction showing a preferred charge cloud.

The reason we want the second channel plate to operate in space charge saturation, is that it is of advantage to have a narrow pulse height distribution: one can easily discriminate noise coming from the preamplifiers from real pulses by setting a level discriminator. A narrow distribution requires a smaller dynamic range for all further signal processing. In order to operate the EARISS detector in a space charge saturated mode we should at least apply 1500V across the first channel plate, 200V across the gap between the plates, and 1200V across the second channel plate.

Knibbeler [5] has shown that it is necessary to take the pulses from both the front and the back of the second channel plate to obtain a signal for the total charge in a charge cloud. The way in which we measure the size of the emitted charge cloud is discussed in chapter 6.

4.4 *Spread of the charge cloud*

The electrons leave the channel with a certain angular and velocity distribution. As we have explained in the last section, the electrical field applied between the two channel plates determines the size of the charge cloud on the surface of the detector.

Schat [6] has calculated the spread of the charge cloud between the first and the second channel plate, with the assumption that the forces on an electron due to the charges of the other electrons are negligible compared to the force on the electrons by the electrical field originating from the voltage applied across the gap. His calculations on the radius of the charge cloud are presented in table 4.2.

$V_{1,2}$ (V)	$R_{1/e}$ (μm)
50	115
100	100
200	78
400	69
800	60

Table 4.2. The 1/e radius of the electron cloud as a function of the voltage across the gap.

The desired radius is determined on the basis of the need of space charge saturation and on the demand to prevent current saturation. The first restriction yields (§4.2):

$$n \cdot A_2 > 10^5 \qquad (4.5)$$

where n is the number of electrons entering a channel in the second MCP, and A_2 is the amplification of the channel. The second restriction yield:

$$n \cdot C \cdot A_2 < 5 \cdot 10^6 \cdot s^{-1} \tag{4.6}$$

where C is the maximum allowable count rate per channel (C = 5 cts/s) and the factor $2 \cdot 10^6$ is calculated from the current through the channel at 1200 Volts across the plate. Current saturation then limits the pulse current to a value of 10% of the calculated DC-current through the channel. From the above equations and assuming the maximum countrate C to be 5 cts/s, we conclude:

$$10^5 < nA_2 < 10^6 \tag{4.7}$$

The value of n is determined by the number of electrons coming from the first channelplate. If we take the gain of the first MCP to be A_1, and we assume that the electrons leaving the first MCP distribute themselves over a channels in the second plate we obtain:

$$10^5 < \frac{A_1 A_2}{a} < 10^6 \tag{4.8}$$

Our amplifiers are not able to handle count rates of more than 10^5 cts/s if the average charge equals 1 pC. This restricts the overall amplification $A_1 A_2$ to $6 \cdot 10^6$. From these arguments we conclude that:

$$6 < a < 60 \tag{4.9}$$

The spread of the charge cloud between the two channel plates should therefore be restricted to a number of 60 channels on the second MCP. This is a radius of 15 $\mu m \cdot \sqrt{a}$ = 0.1 mm. The lower limit yields a minimum radius of 27 μm.

The calculations of Schat [6] were based on the assumption that the spreading of the charge cloud due to the space charge was negligible. The acceleration of an electron caused by the electrical field between the channelplates if given by:

$$a_E = \frac{q_e V_{1,2}}{m_e D_{1,2}} \tag{4,10}$$

where a_E is the acceleration, q_e is the elementary charge. $V_{1,2}$ is the interplate voltage, m_e is the electron mass, and $D_{1,2}$ is the distance between the MCP's.

An electron at the edge of the charge cloud will in a first order approximation experience an electrical force from the other electrons:

$$a_s = \frac{nq_e^2}{m_e 4\pi\epsilon_o R^2} \qquad (4.11)$$

where n is the number of electrons in the cloud, and R is the cloud radius, ϵ_o is the permittivity of vacuum ($\epsilon_o = 8.85 \cdot 10^{-12}$), and a_s is the acceleration due to the space charge. If we take $n = 10^3$ and $R = 6$ μm we can calculate a_s to be $7 \cdot 10^{15}$ ms^{-2}. If we take $V_{1,2} = 200$ V and $D_{1,2} = 0.5$ mm we can calculate a_E to be $2 \cdot 10^{17}$ ms^{-2}. The difference is about 2 orders of magnitude and therefore the forces due to the space charge can be neglected in the region between the channel plates.

The charge cloud leaving the second MCP has to cross the gap between the MCP and the charge collector. If we look at this region (fig. 3.3), we have A) a lower electrical field strength between MCP 2 and the collector and B) much larger electron clouds.

If we take $V_{1,2} = 200$ V and $D_{2,c} = 17$ mm we have $a_E = 2.0 \cdot 10^{15}$ ms^{-2}. If the charge cloud has about $6 \cdot 10^6$ electrons on a radius of 50 μm we have: $a_s = 6 \cdot 10^{17}$ ms^{-2} which is 2 orders of magnitude larger than a_E. Therefore in this case space charge is the main reason for the expansion of the charge cloud. Rees et al. [7] have measured the radius of a charge cloud to be of the order of 1.5-2.5 mm (1/e value). The distance between their channel plate and detector was 15 mm and the applied voltage was 200 V. At these radii a_s is about $3.8 \cdot 10^{14}$ ms^{-2} which is smaller than a_E. Therefore we can assume that a further expansion of the charge cloud beyond this radius, is almost linear (fig. 4.11). In the calculations of Rees et al. [7], the electron cloud takes about 3.5 ns to travel from the MCP to the detector. In our detector configuration this is about 5 ns. The time needed for an electron to travel across the potential difference between the second MCP and the charge collector is given by:

$$t_{2,c} = \left[\frac{2\, D_{2,c}^2\, m_e}{q_e\, V_{2,c}}\right] \qquad (4.12)$$

where $t_{2,c}$ is the time needed for travelling from MCP-2 to the collector, and $V_{2,c}$ is the potential difference between those two. Since we assume the further expansion to be linear, we can calculate the radius of the electron cloud to be:

$$R_{1/e} = A\, \frac{D_{2,c}}{\sqrt{V_{2,c}}} \qquad (4.13)$$

where $R_{1/e}$ is the radius of the cloud at 1/e of the maximum (fig. 4.11), and A is a factor which can be estimated from the data given by Rees et al: ($D_{2,c}$ = 15 mm, $V_{2,c}$ = 200 V)

$$\begin{aligned} R_{1/e} &= 1.5 \text{ mm yields } A = 1.4 \\ R_{1/e} &= 2.5 \text{ mm yields } A = 2.4 \end{aligned} \qquad (4.14)$$

Using the above data we are able to calculate the size of the charge cloud at the EARISS charge collector (§5.2).

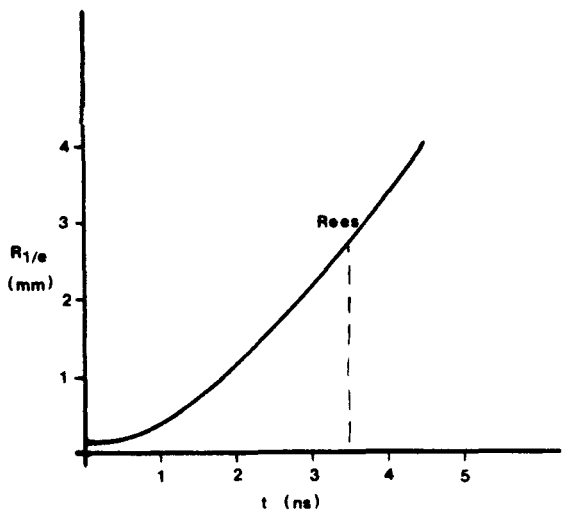

Fig. 4.11. The radius of the charge clouds arriving on the collector from Rees et al. [7].

4.5. *Common operating problems.*

During some of our first experiments we noted sudden instabilities in the current through the MCP's. These were thought to originate from electrical discharges through the MCP's which causes a sudden drop in the MCP resistance. Since the high voltage applied was able to deliver substantial DC-currents (mA's), there was substantial damage done to both the channelplates and to the glass ring between the channel plates (fig. 4.12).

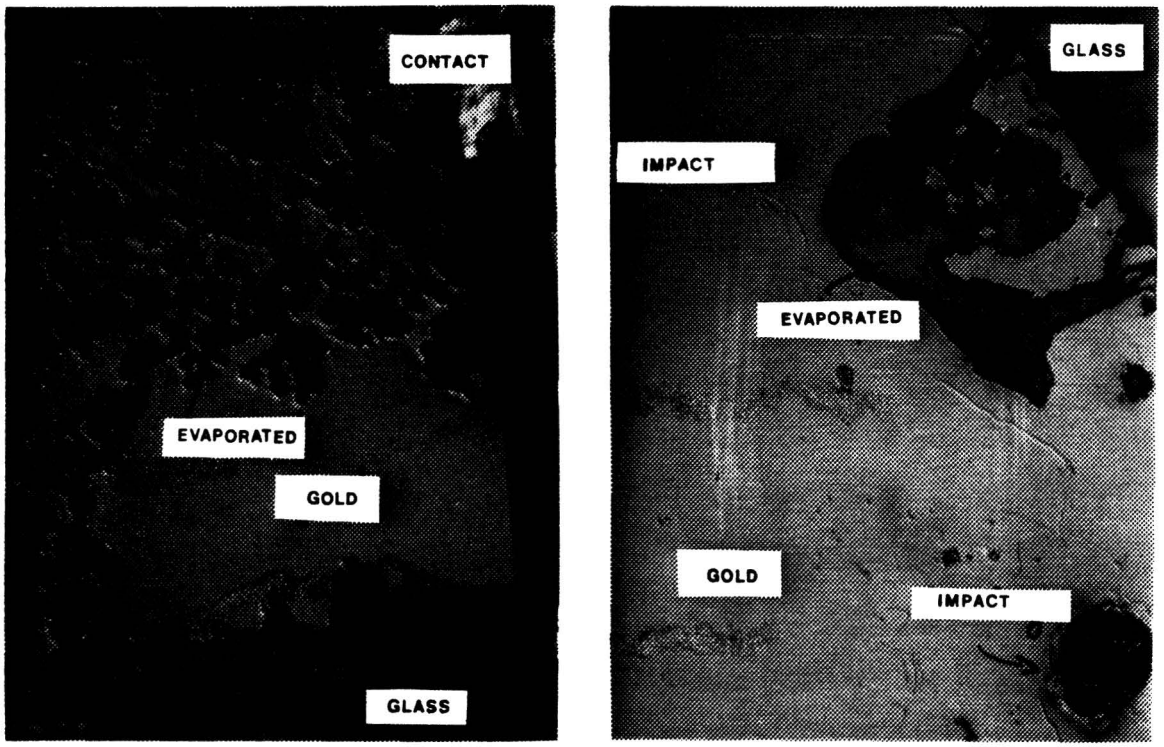

Fig. 4.12. Damage to the goldplated surface of the glass ring due to spark impacts and high voltage discharge.

The large currents caused the evaporation of the gold layer on the glass ring close to contact wires. Also some spots were observed where spark-impacts had taken place. In order to prevent these kind of damages it was thought to be necessary to put resistors of over 1 MΩ in the H.V. supply lines to the channel plates. Electrical discharge can still occur, but the currents can never become so large that they can damage the detector.

Spontaneous pulses were observed occasionally. Usually after increasing the voltage over the chevron. After some time, typically several hours a decrease in the number of spontaneous pulses was observed. These effects were also described elsewhere [8,9,10,11]. It is generally believed that spontaneous pulses are caused by field-emission. The spot where this occurs is called a 'hot spot', or a 'switched on channel'. The dark-current of channel plates is usually very low. We have measured a dark current of about 80 cts/s. This number increases exponentially with the channel plate voltage. Channel plates should be treated very carefully. It is reported [8] that if the applied voltage is increases to fast, sudden bursts of pulses presumably caused by desorbed gasses can damage a MCP in less than 1 ms. Therefore one should monitor the number of spontaneous pulses during the increase of the MCP-voltage. It was suggested that one should never increase the voltage before the number of spontaneous pulses has dropped a factor 10. A number of protective measures are discussed in [4]. A further discussion on the prevention of electrical discharges is given in §6.4.

4.6 References

[1] **J.L. Wiza**, Nucl. Instr. Meth. 162 (1979) 587.

[2] **Philips Data Handbook**, 9 (1980) 06-80.

[3] **B. Leskovar and C.C. Lo**, IEEE Trans. Nucl. sc. NS-25 (1978) 582.

[4] **D. de Bruyn et al.**, Microchannelplate Report, FOM institute for atom and molecular physics, Asterdam (1982).

[5] **C.L.C.M. Knibbeler**, Master Thesis, Eindhoven University of Technology (1983).

[6] **E.P. Schat**, Masters Thesis, Eindhoven University of Technology (1986).

[7] **D. Rees et al.** (to be published).

[8] **P.C. Friedman et al.**, Rev. Sci. Instr. 59 (1988) 98.

[9] **R.F. Malina and K.R. Copburn**, IEEE Trans. Nucl. Sci. NS-31 (1984) 104.

[10] **O.H.W. Sigmund et al.**, IEEE Trans NUcl. Sci. NS-31 (1985) 776.

Chapter 5. The Two Dimensional Charge Collector.

5.1 *Introduction*

The EARISS 2-dimensional detector is used to determine the point of impact of an ion after it has passed through the analyzer. The microchannel plates (MCP) have amplified the signal from the ion to a detectable electron cloud, thereby preserving the information on the point of impact. The center of the charge cloud should be determined. There are several ways in which this can be done [1].

If we want to obtain an azimuthal and energy spectrum of a sample we should at least be able to determine the point of impact of the ion with an accuracy of 1% in both directions. This implies that should we use small individual charge collectors in both a radial and an azimuthal direction. This would require 10^4 collectors, each with its own amplifiers and signal processing. This solution is too complicated to be practical. Several solutions have been found [2], that do not require such a large number of collectors and electronic circuits.

The use of conducting strips on the collector in a grid can reduce the number of circuits considerably to about 200. Since this number is still rather large due to the number of vacuum feedthroughs that such a detector would need, several authors have tried other solutions. One of these is to place a capacitor or resistor between each strip, and collecting the charge at the end of the chain [3,4]. The time between the moment of impact and the moment the pulse arrives at the end of the chain, can now be used to determine the point of impact. The number of amplifiers can in this case be reduced to four or five. Another possibility is to shape the strips in such a way, that the amount of charge collected on a strip is a measure for the place where the charge cloud was deposited on the collector.

Several forms of conducting strips have been invented. C. Martin et al. [5] used a two dimensional set of strips and wedges (fig. 5.1). The strips have a width varying in the Y direction, whereas the width of the wedges only varies in the X direction. In this way, the charge collected on a strip is a measure for the Y position and the charge collected on a wedge is a measure for the X position of the point of impact. A complicating factor is that the number of electrons in a charge cloud is not constant. This means that the collected charge on each strip has to be normalized with respect to the total charge in the cloud.

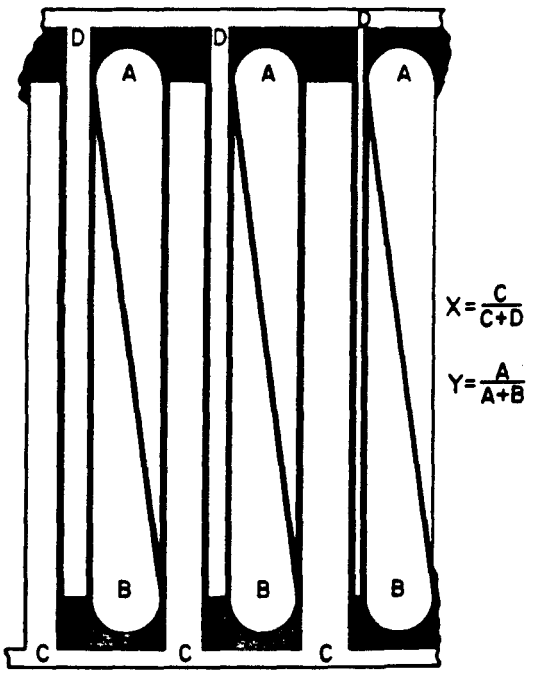

Fig. 5.1. Wedge (A) and strip (C) detector of Martin et al. [5]. The position of the center of the charge cloud is determined by the fraction of the cloud on each strip set.

It has been shown elsewhere [5,6,7,8] that the size of the arriving charge cloud should be somewhat larger than the characteristic distance in the collector, thus larger than the size of a single set of strips. The situation is complicated by the fact that the size of the charge cloud is not constant. It varies with the number of electrons in the cloud.

The disadvantage of the charge collector used by Martin et al. [5] is that the strips run parallel to the wedges for a distance of more than 4 m. The consequence is that the coupling capacitance between the X and Y signals is relatively large. This causes cross-talk. Another disadvantage of the wedge and strip collector is that the resolution of this type of collector depends on the position where the incident electron cloud hit the collector. Both disadvantages are absent in the present collector design.

The charge collector in our situation should have a hole in its center for the passage of the primary ion beam (e.g. fig. 3.6). There are several collector geometries that solve this problem [5,9]. We have chosen a sickle and ring (SR) geometry which will be described in the next section.

5.2 *Detector design*

The two-dimensional sickle and ring charge collector which is schematically shown in figure 5.2 is used to determine the center of the deposited charge cloud coming from the second MCP.

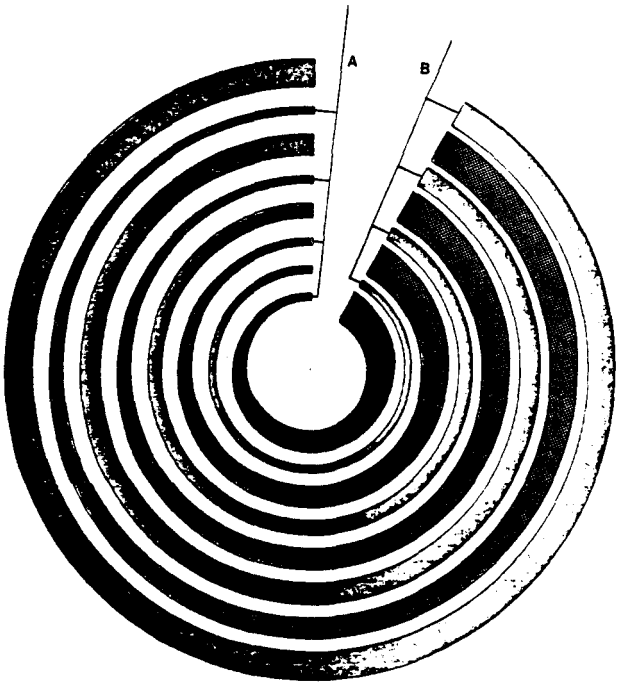

Fig. 5.2. Principle of the sickle (A) and ring (B) detector. The sickle width increases with the azimuth φ. The ring increases with increasing radius R.

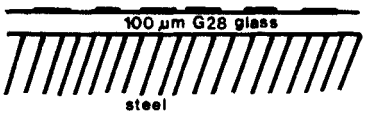

Fig. 5.3. The collector consists of thin gold strips deposited on a glass substrate which is mounted on a steel support.

The detector consists of small gold strips (1 µm thick) deposited on a thin (100 µm thick) glass substrate (SiO_2) (fig. 5.2.b). The substrate is mounted on a stainless-steel support, which functions as a "ground" contact; this will be discussed later (§6.5). The gold

strips on the detector have a special shape. Each of the sickles increases linearly in width with the azimuthal angle φ. All sickles have the same width in a radial direction. Just the opposite is the case for the ring-like strips B. Their width remains constant in an azimuthal direction. But the width of each ring increases linearly with increasing radius. Altogether we have 14 sickles and 14 rings on our collector. A charge cloud falling onto the detector will deposit its charge on a few rings and sickles at the same time. The charge collected on the rings determines the radial position of the center of the incident charge cloud. The charge collected on the sickles determines its azimuthal position. Since we can not know in advance the total charge in the electron cloud, due to the statistical variations in the gain of the channel plates, we have to normalize the collected charges on the sickles and rings with respect to this total charge. This is done by measuring the charge emitted from the second MCP (§6.2).

We have explained previously (Chapter 3) that the energy analyzer converts the energy distribution of the backscattered ions in a radial distribution on the first MCP. The analyzer is optimized in such a way that the radial distribution is linearly proportional to the energy. Therefore the radius of the center of the charge cloud is a linear measure for the energy of the scattered ion, and the azimuthal coordinate is of course preserved.

According to the calculations of Hellings [10] the ions having an energy equal to the analyzer pass energy E_p are focussed in a 16 mm ring on the first MCP. The analyzer focusses ions with $E_p \pm 6\%$ on the edges of the MCP, thus with radii of 21 and 11 mm respectively. The energy E_f of a detected ion can be calculated using:

$$\frac{E_f - (E_p - E_p * 0.06)}{(E_p - E_p * 0.06)} = \frac{(R - 21)}{(16 - 21)} \qquad (5.1)$$

Which yields:

$$\frac{E_f}{E_p} = 1.192 - R * 0.012 \qquad (5.2)$$

Where R is the radius of the point of impact of the ion on the collector, given in mm.

The radius R is determined by the amount of charge falling on the ring strips. From now on we will call these strips the energy strips or E-strips. The sickle strips A will be called azimuth-strips or φ-strips. The radius R and the azimuth φ of the center of the charge cloud are given by:

$$R = Q_E / Q_T$$
$$\varphi = Q_\varphi / Q_T \qquad (5.3)$$

Where Q_E is the charge collected on the E-strips,
Q_φ is the charge collected on the φ-strips and
Q_T is the total charge in the cloud.

The space between the E-strips and φ-strips is filled with a ground strip G (fig. 5.3.a). Each individual E-or φ-strip has its own compensating ground strip E' or φ'

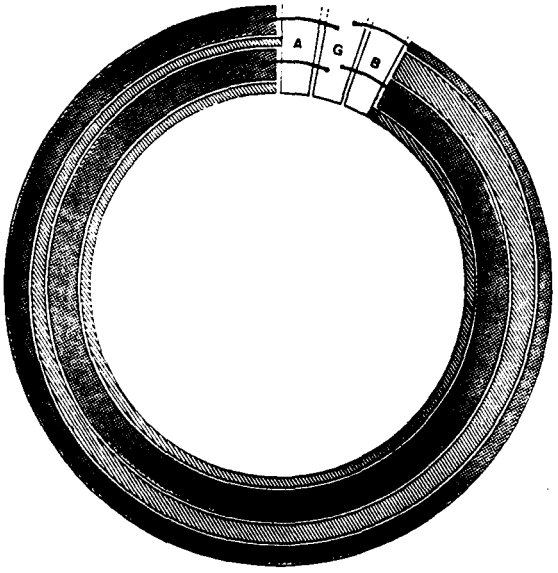

Fig. 5.4. A complete strip set showing also the ground strips G which occupy the space left open by the sickles (A) and rings (B). The width of a complete set is 1 mm. The inner radius varies from 9 to 22 mm.

The distance between the strips is always 40 μm. A "set" of strips will consist of four strips (E, E', φ, φ') and four spacings (three between the strips and one separating this set from the next one). The width W of each strip is given by:

$$
\begin{aligned}
W_E &= 40 + 26.15\cdot(i-1) && (\mu m) \quad (i = 1 \ldots 14) \\
W_{E'} &= 380 + 26.15\cdot(i-1) && (\mu m) \quad (i = 1 \ldots 14) \\
W_\varphi &= 40 + \varphi && (\mu m) \quad (\varphi = 0^o \ldots 340^o) \\
W_{\varphi'} &= 380 - \varphi && (\mu m) \quad (\varphi = 0^o \ldots 340^o)
\end{aligned}
\tag{5.4}
$$

Where i is the number of the set (i = 1 has the smallest radius, i = 14 has the largest). Each set has a total width of $2\cdot(40 + 380 + 2\cdot40)$ μm = 1 mm.

The inner radius of the collector is 9 mm and the outer radius is 23 mm. Not the full 360° azimuth angle is used. A 20° part is used to connect the strip sets to the each other and to the preamplifiers placed outside the vacuum system. Therefore a 340° useful area is available for the collecting of charges (fig. 5.5).

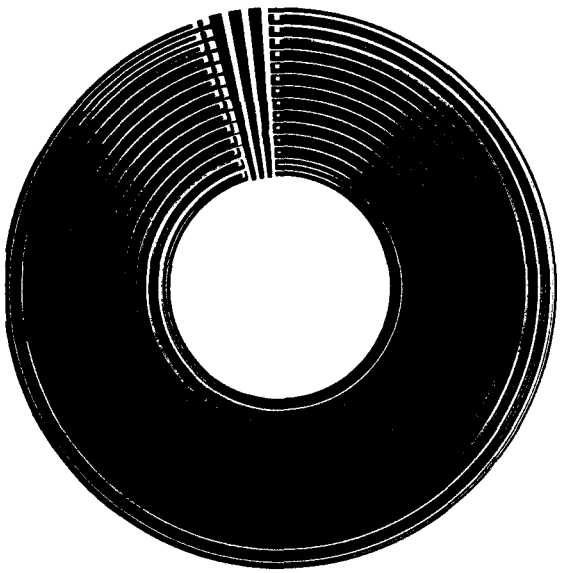

Fig. 5.5. The 14 strip sets and the connecting strips of the sickle and ring collector.

The detector is somewhat larger than the active area of the MCP's. This was done since the charge clouds escaping from the MCP's will expand in the region between the MCP and the charge collector. The arriving charge cloud should have a diameter somewhat larger than the characteristic of a set of strips which in our case is 1 mm. The distance between the second MCP and the collector in our detector system is 16.5 mm. According to equation (4.13) we can calculate the voltage needed across the gap between the second MCP and the collector:

$$V_{2,c} = \left[A \frac{D_{2,c}}{R_{1/e}} \right]^2 \qquad (5.5)$$

If we substitute the values for A resulting from the measured by Rees et.al. [7] we obtain 534 V < $V_{2,c}$ < 1570 V. This large voltage can not be used in our case due to the conducting layers (fig. 3.6). These layers consists of a RuO_4-layer with a high resistance $R_\square$ = 10 MΩ which is deposited on a glass (SiO_2)-substrate. The layers would be damaged if such a high voltage were applied to them. The temperature they would get by ohmic heating would be too high.

This problem and some other problems concerning the conducting layers will be discussed in §8.2. There are only two more remarks to be made at this point concerning the construction of the collector. Firstly, the insulating gap between two strips (fig. 5.6) will charge itself negatively due to the negative charge clouds. This charge will influence the electrical field above the collector and thus the effective width of each strip will be larger than its physical width.

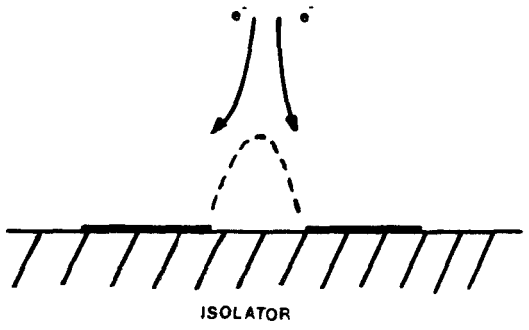

Fig. 5.6. The deflection of the electrons in the charge cloud by the potential between the strips. This effectively enlarges the strip size.

Secondly, we have noticed that during the production process of several indentical collectors, the mask which was used to deposit the gold strips was sometimes turned upside down. Therefore care should be taken: two different collectors exist which are each others mirror image. This should not cause any trouble provided that it is known which strip is connected to which preamplifier.

5.3 *Signal transmission*

The collected charges on the strips have to be fed into the amplifiers and signal processing system. The input capacitance of a charge sensitive preamplifier should be kept at a minimum, because of the noise which they produce at larger capacitances (§6.3). Therefore we should keep the connecting wires as short as possible. Another point to take into consideration is the capacitive cross-talk between the strips. This can be demonstrated as follows (fig. 5.4.). The capacitance between two strips is determined by the length that they are parallel to each other. The ground strips (E' and φ') are connected to a ground potential. The result is that the coupling capacitance between the E- and φ-strips is reduced, since a signal on the ground strip will be coupled to ground instead of to the other strip. This capacitance is further reduced by the backing of the charge collector (fig. 5.3.a). This backing is connected electrically to the ground strips. It increases the capacitance between the E and ground strip or between the φ and the ground strip, but it reduces the capacitance between the E- and φ-strips [6].

The capacitance between the E and φ strips was measured to be 3 pF with the ground strip connected to ground. With the ground strip not connected to ground we measure a capacitance of 110 pF. The capacitance between the E-strips and the ground strips was measured to be about 210 pF. About the same capacitance was measured between the φ-strips and the ground strips.

The wires which conduct the charges to the preamplifiers have recently been changed. Two parallel wires (about 40 cm length) have, at a distance of 1 cm, a capacitance of 30 pF. This would drastically increase the coupling capacitance between the E- and and φ-signal. Therefore we have made an in-vacuum coaxial cable, one for each strip. The mantle is at the same potential as the groundstrip. The central line of each coax conducts the signals of the E-, the φ-strips respectively to the preamplifiers. The mantle of each coax conducts the charges collected on the ground strips to the grounding capacitor. A further discussion on the signal processing will be given in chapter 6.

5.4 *References*

[1] **M. Lampton**, The Microchannel Image Intensifier, Sci. American nov. (1981).

[2] **M. Lampton and F. Paresce**, Rev. Sci. Instr. 53 (1974) 1098.

[3] **D.P. de Bruyn and J. Los**, Rev. Sci. Instr. 53 (1982) 1020.

[4] **R.W. Wijnandts van Resandt et al.**, J. jPhys. E. 9 (1976) 503.

[5] **C. Martin et al.**, Rev. Sci. Instr. 52 (1981) 1067.

[6] **C.L.C.M. Knibbeler**, Masters Thesis, Eindhoven University of Technology (1983).

[7] **D. Rees et al.**, to be published.

[8] **D. de Bruyn et al.**, Microchannel Plate Report, FOM Institute for Atom and Molecular Physics, Amsterdam (1982).

[9] **M. Lampton and C.W. Carlson**, Rev. Sci. Instr. 50 (1979) 1093.

[10] **G.J.A. Hellings**, Energy and Angle Resolved Ion Scattering Spectroscopy, Ph. D. Thesis, Eindhoven (1986).

Chapter 6. Analog Electrical Circuit.

6.1 *Introduction*

The electrical circuits of the EARISS apparatus can be separated into two different parts: the analog and the digital circuit. The analog circuit is used for supplying all bias voltages to the different parts of the analyzer and detector system. Another function of the analog circuit is the signal transmission and amplification (§ 6.2). These two parts will be described in this chapter. The analog/digital conversion and the digital electronic circuit will be described in chapter 7.

Since the charge collector is composed of thin gold strips close to each other, we should be careful that no discharges can occur between the strips or from the strips to the surroundings. Thus an important aspect of the analog circuit is the prevention of high voltage (H.V.) discharge (§6.4). Another aspect is the filtering of high frequency interference (also Radio Frequency Interference, RFI). This will be discussed in §6.5. High frequency cross-talk between the measured charges on the collector strips should be prevented, as we have seen in section 5.3. This subject will be dealt with in section 6.6.

Event detection is done in a timing circuit (§6.6). The timing circuit supplies a trigger pulse to the analog to digital converters (ADC's), at the moment the charge can be sampled on their inputs. We have discussed in section 5.2 that the measured charge on the E- and φ-strips has to be divided by the total charge Q_T in the electron cloud. All three charges are measured and their values are digitized by the ADC's. The division is done in the digital electronic circuit.

6.2 *High voltage power supplies*

The power for all elements of the zoomlens/analyzer/detection system are supplied from a single rack (fig 6.1). The zoomlens requires three bias voltages ranging from -10 kV up to +10 kV on the second, third and fourth lens elements. (The first element is connected to ground, and the fifth element is connected to the fourth

element, section 3.4). These voltages (V_1, V_2, V_3) are supplied by three FUG HCN-35-12500 power supplies rated for 12.5kV (positive or negative). These power supplies are stable within 0.1%. They can be programmed with a 0....10V input voltage. This enables computer control using conventional digital to analog converters (DAC's).

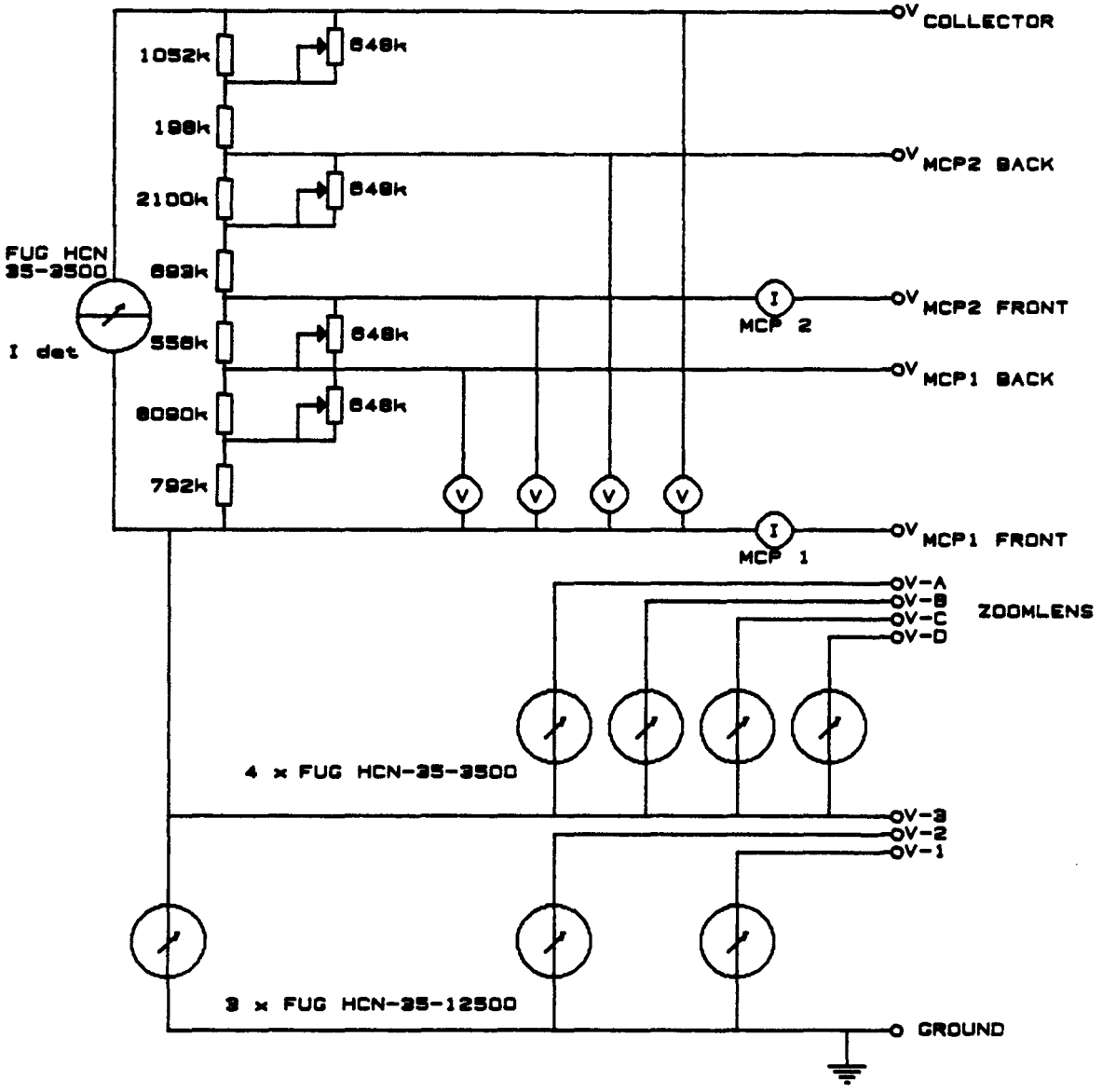

Fig. 6.1. Power supply for the analyzer, detector and zoomlens. All power supplies are mounted in one rack.

The analyzer segments require voltages ranging from -2 ...+2 kV (equation 3.3) with respect to the voltage on sections 4-5 of the zoom lens. We used four FUG HCN-35-3500 power supplies rated for 3.5 kV (positive or negative).

The detector voltage is supplied by a fifth FUG HCN-35-3500. This power supply is set as a current source. It supplies its current to a resistor-network (fig 6.1) which enables us to set the required voltages over the channel plates, the gap between MCP-1 and MCP-2, and over the gap between MCP-2 and the charge collector. The currents through the two channel plates are measured, as well as the voltages over the different elements. Typical detector voltages are:

$$\begin{aligned} V_{MCP-1} &= 1000...1600V \\ V_{1,2} &= 0...300V \\ V_{MCP-2} &= 1000...1300V \\ V_{2,c} &= 200...600V \end{aligned} \qquad (6.1)$$

Where: $V_{MCP-1\ (MCP-2)}$ is the voltage across channel plate 1 (2)
$V_{1,2}$ is the voltage across the gap between channel plates 1 and 2
$V_{2,c}$ is the voltage across the gap between MCP-2 and the collector.

Since the five FUG power supplies have a bias voltage with respect to ground, we are not able to program them directly by using DAC's. Instead we convert the DAC voltages to optical signals that are transmitted to a receiver through optical fibers. This receiver can be at high voltage with respect to the DAC's. The receiver converts the optical signals to input voltages (0..10V) for the power supplies. The required software for the DAC's has not yet been installed. Therefore all measurements were done by setting the voltages manually.

6.3 *Measurement of the collected charges*

An important part of the analog circuit is the charge measurement and amplification. As we have discussed previously, we have to measure three charges (§5.3), namely the charges collected on the E-strip and φ-strip and the total charge Q_T in the electron cloud escaping from the second MCP. This total charge Q_T can be measured in two ways. Firstly we can take the current pulse in the power supply lines of the second MCP. This yields a pulse which is proportional to the size of the escaping charge cloud. Secondly we can sum all the charges arriving on the detector (The sum of all the strips E, E', φ, φ').

Thereby we measure the number of electrons arriving on the collector. Provided that there are no losses between the second channel plate and the collector, both methods will give the same result. The second solution however is complicated by the fact that we want to use the ground strips E' and φ' as a shielding against cross-talk between the E- and φ-strips, as discussed in §5.3. This means that the charge on these strips is not available to be measured. A second disadvantage is that the determination of the sum signal ($Q_E + Q_{E'} + Q_\varphi + Q_{\varphi'} = Q_T$) would require more process time, thus limiting the maximum countrate.

For these reasons we have chosen the first solution. The current pulse in the supply lines of the second MCP is coupled to ground potential by two 10 nF capacitors (fig 6.2). Knibbeler [1] has shown that the combined pulses of the front and back of the channel plate are an accurate measure for the total charge in the electron cloud.

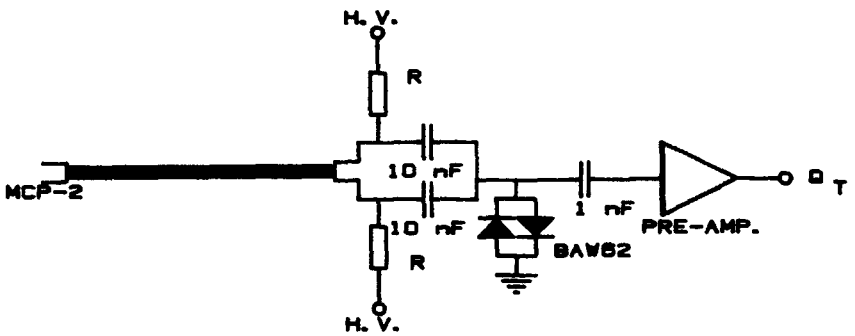

Fig. 6.2. The total charge is measured by decoupling the current pulse in the supply lines to the front and the back of the second MCP to low voltage. The antiparallel diodes are ment for protection against discharge.

The charge collected on the E- and φ-strips and the total charge Q_T from the second MCP are amplified by charge sensitive preamplifiers, after which they are pulse shaped and again amplified.

A charge sensitive preamplifier is in essence an integrator (fig 6.3). The charge Q_{in} collected on its input capacitor C_{in} will result in a small voltage step on the negative input of the operational amplifier (amplification A_o). This operational amplifier

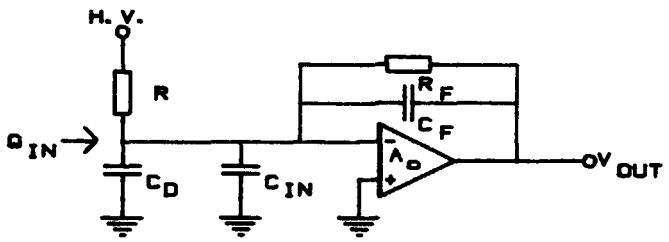

Fig. 6.3. Principle of a charge sensitive preampliefier.

will charge the capacitor C_f in order to bring the voltage on the negative input back to virtual ground. As a result the amplifier output exhibits a voltage step V_{out} given by [2]:

$$V_{out} = \frac{Q_{in}}{C_F + \frac{C_d+C_{in}+C_f}{A_o}} \tag{6.3}$$

Where V_{out} is the output voltage, Q_{in} is the charge, C_f is the integrator capacitance, C_{in} is the input capacitance and C_d is the detector capacitance. The output voltage V_{out} reduces to:

$$V_{out} = -Q_{in}/C_f \tag{6.4}$$

for very large amplifications A_o. This means that the output voltage is linear to the charge deposited on the input. The input capacitance C_{in} is discharged through the resistor R that biases the high voltage to the detector. The charge on the capacitor C_f is discharged by the resistor R_f, in a characteristic time τ given by:

$$\tau = R_f \cdot C_f \tag{6.5}$$

The charge rate is defined as the number of pulses arriving at the amplifier per second (or count rate) multiplied by the average charge per pulse deposited on the amplifier. The charge rate of a charge sensitive amplifier is limited by the output voltage V_{out} which cannot exceed the power supply voltage of the amplifier. This means that the capacitor C_f should get enough time to discharge, which results in a limited charge that can be accepted per time interval.

We have used two different types of charge sensitive preamplifiers: Canberra types 2003BT and 2006. The former is used for the measurement of Q_T, the latter type is used for Q_E and Q_φ. The 2003BT delivers a fast timing pulse that can be used to trigger the ADC's. Some characteristics of these amplifiers are given in table 6.1.

	2006		2003 BT	
Amplification	0.3	V/pC	0.45	V/pC
Rise time	30	ns	18	ns
Fall time	50	μs	250	μs
Noise (C_{in} = 200pF)	$< 10^{-16}$	C	$< 2 \cdot 10^{-16}$	C
Bias voltage	5	kV	5	kV
Non-linearity	< 0.02	%	< 0.04	%
Charge rate	$2 \cdot 10^{-7}$	C/s	$9 \cdot 10^{-8}$	C/s
Input capacitance	1.0	nF	3.0	nF
Max. input charge	33	pC	22	pC
Max. output voltage	± 10	V	± 10	V
Rise time timing			< 6	ns

Table 6.1. Characteristics of the preamplifiers.

It is worthwhile to note that in our case C_f = 6.8 pF and R_f = 100 MΩ. The detector capacitance C_D is measured to be ≈ 210 pF. The input capacitance of the preamplifiers is ~ 1nF (Canberra 2006). The input rise time is about 30 ns (Canberra 2006), which means that, since the duration of the input pulse is about 1 ns, the preamplifiers need about 30 ns to reach their output voltage V_{out}.
The average number of electrons in a charge cloud will be about 10^6-10^7 (Chapter 4). This is a charge of 0.1 - 1 pC. From table 6.1 we conclude that the charge rate is limited to ~ 10^{-7} C/s which means that the preamplifiers can handle 10^5 - 10^6 cts/s.

The noise produced by the preamplifiers is a function of the input capacitance. This is shown in figure 6.4, from which we conclude that we have a noise of $8 \cdot 10^{-7}$ pC (RMS) which is equal to 0.5 mV (RMS) at the output of the preamplifier.

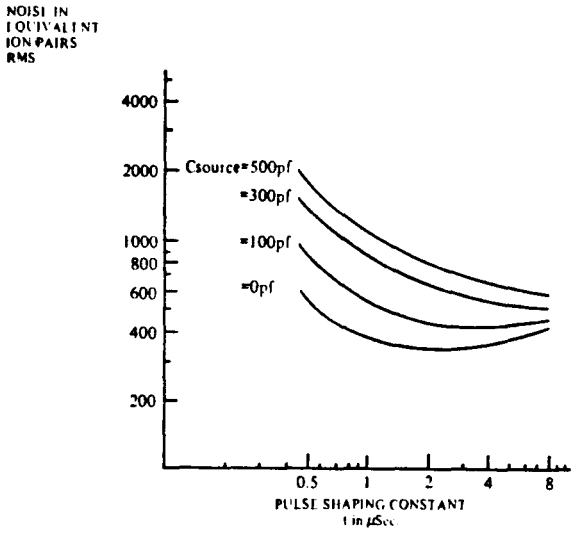

Fig. 6.4. Noise of a Canberra 2006 preamplifier as a function of the pulse shaping constant and the detector capacitance.

The voltage step produced by the preamplifiers is proportional to the collected charge on its input. Since the output voltage decreases slowly (typically in 50 μs), we have to shape the pulse in order to process it. This is done by the pulse shaping amplifiers Canberra 2110. These amplifiers convert the voltage step to a pulse of ~ 300 μs (depending on the integration and differentiation filters selected) with a pulse height linearly proportional to the voltage step (fig. 6.5). Pulse shaping is done by selecting the appropriate integrating or differentiating filters which range from 0 to 200 ns integration or differentiation time constants.

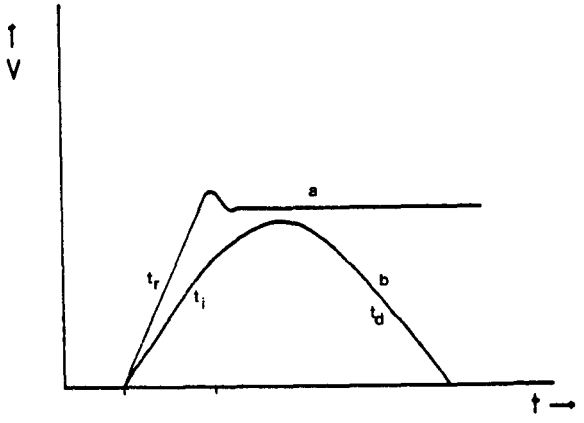

Fig. 6.5. Pulses from the preamplifier (a) with risetime t_r and from the main amplifier (b) with integration time t_i and differentiation time t_d.

Knibbeler [3] has shown that the pulse duration T of the 2110 amplifiers is about $T = 3 \cdot \tau_i + 3 \cdot \tau_d$, where τ_i and τ_d are the integration respectively the differentiation time constants. In order to eliminate the overshoot of the preamplifier signal (fig 6.5) we have to choose an integration time of roughly 3 times the preamplifier rise time constant.

Pulse pile-up occurs when two pulses are detected nearly simultaneously. Knibbeler has shown that at a count rate of $3 \cdot 10^5$ and a pulse duration of $T \sim 350$ ns, about 10% of the pulses has to be rejected to avoid pile-up effects. The elimination of piled-up pulses is done in the timing circuit (§6.7).

6.4 *High frequency interference suppression*

Charge sensitive preamplifiers have very sensitive inputs. Capacitive coupling of signals from other places of the system is easily possible. During our first measurements, we found a whole variety of different interferences on the outputs of our preamplifiers.

A major problem was to reduce this RFI to an acceptable level. In order to get some understanding of the mechanisms involved we first found out what RFI sources existed. Then we tried to understand the way in which they coupled their signal to the preamplifiers. Next we found ways to prevent the coupling of RFI to the preamplifiers.

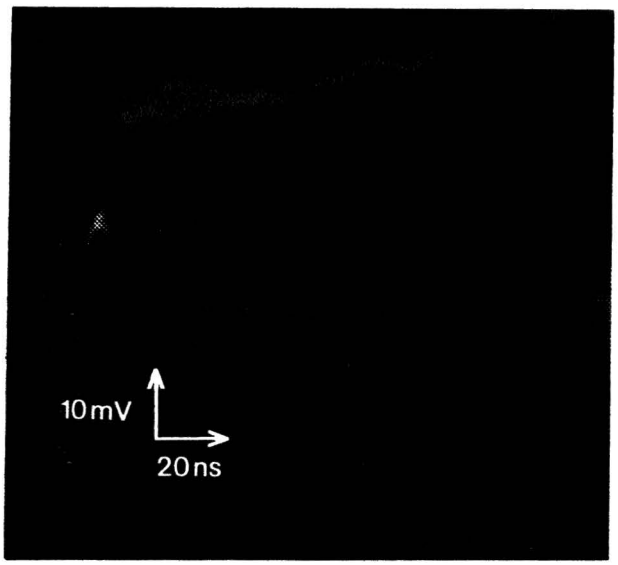

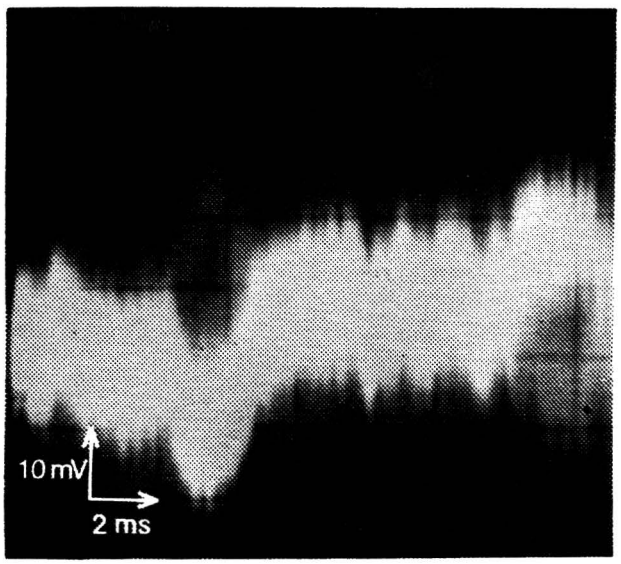

Fig. 6.6.a. Interference on the main amplifier output.
Fig. 6.6.b. 50 Hz pickup on the main amplifier output.

To begin with we photographed (fig 6.6.a) the noise at the output of a 2003BT preamplifier connected to a 2110 amplifier at maximum amplification and no integration or differentiation of the main amplifier. The small peak in the high frequency domain originates from the power supplies of the amplifiers. It has a repetition rate of 50Hz and a height of ~ 10 mV. It cannot be avoided, unless other power supplies are to be used. The low frequency 50 Hz signal is completely eliminated once we differentiate the signal with the pulse shaping section of the 2110 amplifiers. The minimum noise level we could possibly reach is therefore ~ 10 mV, with an exception of the small peak (fig 6.6.a). Connecting the preamplifier to the second channel plate resulted in a wide variety of RFI. Most prominent was the RFI coming from computers. Range: 16-20 MHz, amplitude 1V p-p. All high frequency apparatuses produced interference in this region: the Eurobus-PEP slave, the CADMUS-computer and several pulse generators. Other RFI sources with sharp peaks in a lower repetition frequency were found to be: the Eurobus power supply, the turbomolecular pumps of the sample introduction system and different power supply units using switching triacs (mostly Delta power supplies). In a low frequency domain the main interference source was 50 Hz pickup originating from ground loops (fig 6.6.b).

To find out how the different signals coupled to the preamplifiers we disconnected all supply lines to the vacuum system, except the lines between the second MCP and the charge sensitive preamplifier. Extra filtering of the power supply lines was also necessary (fig 6.7). Furthermore it was found that the lines to the preamplifier input should be as short and as well shielded as possible.

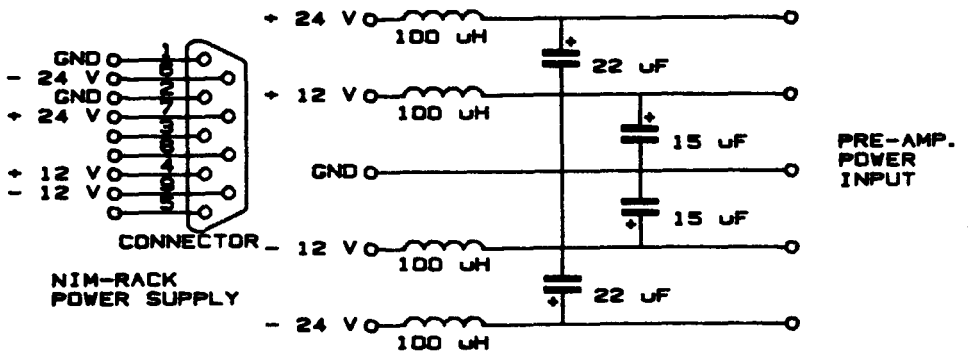

Fig. 6.7. Filters for the preamplifier power supply lines.

In order to suppress all 50 Hz pickup, we changed the 220V power supply to the whole EARISS-apparatus. We supplied the apparatus from one 380V-3 phase outlet. Each phase is rated for 25A at 220V which is sufficient to supply every instrument on the EARISS-apparatus. This solution at once eliminated the ground loops.

Once the grounding of the EARISS was proved to be correct and the power supplies to the preamplifiers were filtered, it became clear that the RFI signals could only be coupled to the preamplifier inputs from the inside of the vacuum system. Therefore we disconnected all wires from the vacuum system. Connecting one power line, e.g. of one of the analyzer segments, introduced a whole range of RFI. This could be understood in the following way. All H.V. lines had an 10 MΩ series resistor in them. This was done to protect the detector against electrical discharge (§4.5). These resistors were placed at a distance of 2m from the vacuum system. It turned out that this high impedance line functions as a pickup for RFI. This can be understood from figure 6.8. We detected a 16MHz signal with an amplitude of 1V p-p originating from the CADMUS computer on our charge sensitive preamplifier. With table 6.1. we can calculate the equivalent charge on the preamplifier input. This yields an input charge of $6 \cdot 10^{-13}$ C. If we take $C_{p1} + C_{p2} = C_p$ as parasitic capacitance and if we take the computer generating 5V p-p, we can then calculate C_p to be $\sim 10^{-2}$ pF.

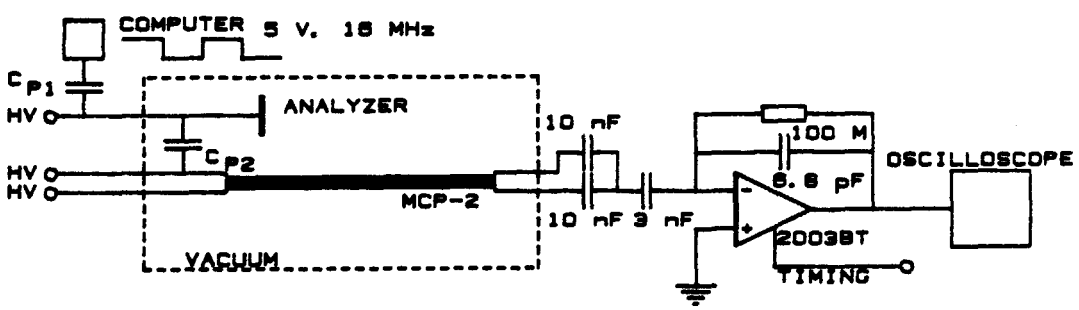

Fig. 6.8. Capacitive coupling of RFI to the charge sensitive preamplifiers in the vacuum system.

It is not possible to reduce parasitic capacitance C_{p2} since it is an inherent part of the analyzer system in the vacuum system. However it is very well possible to reduce C_{p1} by placing the 10 MΩ resistor right on the vacuum feedthrough thereby reducing the high-impedance

wire length. It turned out that the rest of the wire (L ≃ 12 m) also functioned as a RFI pickup. Therefore we developed low-pass filters which were placed on all analyzer and detector supply lines (fig. 6.9). These filters have two 3 dB-points, one at 1 Hz and one at 1 kHz. We have chosen for double filters since the 100 nF capacitors lose some of their filtering characteristics at high frequencies due to their inductance. The last resistor R_3 is solely ment for the protection of the interior elements. If a discharge would occur somewhere in the vacuum, the capacitors could deliver considerable amounts of energy. The resistor R_3 prevents the currents from becoming too large.

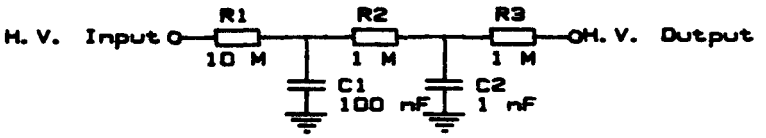

Fig. 6.9. Low-pass filters for the high voltage power supply lines.

Even after we filtered all lines to the vacuum system, we still found a considerable amount of RFI. It turned out that placing the filters in brass boxes and shielding all wires over their entire length using copper mantles connected to a central ground eliminated almost all RFI, except some 50 Hz pickup originating from the H.V.-supply rack (fig 6.1). This 50 Hz pickup could be eliminated using the scheme from figure 6.10. The 5 MΩ resistor was installed

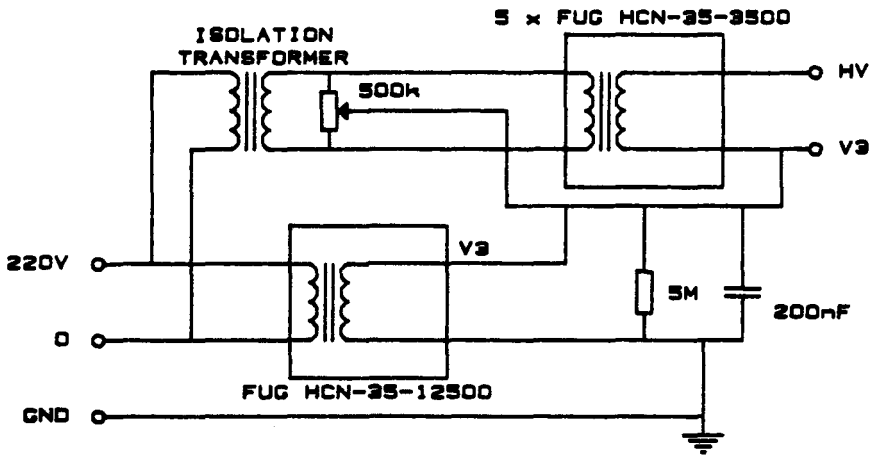

Fig. 6.10. Configuration of the 220V power supply to the analyzer/detector FUG's.

between V_3 and ground because the H.V. power supplies are much faster in stabilizing their output voltage if their output is loaded. The 200 nF capacitor is used to filter fluctuations in V_3 to ground. The variable resistor is used to compensate the asymmetric output of the isolation transformer. If V_3 is monitored on an oscilloscope, the variable resistor can be used to minimize the 50 Hz pickup.

In a later stage we discovered that the use of coaxial lines between preamplifiers and main amplifiers introduced an ground loop and consequently different kinds of RFI were detected. Wrapping the coaxial line around a ferrite ring removed the ground loop for high frequencies. The same problem occurred between the main amplifiers and the analog to digital convertors.

After all measures were taken to prevent RFI reaching our preamplifiers we again measured the noise level of the preamplifiers-main amplifiers (at full amplification). The result was a 50 mV noise level (compared to figure 6.6.a, 10 mV) with the RFI peak (fig 6.6.a) about 40 mV high. In the 50 Hz region, the interference level did neither significantly increase nor decrease. This is regarded as an acceptable level.

6.5 *Cross-talk*

A very important part of our investigations deals with the detection and prevention of cross-talk between the E- and φ-signals. Roughly speaking cross-talk can occur in two stages of the signal processing circuit. The first stage is in the collector itself and on the way from the collector to the preamplifiers. The second stage is cross-talk between the amplified signals from the preamplifiers and the computer system. The first stage will be most important because puls frequencies in this stage are the highest (1 GHz at 1 ns pulse duration). The amplified pulses in the second stage have lower rise times (~ 6...30 ns) and thus lower frequencies (~ 100 MHz).

The cross talk in the second stage is rather easy to check. We can apply a test signal on one of the preamplifier inputs and monitor the signal on all ADC's (With all preamplifiers disconnected from the system). At a frequency of 13 MHz a resonant frequency could be

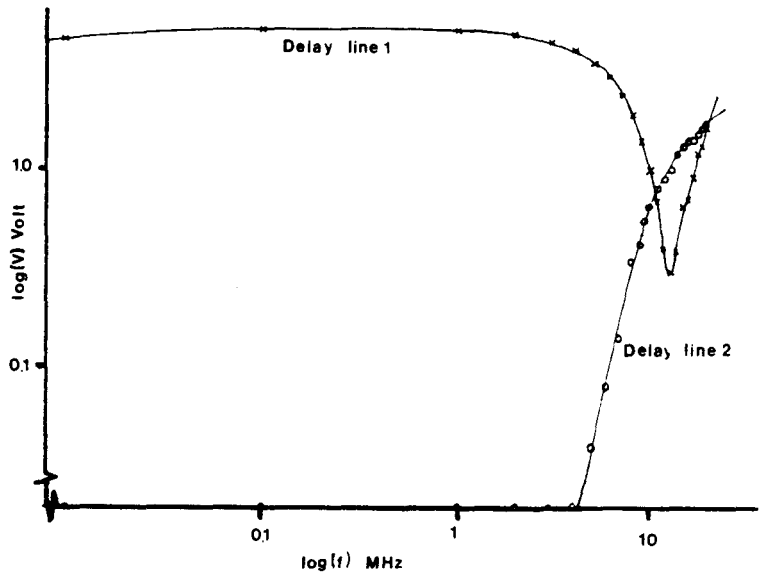

Fig. 6.11. RFI coupling between the delay lines. A sinus is applied to delay line 1. The output is monitored. At about 8 MHz the second delay line picks up RFI.

detected on the other amplifiers (fig. 6.11). After some experiments we discovered that the cross talk occurred between the delay-lines which are used for the timing of the signals (§6.6). Due to the length of coaxial-line used in the delay lines and due to the fact that they were placed close to each another, cross-talk could occur. The solution was to wrap part of the coax-line around a ferrite ring. No more cross-talk could be measured in this system which means that the level was below 10 mV.

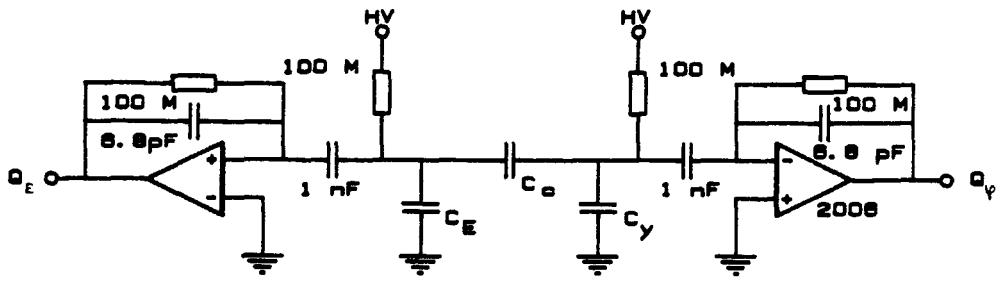

Fig. 6.12. Simplified scheme of the capacitive coupling of the collected charges on the collector.

The cross-talk occurring on the collectors is much more complicated. In figure 6.12 we have shown a simplified scheme of the charge collector and the preamplifiers. The capacitors C_E and C_φ represent the capacitance between the E- and φ-strips and the collector ground strip. The coupling capacitor C_c represents the capacitance between the E- and φ-strips. A charge cloud deposited on C_E will be distributed between C_c, C_E and the 1 nF input capacitor of the preamplifier. Through C_c some of the charge will also be deposited on C_φ and the 1 nF input capacitor of the other preamplifier.

In the first few ns (before the preamplifier starts to react) the input of the preamplifier is at an undefined potential. Therefore only the capacitors C_E, C_φ and C_c determine how much of the charge is coupled to the other preamplifier. Knibbeler [3] has determined that if the cross-talk has to be kept below 1%, C_E should be about 100 x C_c (the same holds for C_φ). There is however a difference between the charge deposited at C_E and C_φ. The charge on C_E is an actually deposited charge. The charge on C_φ is capacitively coupled through C_c. Therefore C_φ can lose its charge if C_E loses its charge. This happens at the moment the preamplifier becomes active. The charge on C_E is then transferred to the input capacitor of the preamplifier. This effect reduces the cross-talk of our circuit.

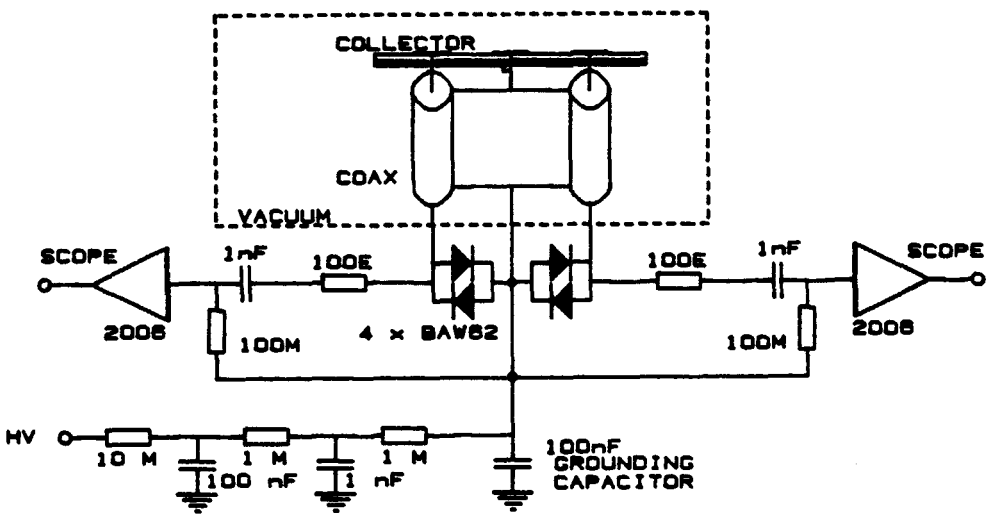

Fig. 6.13. Charge collector and connections to the preamplifiers. The antiparallel diodes are used for protection.

The circuit of our charge collector is somewhat more complicated. (fig. 6.13). The ground strip can not be connected to ground directly, since the charge collector is at a high voltage with respect to ground. Instead, we have to use a grounding capacitor that collects the charge deposited on the ground strips. This capacitor functions as a buffer, thereby reducing the cross-talk between the E- and φ-strip. The grounding capacitor should be taken at least 100 times larger than the capacitance between the strips. This capacitance was measured to be ~ 200 pF. We chose a grounding capacitor of ~ 100 nF.

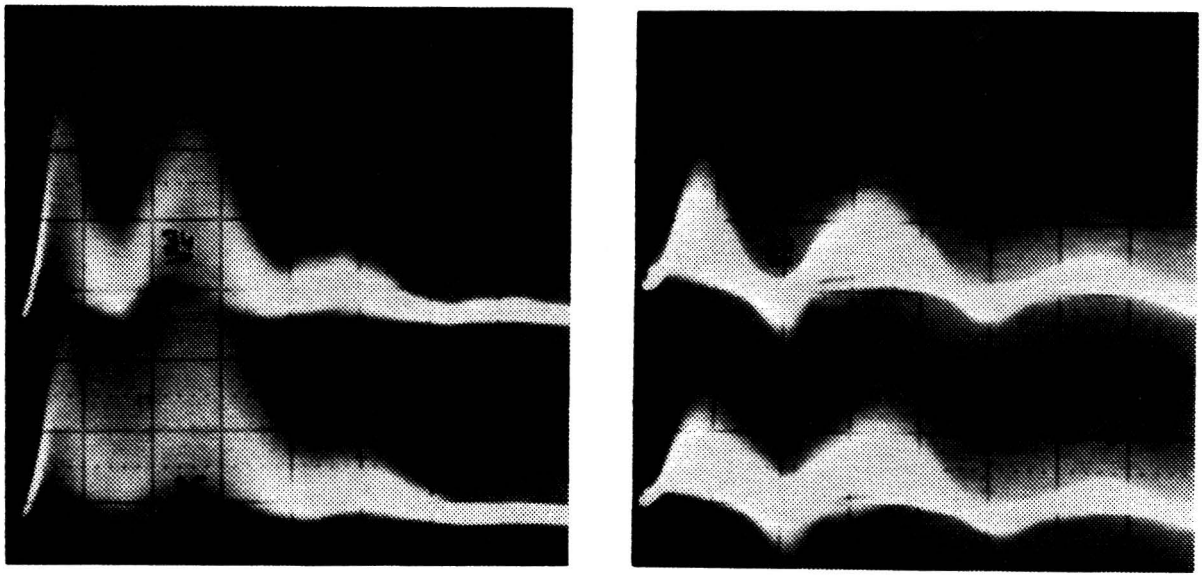

Fig. 6.14. Deformed pulses from the collector strips E and φ using (a) a 20 nF grounding capacitor and (b) a 100 nF grounding capacitor.

The antiparallel diodes in the scheme of figure 6.13 are meant to protect the charge collector in case a high voltage discharge occurs. They prevent the voltages between the strips from becoming larger than ~ 0.6 V. The pulses we measure at this point show some characteristic fluctuations (fig. 6.14). It seems that the value of this capacitor influences the frequency of these fluctuations. We observed a resonant frequency of about 15 MHz in our pulses. Later we discovered that it was not the value of the capacitor that caused the fluctuations but it was the inductance inherent to each capacitor. We should therefore use a capacitor placed as close to our charge collector as possible.

Besides we should choose a capacitor with a low inductance. It turned out that these two measures were not enough. This can be understood if we realize that the coaxial lines in the vacuum system also have an inductance (fig 6.13.). If we take the inductance of a wire to be ~ 0.8 nH/mm, we have a total inductance of ~ 300 nH per line (fig. 6.13.). The resonance frequency of a LC-circuit is given by

$$f = \frac{1}{2\pi\sqrt{LC}} \qquad (6.6)$$

If we take C = 200 pF and H = 300 nH we can calculate this frequency: f ≃ 20.5 MHz, which is quite close to the measured resonance frequency. All connecting wires to the charge collector should be kept as short as possible, thereby having a low inductance. The connection between the ground strip and the backplane of the collector was previously made using a fine 0.02 mm diameter gold wire. This wire has been replaced by a thick gold strip with a low inductance (fig. 6.15).

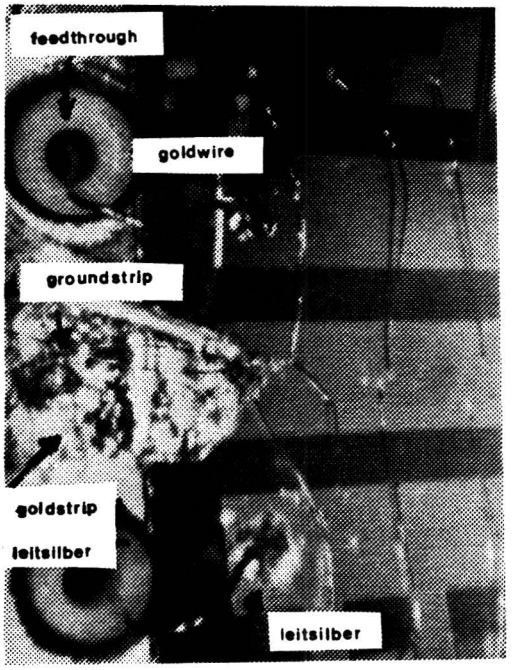

Fig. 6.15. Connecting strips to the charge amplifiers. The ground strip is connected with a gold strip to the backing of the collector.

There is a way of reducing the amplitude of the remaining resonances by placing a 100 Ω resistor in series with the input of the charge sensitive preamplifiers (fig. 6.13). The disadvantage is that the rise time of our pulses becomes longer. This means that we have to adapt the integration and differentiation time constants of our main amplifiers to 100 ns each, thus yielding a pulse with a duration of ~ 600 ns. This is still acceptable. This pulse duration does not decrease the maximum countrate since the process-time of a pulse in the digital system is about 1 μs.

6.6 *The timing circuit*

The preamplifier Canberra 2003 BT supplies a fast 20 ns timing pulse. This pulse can be used to trigger a logic circuit that determines whether the event should be measured or whether it should be neglected if the pulse is too small. A second function of this circuit is to determine whether a second pulse has arrived and to inhibit the processing of this pulse if the time interval between the two pulses is to short for the digitization to have taken place. The third function of the circuit is to supply a trigger pulse to the ADC's at the maximum amplitude on the ADC's inputs. The timing circuit and the time scheme are given in figure 6.16 respectively in figure 6.17.

The timing pulse from the Canberra 2003 BT is fed into a main amplifier which also inverts the pulse. This is done because the Constant Fraction Discriminator (CFD) only accepts negative pulses. The CFD has two functions. Firstly it is able to discriminate pulses that are too small. Since the timing output pulse of the 2003 BT is proportional to the charge detected in its input, this pulse can be used for discrimination purposes. Secondly the CFD generates a timing pulse at exactly the moment when the input pulse has reached a fixed fraction of its total amplitude. This means that the timing pulse is always generated at the right moment, independent of the amplitude of the pulse. The CFD generates two logic outputs. One fast negative pulse is directly fed to a Fast Slow Coincidence (FSC) circuit. The other somewhat slower positive pulse is used to trigger a pulse

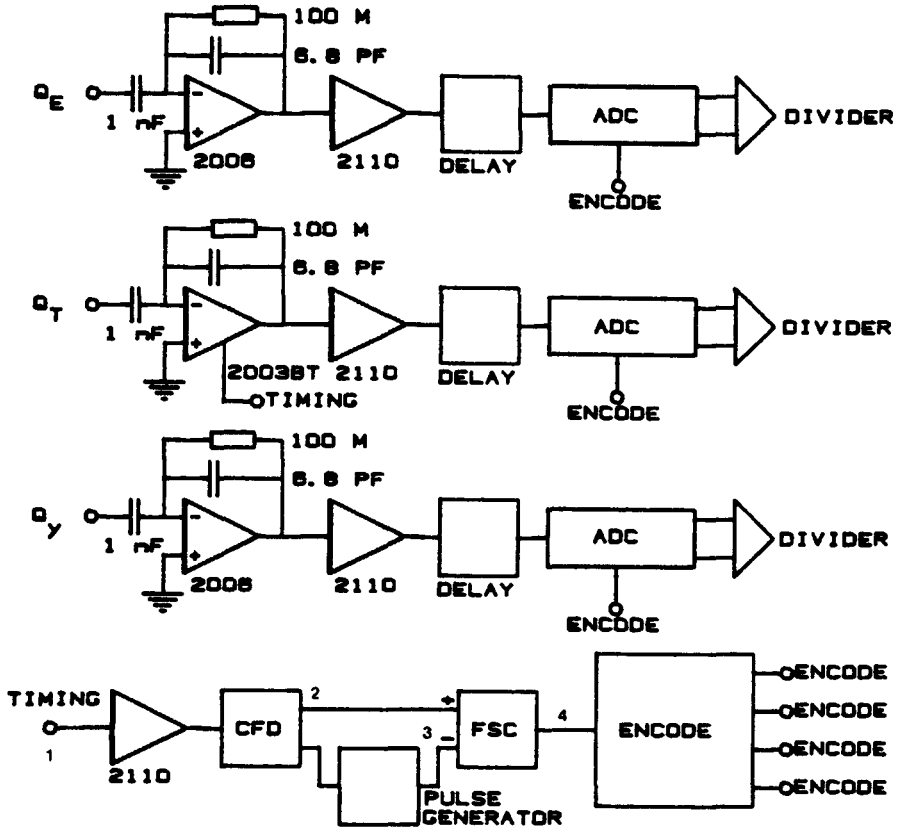

Fig. 6.16 The amplification circuit, showing the preamplifiers, the main amplifiers, the delay lines and the ADC's. The timing circuit processes the timing pulses from the 2003 BT and determines whether the ADC's are triggered.

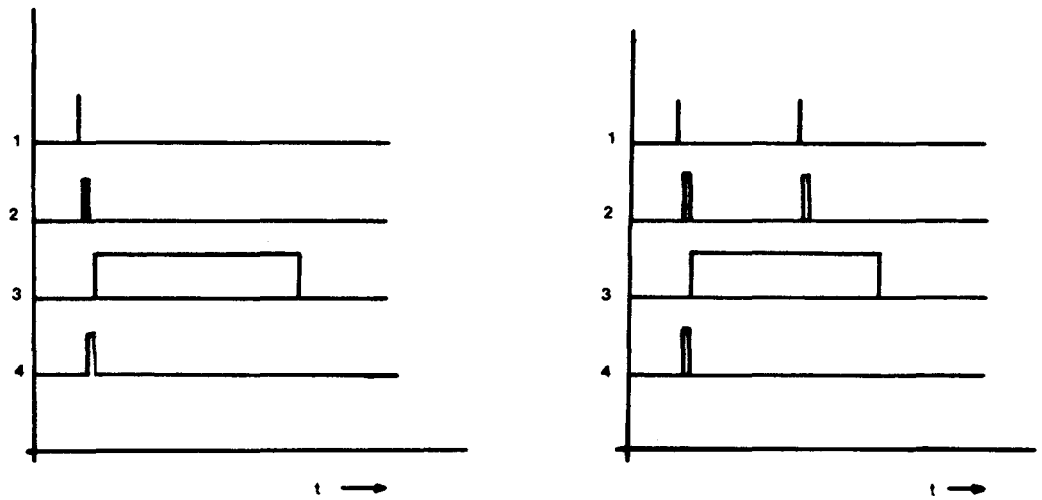

Fig. 6.17. Time diagram of the pulses in the timing circuit. The second figure shows the elimination of a pulse arriving during the processing of the previous one. The numbers in the diagram correspond to the numbers in fig. 6.16.

generator. This pulse generator generates a logic output pulse with a length of 1.1 μs which is somewhat longer than the time our digital circuit (chapter 7) needs to process an event.

An FSC is in fact a logical AND with 5 different inputs. It can detect coincidences or anti-coincidences of very short (> 5 ns) pulses. Each input has three different settings: inverting, non-inverting, and disabled. The FSC inputs accept both positive slow or negative fast pulses. The FSC generates a pulse at the moment a coincidence is detected. No output pulse is generated if at the time of a coincidence one of the inverting inputs detects a pulse.

The FSC determines whether a trigger pulse should be supplied to the ADC's or not. The pulse from the pulse generator will arrive 20 ns later than the pulse from the CFD (fig. 6.18). This means that the FSC will generate a logic 150 ns pulse. If the CFD detects a next pulse within the 1.1 μs set by the pulse generator, this pulse will not trigger the FSC since the negative input is still high. Only if two pulses arrive on the 2003 BT within 20 ns, it is not possible for the timing circuit to detect such an event. The probability of this event happening is, even at countrates up to 10^6 cts/s, small. (Poisson distribution: probability $\simeq$ 0.02). This means that 2 out of 100 detected counts are false, which we find acceptable. This timing circuit was preferred to the one suggested by Knibbeler [3] because he uses the output of the main amplifiers to detect pile-up. This means that the pulse duration is much longer which makes it harder to distinguish piled-up pulses.

The timing pulse generated by the FSC is split into four equivalent timing pulses by the MCA controller (Chapter 7). Three of these are used to trigger the ADC's and one is used to trigger the digital circuit.

The timing circuit requires about 100 ns to detect an event and to determine whether it should be accepted. This means that the pulses of the three amplifiers have to be delayed. The ADC's are triggered at the positive going edge of the pulse from the FSC. This edge has to coincide with the maxima of the pulses from the main amplifiers.

The delay lines we used consist of RG 172U-coaxline, with a length determined by a set of switches. This enables us to select delay times from 3 to 258 ns. At the maximum delay time of 258 ns about 50% of the

signal amplitude is lost. No measurable reflections or dispersion occurred. The loss in amplitude can be compensated by a higher gain of the main amplifiers. The ADC's require pulses with an amplitude of 0 - 1 V.

6.7 *References*

[1] **C.L.C.M. Knibbeler**, LEIS-memo 23, Eindhoven University of Technology. (1983).

[2] **G. Lutz et al.**, Nucl. Instr. Meth. A263 (1988) 163.

[3] **C.L.C.M. Knibbeler**, Masters Thesis, Eindhoven University of Technology, (1983).

Chapter 7. Digital Electrical Circuit.

7.1 Introduction

The fractions of the electron cloud falling on the E- and φ-strips are measured and amplified. As we discussed in chapter 5 these fractions have to be normalized to the total charge in the electron cloud. There are two ways in which this division (according to equation 5.3) can be done.

Firstly we can use an analog divider. These dividers achieve an accuracy of 0.2% over a 10:1 dynamic range in the total charge [1]. Analog dividers of this kind require a settling time of 1 μs to reach a stable output voltage with the desired accuracy. This means that counts up to 10^6 cts/s can be handled.

We have chosen a second division method. This method uses the digitized pulse amplitudes. A digital circuit allows us to calculate the ratio of the measured charges. To reach the required accuracy of 1% we need at least an 8 bits analog to digital convertor (ADC) for each pulse. Its conversion time should be smaller than 1 μs. We have chosen 8 bits flash ADC's (Analog Devices MATV 0811), with a conversion time of 150 ns and an accuracy of 0.2% $\pm$ 1/2 least significant bit. The input is digitized 3 ns $\pm$ 30 ps after a trigger pulse has been received.

The ratio of the charges can be calculated from the digital numbers. This process is described in section 7.2. The two calculated ratios (R and φ coordinate) are combined to an address in the memory of a Multi Channel Analyzer (MCA) (§7.3). The number at this address is incremented by 1. At the end of the measuring cycle, the MCA-memory contents can be transferred to a computer system (§7.4).

7.2 Concepts of very fast divisions

The digitized ADC inputs can be divided by each other in two ways: by hardware or by software. Using the software division one computes the result of a division with a microprocessor. The result of the division can be used as an index to an array. This array element is incremented by one each time it is accessed. Such a computation would require a lot of time to process (typically 10-20 μs). This reduces the maximum countrate considerably.

Using hardware dividers is another possibility. The answers to all possible divisions are calculated once. These answers are then stored in a memory. The two digital numbers which have to be divided are combined to one address. The answer to the division is then found at the address in the preprogrammed memory. This is called a look-up table. The result found at the address is used to form an address in a accumulation memory where the result is used as a new address. The contents of this address is then incremented by 1. This second memory is the multichannel analyzer memory. We have chosen the hardware division method. Processing times lie around 1 μs.

Each 8 bits ADC yields 2^8 = 256 possible numbers. Therefore the lookup table should contain $2^8 \cdot 2^8$ = 64 kBytes (kB) addresses. A few years ago this kind of memory was not readily available. At that time a first look-up table was tempted using Programmable Read Only Memories (PROM's) [2]. In a later stage this setup was abandoned due to its inflexibility: it is possible to change the contents of a PROM but this requires a lot of effort and time. A more flexible look-up table can be build using a 64 kB Random Access Memories (RAM's) [3].

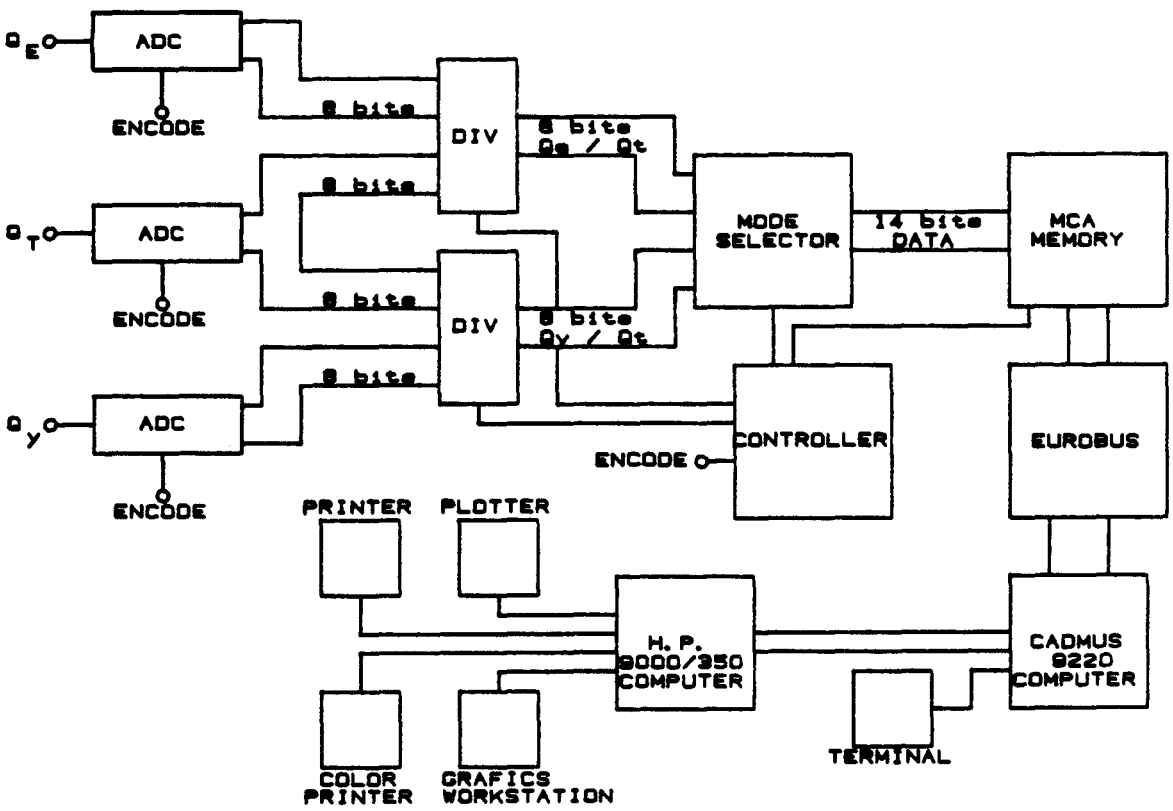

Fig. 7.1. Schematic diagram of the digital system showing the ADC's, the divider memories, the male selector and the MCA memory.

Two divisions have to be calculated (§5.3), which means that two 64 kB RAM's have to be used (fig. 7.1). The two answers obtained from these memories represent an azimuth and an energy. These two answers are again combined to one address in the two dimensional MCA-memory. This address content is now incremented by one, meaning that one ion of a certain energy and angle has been detected.

Since this whole cycle of dividing the ADC outcome and incrementing the MCA memory takes about 1 μs, a maximum countrate of 10^6 counts per second can be obtained.

7.2.1 The analog to digital converters

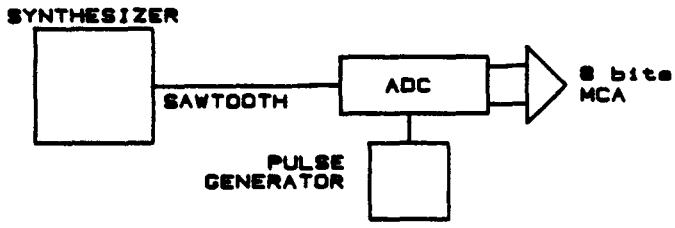

Fig. 7.2. Test setup for the ADC's.

The digitization process and the subsequent division introduce some artifacts in our system. The ADC's used are not completely linear. A simple test (fig. 7.2) in which we applied a sawtooth voltage of 0 to 1 V, 100 Hz at the ADC inputs and an independent trigger pulse with a 100 kHz repetition frequency, showed that the three ADC's did not produce an homogeneous distribution in all channels as we would have expected (fig. 7.3.a,b,c). From figure 7.3 we see that channels with an index of a power of 2 or manifolds of 2 have an higher number of counts than we expected. This means that our ADC's have to be tuned. An ADC is supposed to split the interval between 0 and 1 V in 255 equal parts. The most significant bit determines whether the input lies above or below 0.5 V. The second bit determines whether the input is above or below 0.25 V or 0.75 V etc. If the splitting of an interval in two parts is done asymmetrically, (e.g. 0-0.45 V and 0.45 V to 1 V instead of 0-0.5 V and 0.5-1 V) we expect most counts to be detected in the largest interval. In figure 7.3.a. we see that some of the least significant bits have to be

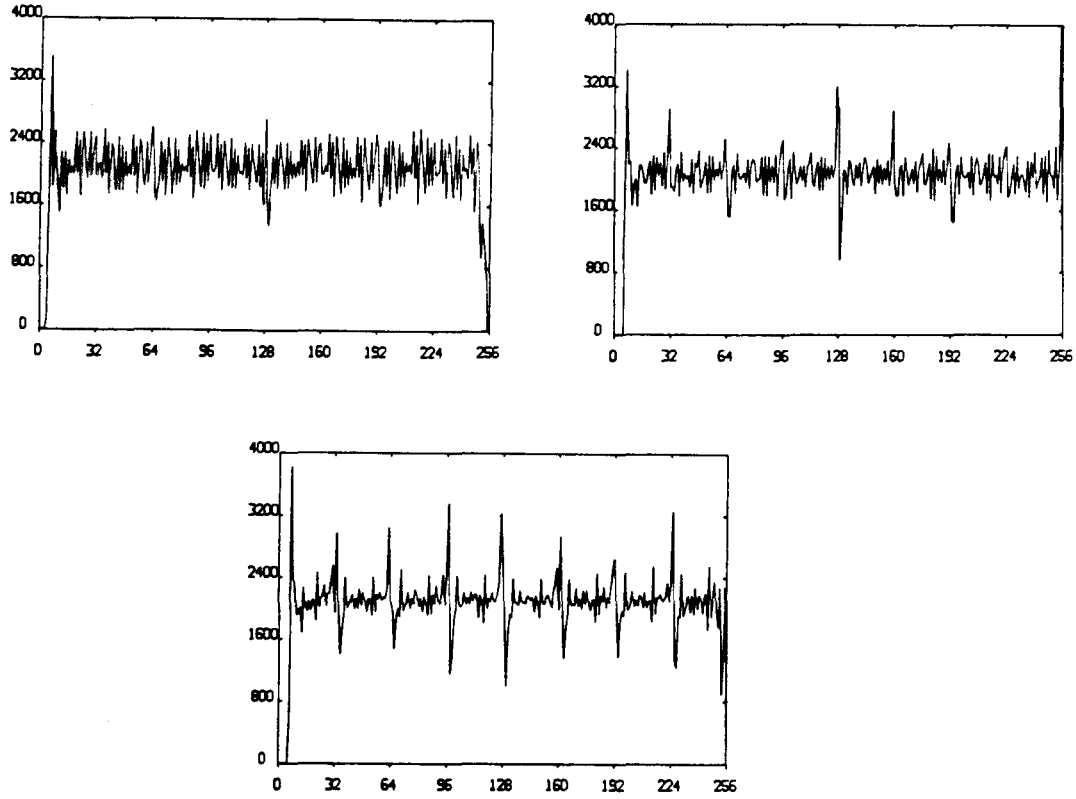

Fig. 7.3.a,b,c. Digital output of the ADC's with sawtooth voltage applied on their inputs.

adjusted, in figure 7.3.b. we see that the first second and third bit require adjustment and in fig. 7.3.c. we see that the third bit needs adjustment. A suitable calibration procedure should be developed in the near future to reduce these artifacts.

7.2.2 *Theory of integer division*

A far more fundamental problem occurs if we calculate the answers to a division of integer numbers [4,5]. Even if we would have an homogeneous input from our ADC's not all answers are equally likely to occur. This can be explained in the following way: The division we would like to calculate is given by:

$$E = A / B, \qquad 0 \leq A < B \tag{7.1}$$

where A and B are given by two 8 bits integers coming from our ADC's. The restriction $0 \leq A < B$ originates from the fact that the total charge emitted from the channel plate is always larger than the charge collected on a strip.

Using (7.1) however yields a fraction somewhere between 0 and 1. this can not be represented by an 8 bits integer. We multiply the resultant fraction of (7.1) by an integer value 256, thereby shifting the whole answer 8 bits to the left:

$$E' = 256 \cdot A / B, \qquad 0 \leq A < B \tag{7.2}$$

A multiplication by 256 however causes serious problems. When we evaluate all possible sets of A and B yielding a certain value of E', we discover that the distribution N(E') is not homogeneous (fig. 7.4.). Sharp peaks occur at powers of 2 and at multiples of 2.

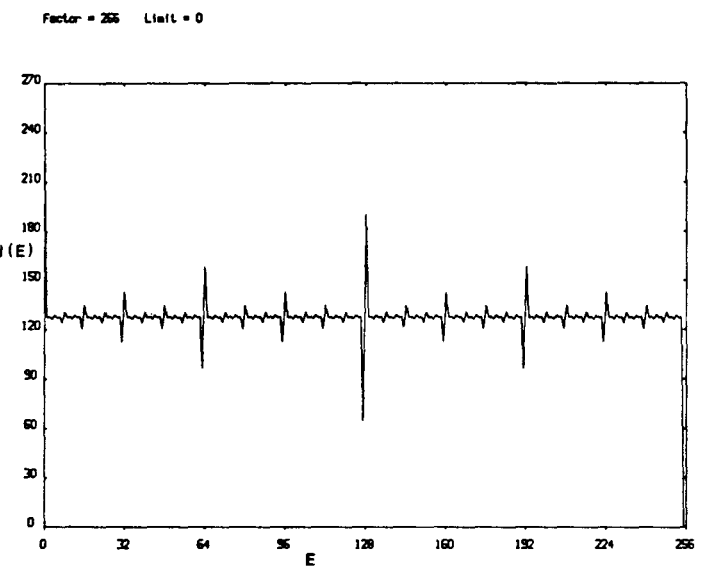

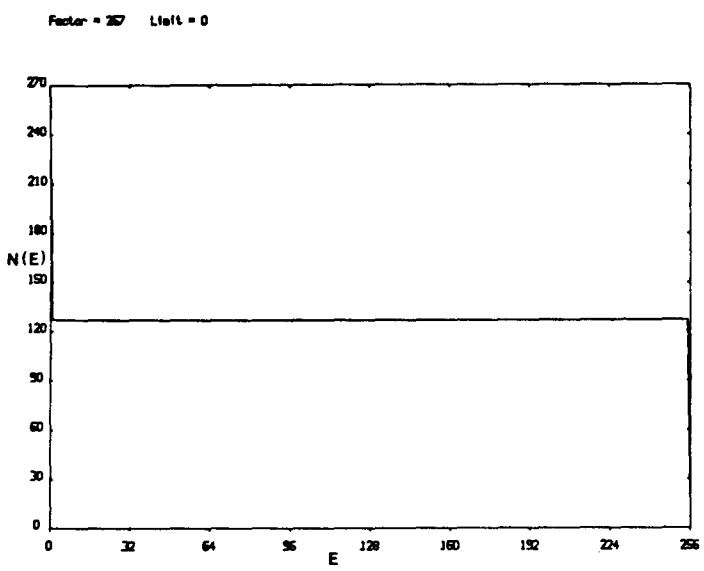

Fig. 7.4. Distribution of the division $E = 256 \cdot A/B_0$.
Fig. 7.5. Distribution of the division $E = 257 \cdot A/B$.

Since the peaks occur at powers of two it was thought that the number 256 has something to do with this effect. We replaced the multiplier 256 by 257 (which is a prime number). This multiplier yields a straight distribution (fig. 7.5.). What happens can be simplified using the following scheme. Suppose we have two 4 bits integers, say A and B. If A is always smaller than B, the division of A/B•16 does not deliver an homogeneous outcome. Let E = A/B•16. All possible outcomes E and their frequency N(E) are listed in table 7.1.

E=f*A/B	N(E) (f=16)	N(E) (f=17)
0	15	15
1	7	7
2	8	7
3	6	7
4	9	7
5	7	7
6	8	7
7	4	7
8	11	7
9	7	7
10	8	7
11	6	7
12	9	7
13	7	7
14	8	7
15	0	7

Table 7.1 Distribution of f•A/B.

In the third colum of table 7.1 we have shown the same division using a multiplier factor f = 17 instead of f = 16.

The use of a prime number as a multiplier is not the whole answer to this problem. If we calculate all answers of the division A/B•17 (0 ≤ A < B) and we write them down for each number B, we obtain:

B \ A	0	1	2	3	4	5	6	7	8	9	10	11	12	13	14
1	0														
2	0	8													
3	0	5	11												
4	0	4	8	12											
5	0	3	6	10	13										
6	0	2	5	8	11	14									
7	0	2	4	7	9	12	14								
8	0	2	4	6	8	10	12	14							
9	0	1	3	5	7	9	11	13	15						
10	0	1	3	5	6	8	10	11	13	15					
11	0	1	3	4	6	7	9	10	12	13	15				
12	0	1	2	4	5	7	8	9	11	12	14	15			
13	0	1	2	3	5	6	7	9	10	11	13	14	15		
14	0	1	2	3	4	6	7	8	9	10	12	13	14	15	
15	0	1	2	3	4	5	6	7	9	10	11	12	13	14	15

Table 7.2 Answers of the division 17•A/B, with 0 ≤ A < B

From table 7.2 we can conclude that a homogeneous distribution is only obtained if all values of B are taken into account. If B = 15, each answer to the division 17•A/B occurs nearly one time. Only the number 8 is still missing in this row. When B gets smaller (moving upwards in table 7.2), more and more numbers do not appear in the row. This means that the distribution of answers in a row is not homogeneous. However if we count the occurences of the answers in the whole table, we see that each answer occurs exactly 7 times. This yields the homogeneous distribution of the third colomn in table 7.1.

We could use a multiplication factor smaller than 17. Using the number 8 as multiplier again yields the same inhomogeneous distribution as we observed earlier using the factor 16 (table 7.3). However if we use a factor f = 7 we obtain a homogeneous distribution, as we can see from the second colomn in table 7.3:

E=f×A/B	N(E) (f=8)	N(E) (f=7)
0	22	24
1	14	17
2	16	17
3	12	17
4	18	17
5	14	17
6	16	11
7	8	0

Table 7.3 Distribution of the answers to the division E = f•A/B.

It is now possible to make the same table as we did for f = 17. This is done in table 7.4. In this table we can see that from B = 7 to B = 15 each possible answer occurs at least one time in every row. For B < 7 we observe that in each row one or more answers are missing. Furthermore we note that the missing answers start occuring at exactly the row number which equals the multiplication factor. We should therefore restrict ourselves to a dynamic range of $f \leq B \leq 15$. The number of times an answer appears in each row can be observed from table 7.4. The inhomogeneity in each row can therefore be corrected for afterwards. This means that the number of times each row occurs should be known.

For example: if we take B = 10 and we have a homogeneous distribution of numbers A, we obtain twice as many occurrences of the results 0,2 and 4 as of the results 1,3,5 and 6. This means that if the row B = 10 occurs during a measurement, we should multiply the number of times the answers 1,3,5 and 6 appear by a factor 2.

These inhomogeneities become less important if the number of bits of A and B becomes larger and we are allowed to ignore more bits.

B \ A	0	1	2	3	4	5	6	7	8	9	10	11	12	13	14
1	0														
2	0	3													
3	0	2	4												
4	0	1	3	5											
5	0	1	2	4	5										
6	0	1	2	3	4	5									
7	0	1	2	3	4	5	6								
8	0	0	1	2	3	4	5	6							
9	0	0	1	2	3	3	4	5	6						
10	0	0	1	2	2	3	4	4	5	6					
11	0	0	1	1	2	3	3	4	5	5	6				
12	0	0	1	1	2	2	3	4	4	5	5	6			
13	0	0	1	1	2	2	3	3	4	4	5	5	6		
14	0	0	1	1	2	2	3	3	4	4	5	5	6	6	
15	0	0	0	1	1	2	2	3	3	4	4	5	5	6	6

Table 7.4 Answers of the division 7•A/B, with $0 \leq A < B$.

7.2.3 *Practical aspects for EARISS*

We can summerize the effects we described above and discuss what they imply for the EARISS divider process. We have noted that multiplying the division of Q_E/Q_T by a prime number yields a homogeneous distribution of answers. However for Q_T smaller than the multiplier we do not obtain all possible answers. This means that answers with a Q_T smaller than the multiplier should not be taken into account. We have chosen a multiplication factor f = 101. We thus do not accumulate counts with a Q_T smaller than 101, thereby avoiding the effect that some answers do not appear for small Q_T's. This corresponds to that we limit ourselves to the upper part of table 7.4. taking $B \geq 7$. It means that we have a dynamic range of about a factor 2.5 in Q_T.

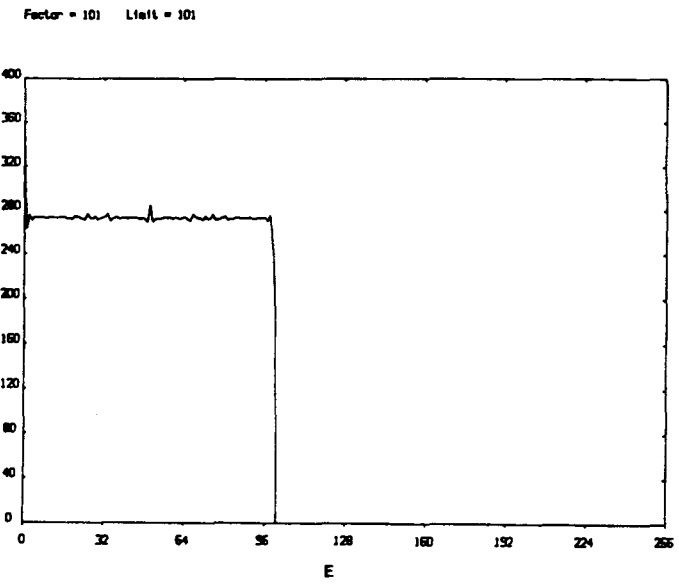

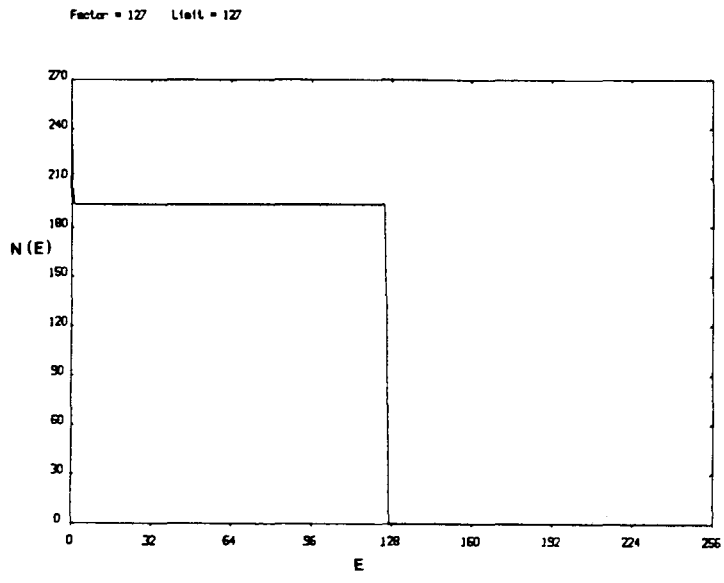

Fig. 7.6.a. Distribution of the division $E = 101 \cdot A/B$ with a lower limit $B \geq 101$.

Fig. 7.6.b. Distribution of the division $E = 127 \cdot A/B$ with a lower limit $B \geq 127$.

In figure 7.6.a we have shown the distribution of answers which we obtain using a factor 101 and a lower limit also set to 101. It is clear that although the result is already much better than the distribution shown in figure 7.4, it still is not optimal.

In effect, it would have been much better to take a factor f = 127 and thus also a lower limit of 127 (fig. 7.6.b). This was however not possible. We needed a way of signaling false counts. These are counts that have a $Q_E \geq Q_T$ (implying an improper amplification), or a $Q_T = 0$ (implying a false trigger pulse from the timing circuit), or (which is new) a $Q_T < 101$. In our dividers we have used the number 127 for signaling those false counts, which means that the number 127 is not free to be used as a multiplication factor.

In figure 7.7 we have photographed the computer screen showing an intensity distribution in the MCA memory. The figure was made by applying a sawtooth voltage from 0 to 1 V onto the ADC's used for measuring Q_E and Q_φ and by applying a DC voltage of 1 V on the ADC used for Q_T. The photograph shows quit clearly that powers of 2 are still dominant. We would have expected an almost homogeneous distribution in both the X and Y direction, however variations of over a factor 3 in the number of counts can be observed. Corrections for this effect will be added to the software.

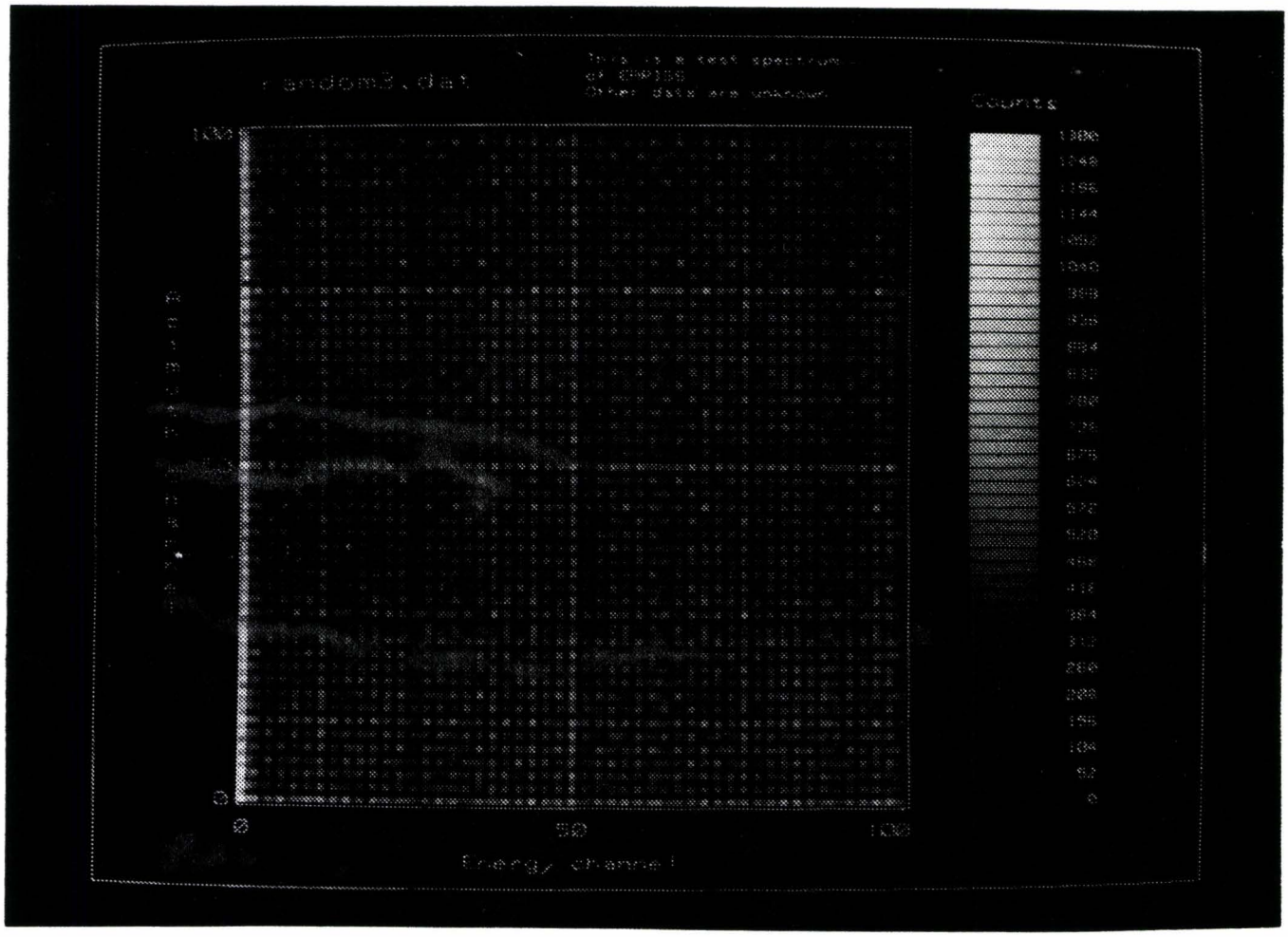

Fig. 7.7. Contents of the two-dimensional MCA memory with a homogeneous input on both the azimuth and energy channel. Channels equaling manifolds of 2 are prominent.

The consequence of the effect discussed above is that we lose part of the dynamic range in Q_T. This disadvantage is however compensated by a gain in the divider resolution. A solution to this loss in dynamic range would be to use 10, 11 or even 12 bits ADC's [6]. This would also require larger divider memories of $2^{2 \cdot 10}$ bytes (1 MB RAM) in case 10 bits ADC's are used. We could then ignore the last three bits of the division result by using a multiplication factor of 127 and thus also setting a lower limit of 127. The loss of those bits is compensated by a gain in the dynamic range of Q_T by a factor 4. (Q_T ranges from 127 to 1023 in stead of ranging from 101 to 255 with 8 bits ADC's).

Another part of the solution to this problem is to record simultaneously the pulse height distribution of Q_T. This would require an extra memory board of 64 kB. However this pulse height distribution could also automatically be measured after the MCA memory has been filled. The obtained pulse height distribution can then be used to correct for the number of times each row (B) has appeared in the look-up table. The inhomogeneous distribution of each row can then be corrected for. More insight in these phenomena is needed to determine the optimal solution to this problem.

The conclusion should be that the product of the dynamic range in the denominator and the accuracy of the calculated division is a constant. Increasing the dynamic range by using a larger multiplication factor automatically result in a lower resolution of the calculated answers unless more bits are to be used.

7.3 The MCA memory and controller interface

The output of the ADC's is transported to the two divider memories. The two divisions Q_E/Q_T and Q_φ/Q_T yield two 8 bits integers. These integers represent an energy and an azimuth (fig 7.1). The two 8 bits integers are combined to an address in the MCA memory. However this MCA memory uses only 14 bits addresses. Therefore two bits have to be truncated. The reason why only 14 bits addresses are used is the following: Since we would like to accumulate over 10^5 counts per second each MCA address should be able to contain enough counts. Making use of the same memory boards as we used for the dividers (64 kBytes, 8 bits RAM) would allow us only $2^8 = 256$ counts per address which is not nearly enough at such count rates. However these memory boards can be programmed to 32 kbytes, 16 bits RAM or 16 kbytes 32 bits RAM. The former setting would allow for $2^{16} = 65536$ counts per address and the latter setting would allow for over $4\ 10^9$ counts per address, which is sufficient for our measurements. A 16 kB memory uses 14 bits addresses. The truncation of the last two bits is done in the Mode Selector (MS). The MS enables us to choose the number of bits used for the energy or for the azimuth. We could for example use 7 bits for the energy and 7 bits for the azimuth, thus one bit of each divider result is lost. Another possibility would be to use 6 bits for the energy and 8 bits for the azimuth or vice versa. This means that

we have some freedom to choose the accuracy in the energy or azimuth direction. However a higher accuracy in the energy direction automatically implies a lower accuracy in the azimuthal direction.

The controller interface (fig 7.1) is the central part of the digital system. It controls the flow of data between the ADC's the dividers, the MCA memory and the MS. The controller is a state sequencer. This means that a measuring cycle is started at the moment a trigger pulse is generated by the timing circuit. This pulse triggers both the ADC's and the controller interface. The controller uses 50 ns clock pulses. After 350 ns the controller transports the data from the ADC's to a buffer register (fig 7.8.). The dividers read

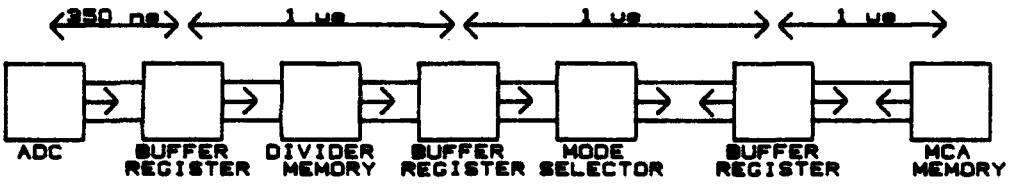

Fig. 7.8. Pipe line showing the transport of data from the ADC's to the MCA Memory.

the data from these registers and transport the result in the look-up table to a second buffer register. The MS reads the data from these second buffers and combines them to a 14 bits address. Next, the MS reads the contents of the selected address from the MCA memory. This number is then incremented by 1 and the result is written back to the same address in the MCA memory. In this way the MCA memory is filled. The computer is able to stop the controller after which the accumulated counts in the MCA memory can be read.

The controller enables the digital system to accept a second pulse at the moment the previous count has left the dividers This is called a pipe line. It means that it is not necessary for the digital system to wait for the whole storage process to have finished, but new pulses can be accepted after the division has taken place, which in theory is after 1 μs. This means that countrates of 10^5 to 10^6 can be handled. We have shown that a countrate of 4 10^5 is about the maximum we can handle at this moment.

A more detailed description of the MCA memory the controller interface is given in by Dijkstra [7] and Knibbeler [8].

7.4 Computer interfaces and control

All parts of the digital system (the divider memories, the mode selector, the MCA memory and the controller interface) are connected to an Eurobus system [9]. The Eurobus system is a real time measurement system meant for data acquisition in laboratory experiments. It consists of a whole range of exchangeable modules such as scalers, digital to analog convertors, ADC's (not the special ones we use), liquid crystal displays, memory boards, steppermotor interfaces etc. All these modules are connected to a data / address bus (Eurobus). This bus can be controlled and addressed by a computer system. We have used a Cadmus 9220 computer (1 MB RAM, 40 MB Harddisk) with a LSI11-bus (Q-bus) to Eurobus converter. This computer uses the UNIX-System V operating system which was modified and extended for real time operations. The computer generates the look-up table for the divider memories, it sets the Eurobus system to the right starting values and it enables or disables the data acquisition. At the end of each measuring cycle the computer reads the data collected in the MCA memory and stores them onto the harddisk. This enables a later treatment of the datafiles.

The MCA memory contains a two dimensional height map of the accumulated counts in the energy and azimuthal direction. There are several ways of looking at such a map. We could for example take one single energy channel and plot the measured counts as a function of the azimuthal angle, or vice versa. It is also possible the sum all channels in one direction thereby obtaining an overview of all occuring energies or azimuths.

In the last stage of our experiments we were able to use another computer (Hewlett Packard 9000/350). Since this computer also uses the UNIX operating system we were able to transfer our datafiles directly to this computer system without making any changes. The HP 9000 computer supports a high resolution color graphics monitor (1024 x 786 pixels) and a color graphics printer (Paintjet) plus the associated software.

The two dimensional height map of the MCA memory can be presented on this screen using color as a representation for number of counts. Another way of presenting the MCA contents is by making a three dimensional picture. Examples of this will be shown in the next chapter.

7.5 Refences

[1] **M. Lampton and F. Paresce,** Rev. Sci. Instr. 45 (1974) 1098.

[2] **P. v. Dinther**, Internal Report VDF/CO 82-15, Eindhoven University of Technology (1982).

[3] **W.M. Dijkstra**, Internal Report VDF/CO 84-15, Eindhoven University of Technology (1984).

[4] **H. Ottevanger**, Private Communications.

[5] **H. Ottevanger**, Ph. D. Thesis (To be published), Eindhoven University of Technology (1988).

[6] **D. de Bruyn et al.**, Microchannel Plate Report Chapter 3: The FOM charge division method, ed. H. Kersten, Amsterdam (1983).

[7] **W.M. Dijkstra**, Internal Report FIV 85-10, Eindhoven University of Technology (1985).

[8] **C.L.C.M. Knibbeler**, Internal Report LEIS memo 21, Eindhoven University of Technology (1985).

[9] **F.C. v. Nijmweegen**, Internal Report FIV/CO 79-10, Eindhoven University of Technology (1979).

Chapter 8. EARISS First Results.

8.1 *Introduction*

As we have discussed in the last few chapters a lot of problems were encountered during the operation of the EARISS apparatus. The three major difficulties, electrical discharges through the channel plates, and the problems of radio frequency interference in the analog electrical circuit and the grounding of the ground strip, were solved.

We started our measurements using a Ne^+ ion beam with a primary energy of 2 keV. Beam intensities usually varied between 30 and 50 nA, depending on the focussing properties of the electrostatical lenses and the deflection along the beam line. We took a platinum sample (polycrystalline foil). This sample does not contain measurable amounts of other elements.

From equation (2.1) we expect a final energy E_f for 2 keV Ne^+ ions backscattered from Pt of E_f = 1.04 keV. Our first objective was to detect counts from backscattered ions arriving at the second microchannel plate (MCP). The result was shown earlier in figure 4.8. We were able to detect countrates of up to $3.8 \cdot 10^5$ counts per second with a background countrate of 80 counts per second from spontaneous pulses in the MCP's.

The width of the energy window on the first channel plate was calculated to be 12 % of the analyzer pass energy. We chose a pass energy of 4 keV, meaning the ions entering the analyzer with energies between 3760 eV and 4240 eV will arrive on the first MCP. Thus the width of the window is 480 eV. From figure 4.8 we observe that the detected peak is 560 eV wide. This extra width is caused by the convolution of the analyzer window and energy spread of the backscattered ions. A rough estimate of this energy spread in the backscattered ions is thus calculated to be 560-480 = 80 eV. This energy spread is caused by the energy spread in the primary ion beam, by the scattering process and by analyzer imperfections. These processes add up to this estimated energy spread of 80 eV.

At this time we can start looking at the collected charges on the E- and φ-strips. We would like to detect an energy dependence if we vary the accelerating potential V_3 of the zoomlens and we would like

to see an azimuthal dependence if we close the second slit in front of the analyzer. This slit has two openings used for mounting the inner part of the analyzer (figure 8.1, §3.4.). These openings should also

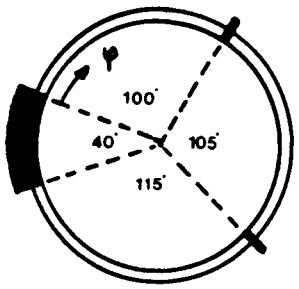

Fig. 8.1. The second slit in the analyzer. The unused part of 40° and the two openings of 2° are shown.

be visible in the azimuthal spectrum. They can be used as a reference since their position is known. In this chapter we will discuss some of the effects mentioned above.

8.2 *Energy and azimuthal dependencies*

In the first stage of our work we recorded several spectra, of which some characteristic examples are shown an figure 8.2.a,b. All spectra showed a broad distribution in the azimuthal direction (70 channels out of 101) and a much narrower distribution in the energy

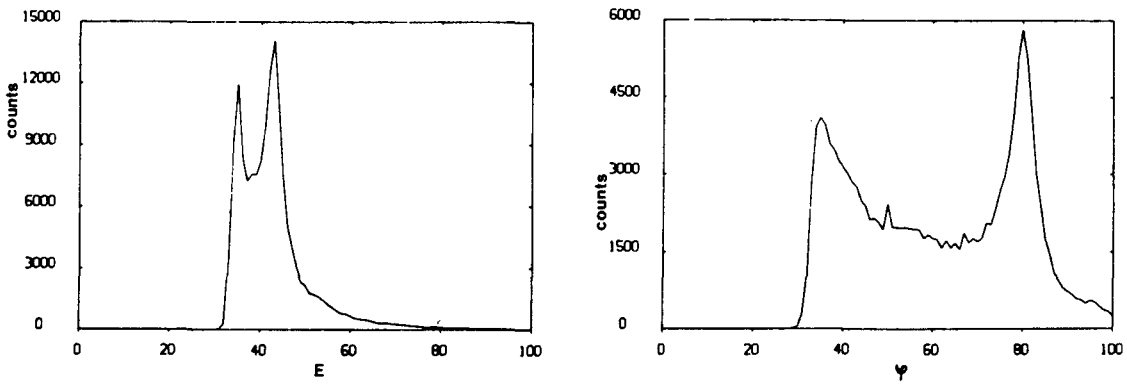

Fig. 8.2.a,b. The energy (a) and azimuthal (b) distribution in the MCA memory.

direction (30 channels out of 101). Both the energy and the azimuthal spectrum showed rather sharp peaks at the edges of their distribution.

We thought that this effect was caused by cross-talk: a higher pulse on the energy strips causes automatically a higher pulse to be detected on the azimuthal strips. This vision was supported by the calculation of the correlation coefficients: the correlation between energy and azimuthal pulses would typically lie around 0.85 to 0.95, thus indicating that Q_E/Q_T and Q_φ/Q_T showed a strong coupling. This coupling was also demonstrated in another way. When the sample was tilted, the effect of this could be seen in the azimuthal spectrum. However the tilting could also be observed in the energy spectrum in which it behaved in exactly the same way.

Another observation was done when the potential V_3 on the last part of the zoomlens was decreased. We would have expected that the energy peak in shifts to the right. However we observed that the peak shifted in the opposite direction: to the left. Part of this shift could also be observed in the azimuthal spectrum, however the effect was not very clear.

The cross-talk was then thought to originate in the electrical circuit. We discovered that the delay lines between main amplifiers and ADC's caused cross-talk and that the ground capacitor for the ground strips should be kept large compared to the capacitance between the E (or φ) strips and the ground strips. It turned out that this capacitor should also have a very low inductance. Although these discoveries gave us more insight in the electrical characteristics and the dynamic behavior of charge collector and preamplifier circuit, we were not able to reduce the correlation between the angular and energy spectra. All aforementioned effects could still be observed.

At this point we started realising that this so called cross-talk could also be caused by a defect in Q_T, since Q_T is an essential signal for determining Q_E/Q_T and Q_φ/Q_T. This would would mean that the Q_T measured on the second microchannel plate (MCP), which we use to normalize our collector charges, is not a good representation of the number of electrons actually arriving on the collector.

There are several ways in which the charge cloud emitted from the second MCP can be distorted on its way to the collector. Firstly inhomogeneous or radial electrical fields between the second MCP and the collector can deflect the electrons in the charge cloud from a

straight path. This means that the point of impact of the electron cloud on the collector does not correspond linearly with the point of origin on the second MCP.

Secondly the situation can occur in which the charge cloud becomes larger than the collector size, which means that the charge cloud expands too much. Part of the cloud will then be deposited onto the conducting layers or onto the collector holder (fig. 8.3.a). This

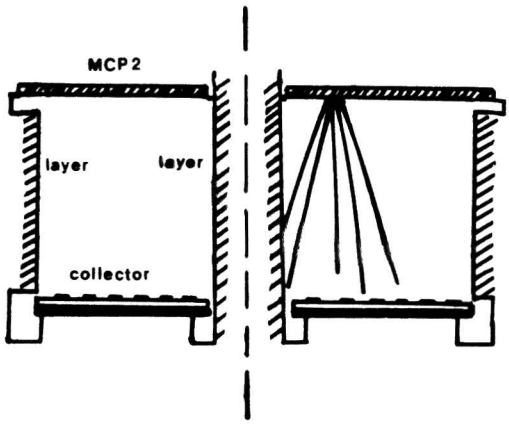

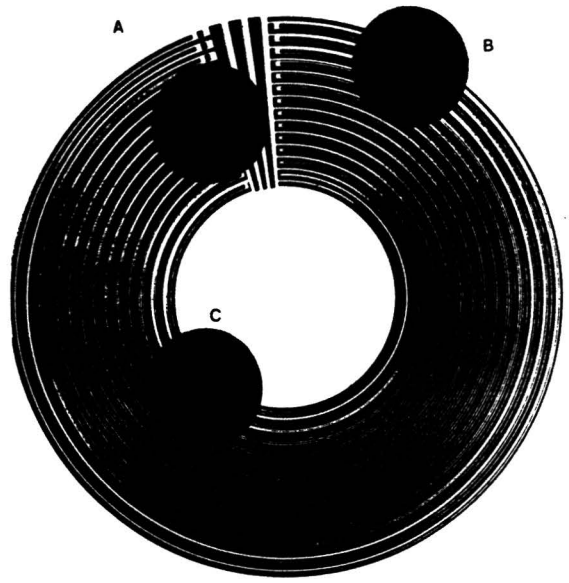

Fig. 8.3.a. Too large electron clouds will lose electrons to the conducting layers and the collector holder.

Fig. 8.3.b. Charge clouds which fall on the marked positions will result in a false detection of their point of impact.

means that we divide Q_E and Q_φ by the wrong number since we divide by Q_T which is the number of electrons leaving the second MCP and not the number arriving on the collector (fig. 8.3.b). This explanation accounts for the energy peak moving in the wrong direction: if the ions are deposited closer and closer to the edge of the MCP, more and more electrons of the charge cloud escaping from the second MCP will be lost in the conducting layers on their way to the collector. This means that although the energy strips become relatively larger near the outer edge of the collector, we start losing so much of the electron cloud that we start dividing by a Q_T which is much larger than the number of electrons actually arriving at the collector. The

result is that the answer to the division becomes smaller, instead of becoming larger as we would have expected. The energy peak will shift in the opposite direction as the one we expected.

In the azimuthal direction however, the collector strips are quite long. Even if the charge cloud is larger than the radial dimensions of the collector, we would still be able to observe a rather broad azimuthal distribution.

The solution the problem of a too large radius of the charge cloud is to increase the voltage across the gap between the second MCP and the collector, thereby giving the charge cloud less time to expand (§4.4 and §5.2). This was tried. We increased the voltage across the conducting layers between the second MCP and the collector to the maximum voltage we could achieve, which is about 500 V. According to equation (4.13) we can calculate the 1/e radius of the electron cloud to be 1.0 to 1.8 mm. This is still a factor 2 larger than the desired cloud size.

Increasing the voltage across the conducting layers significantly improved our spectra. Some results will be discussed in the next section. It is appropriate at this point to mention that we did obtain an energy shift in the right direction.

If we take the problems mentioned above into account, the detection system can be tested in the following way:

In order to test the energy dependence we could image the peak of Ne^+ ions scattered from our Pt sample onto the center of the first MCP by selecting the right accelerating potential V_3 on the zoomlens at the chosen analyzer pass energy. By taking a larger or smaller accelerating potential we are able to scan this peak across the surface of the first MCP. At larger accelerating potentials we start imaging other parts of the energy spectrum onto the first MCP. Sputtered ions are emitted from a surface with energies up to a few hundred eV. Taking V_3 to be near the pass energy of the analyzer will image those sputtered ions onto the first MCP. Since the energy spread of these ions is rather large (also in the range of a few hundred eV) we have a way of imaging a more or less homogeneous energy distribution on our detection system. This should result in an equally

homogeneous energy distribution measured on our collector.

The azimuthal dependence was tested by closing and opening the second slit (fig. 8.1, fig. 3.3). If all inhomogeneities would have been corrected for we would expect a rectangular azimuthal spectrum when the slits are open. When we close the second slit, only the two openings should be observed on the detector. If we open the second slit slightly we should observe the same two peaks an a homogeneous rectangular background. This azimuthal spectrum should also be independent of the energy of the detected ions.

8.3 *EARISS spectra*

In this section we will discuss some aspects of the collected EARISS spectra using different photographs and prints of the collected data.

We used 2 keV Ne^+ ions scattered from a Pt polycrystalline surface. The scattered ions have an energy of about 1 keV. They are postaccelerated in the zoomlens to 4 keV. After they have passed the analyzer (which was set to a 4 keV pass energy) they are focussed onto the first MCP. At that point their energy spread is about 2 % of the analyzer pass energy, as we have estimated in section 8.1. These incident ions are detected and the radial and azimuthal distribution is collected in the MCA memory.

In figure 8.4 we present a three dimensional picture of the collected counts in the MCA memory. One axis shows the energy channels containing the distribution of Q_E/Q_T. The other axis shows the azimuthal channels containing the distribution of Q_φ/Q_T. The vertical axis represents the number collected counts.

Several aspects of the detection system can be seen in figure 8.4. The collected counts show up as a steep ridge. This ridge stretches in the direction from channel 10 to channel 40. In the azimuthal direction it stretches from channel 10 to about channel 90. The ridge is not perpendicular to the energy axis. This is presumably caused by cross-talk between the Q_E and the Q_φ pulses or by the size of the charge cloud still being too large. Furthermore we see that the number of collected counts is not homogeneously distributed over the ridge. We observe two peaks, one at each end of the ridge. These peaks may be

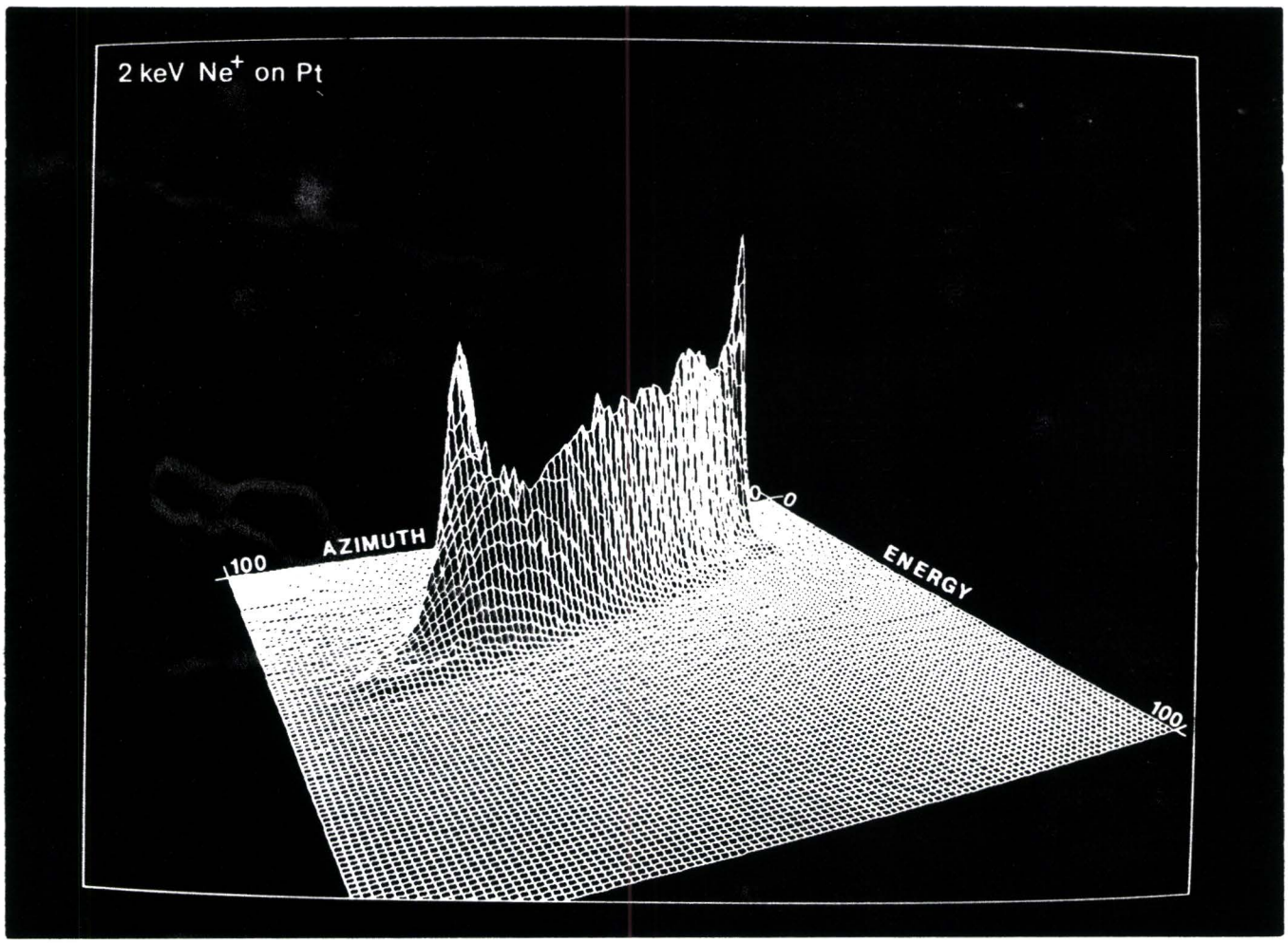

Fig. 8.4. Three dimensional picture of the counts collected in the MCA memory.

caused by electron clouds falling on the strips meant for interconnecting all rings and sickles located in the unused part of the charge collector (fig. 5.3.b and fig. 8.3.b).

In figure 8.5. we have shown a height map of the same kind of ridge as we showed in figure 8.4. The color in this map represents the number of accumulated counts in the MCA memory. From this figure we see that the aforementioned ridge is not a straight line, but it is slightly bent to the left at higher energy channels. At the lowest energy channels we observe the ridge to be very slightly bent to the right, thus causing the ridge to have a very slight S-shape. A possible solution for this observation is that the ring of ions inpinging on the first MCP is projected slightly off axis on the

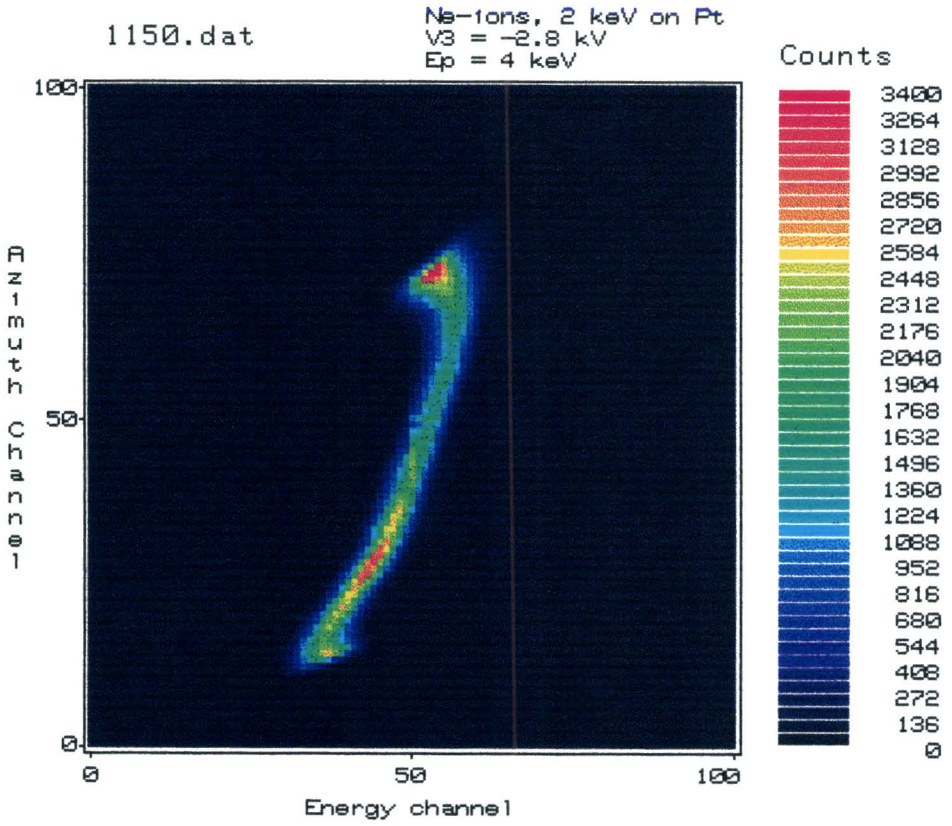
1150.dat
Ne-ions, 2 keV on Pt
V3 = -2.8 kV
Ep = 4 keV
Counts
3400
3264
3128
2992
2856
2720
2584
2448
2312
2176
2040
1904
1768
1632
1496
1360
1224
1088
952
816
680
544
408
272
136
0
Azimuth Channel
100
50
0
0
50
100
Energy channel

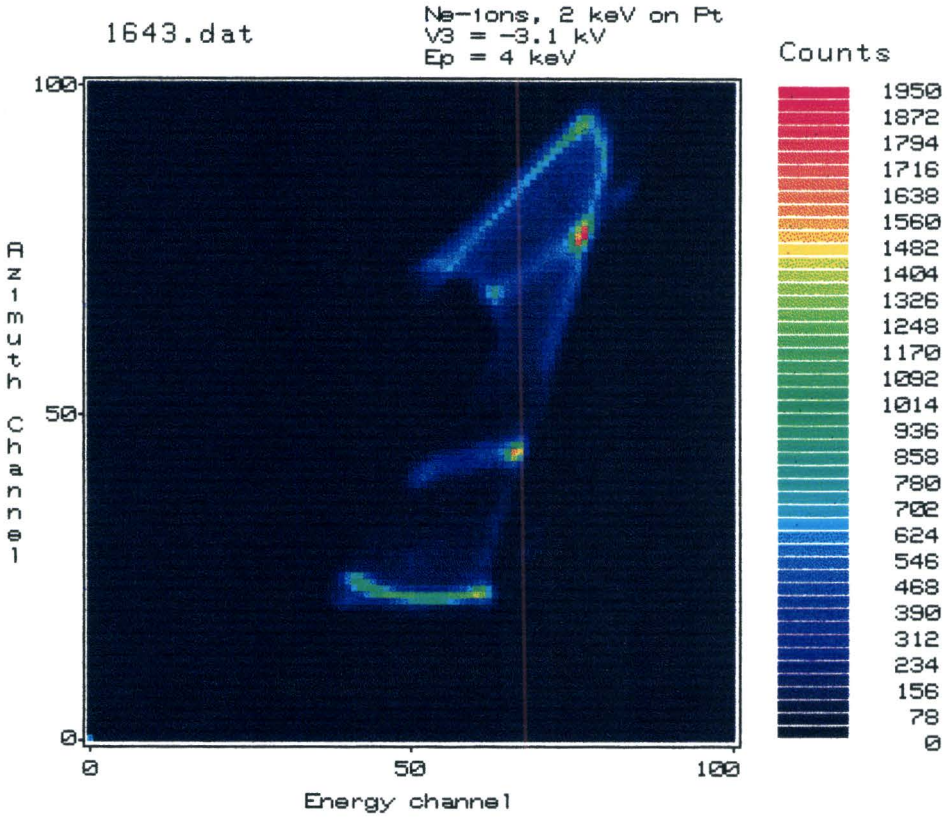
1643.dat
Ne-ions, 2 keV on Pt
V3 = -3.1 kV
Ep = 4 keV
Counts
1950
1872
1794
1716
1638
1560
1482
1404
1326
1248
1170
1092
1014
936
858
780
702
624
546
468
390
312
234
156
78
0
Azimuth Channel
100
50
0
0
50
100
Energy channel

Fig. 8.5. (Previous page) Height map of the counts collected in the MCA memory with a homogeneous energy distribution over all azimuthal angles.

Fig. 8.10. (Previous page) Height map of the counts collected in the MCA memory with the second slit slightly opened and a broad energy distribution.

charge collector (fig. 8.6). A numerical simulation has shown that this lateral shift can cause an S-shape in the detected signals. A possible cause for this off-axis projection is the 13^{o} angle which the channels of the second MCP have with respect to the surface normal. It

Fig. 8.6. The projection of the electron clouds on the collector is slightly off axis. This can cause an S-shape in the spectra.

is plausible that the escaping electron clouds gets a velocity component parallel to the MCP surface because of this angle. Due to this velocity component the point of impact of the electron cloud on the charge collector is shifted laterally with respect to its point of origin on the second MCP. Since all MCP channels are parallel this would account for the slightly off-axis projection of the ring of inpinging ions. This effect could thus cause the S-shape detected in the ridge. The effect could also be present if the electrical field between the second MCP and the collector has a lateral component. Such

a field could cause the same kind of lateral deviations of the electrons in the cloud.

Our next objective is to show that a correct energy shift is observed when the accelerating voltage V_3 is varied. Several collected spectra at different voltages are shown in figure 8.7.(a, b, c, d, e, f, g, h)

Starting from the upper left of figure 8.7. (picture a) we have increased the voltage on the zoomlens in 100 V steps from -2.2 kV to -3.2 kV (picture h). Each picture is scaled to its maximum number of counts.

At -2.2 kV we observe a rather homogeneous distribution of counts over the whole collector area. The counts observed in this picture can be attributed to the neutrals we observed earlier (§4.2) due to analyzer imperfections. These neutrals have a more or less homogeneous distribution over the first channel plate, which means that we detect impacts from the entire detector.

The shape of picture (a) demonstrates that the rectangle we would have expected is distorted. At the right we observe a rather straight edge but at the left there seems to be part of the detector where no incident particles are detected. The upper edge is tilted to an angle of nearly 35^{o} with respect to the lower edge. These distortions are probably caused by a distorted electrical field in the gap between the second MCP and the collector. This distorted field could be caused by the conducting layers in this gap. Later, we discovered that the conducting layers at the inner edge of this gap differed from those at the outer edge (fig. 3.5). This means that the voltage drop in the region between the second MCP and the collector is different for the inner and the outer conducting layers. The electrical field in this region will thus be inhomogeneous. A radial component will be present. The electrons leaving the second MCP have a low velocity. Even a small electrical field at this point could cause large deflections in the electron trajectories. An inhomogeneous electrical field near the collector would not be able to cause such large deflections since the electron velocities at that point are much larger.

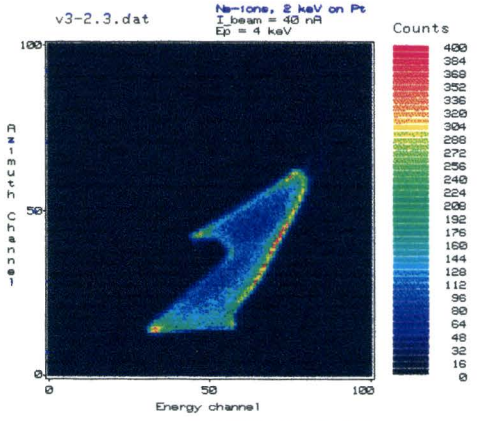
v3-2.3.dat
Ne-ions, 2 keV on Pt
I_beam = 40 nA
Ep = 4 keV
Counts
400
384
368
352
336
320
304
288
272
256
240
224
208
192
176
160
144
128
112
96
80
64
48
32
16
0
Energy channel
0
50
100

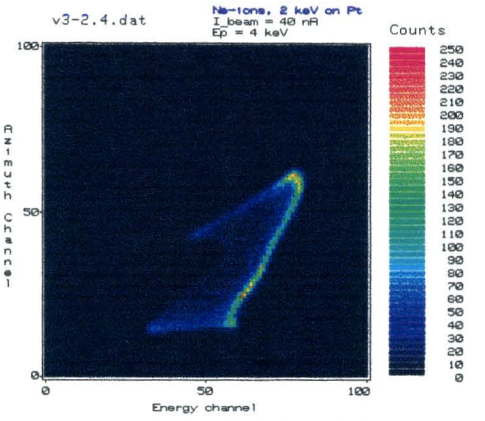
v3-2.4.dat
Ne-ions, 2 keV on Pt
I_beam = 40 nA
Ep = 4 keV
Counts
250
240
230
220
210
200
190
180
170
160
150
140
130
120
110
100
90
80
70
60
50
40
30
20
10
0
Energy channel
0
50
100

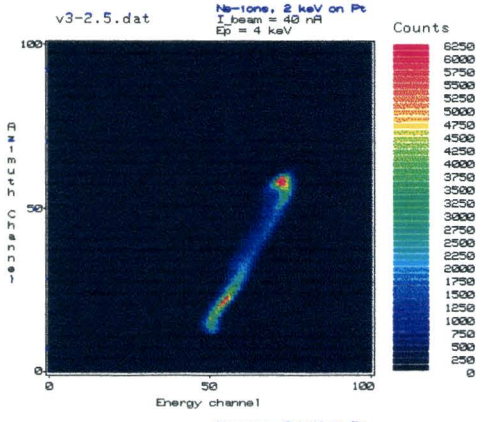
v3-2.5.dat
Ne-ions, 2 keV on Pt
I_beam = 40 nA
Ep = 4 keV
Counts
6250
6000
5750
5500
5250
5000
4750
4500
4250
4000
3750
3500
3250
3000
2750
2500
2250
2000
1750
1500
1250
1000
750
500
250
0
Energy channel
0
50
100

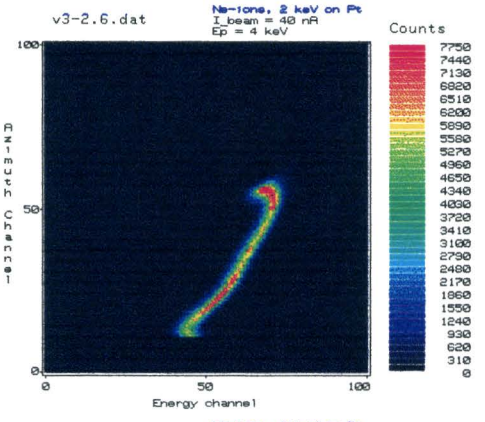
v3-2.6.dat
Ne-ions, 2 keV on Pt
I_beam = 40 nA
Ep = 4 keV
Counts
7750
7440
7130
6820
6510
6200
5890
5580
5270
4960
4650
4340
4030
3720
3410
3100
2790
2480
2170
1860
1550
1240
930
620
310
0
Energy channel
0
50
100

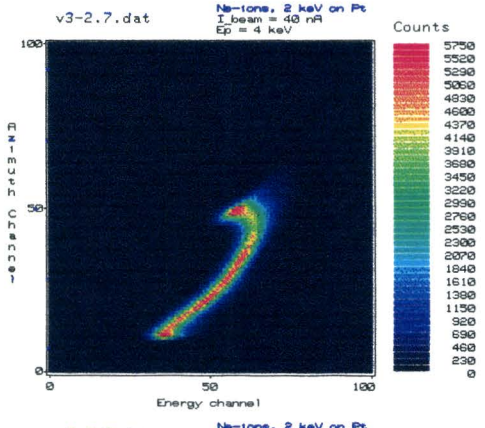
v3-2.7.dat
Ne-ions, 2 keV on Pt
I_beam = 40 nA
Ep = 4 keV
Counts
5750
5520
5290
5060
4830
4600
4370
4140
3910
3680
3450
3220
2990
2760
2530
2300
2070
1840
1610
1380
1150
920
690
460
230
0
Energy channel
0
50
100

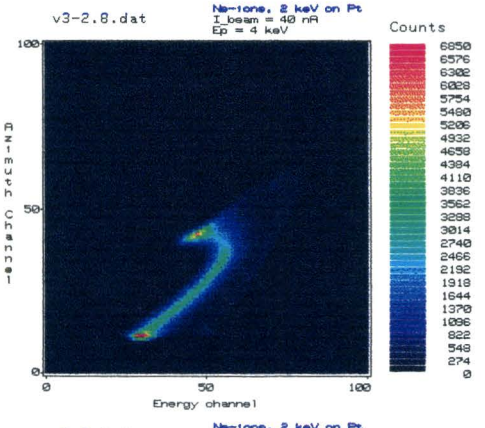
v3-2.8.dat
Ne-ions, 2 keV on Pt
I_beam = 40 nA
Ep = 4 keV
Counts
6850
6576
6302
6028
5754
5480
5206
4932
4658
4384
4110
3836
3562
3288
3014
2740
2466
2192
1918
1644
1370
1096
822
548
274
0
Energy channel
0
50
100

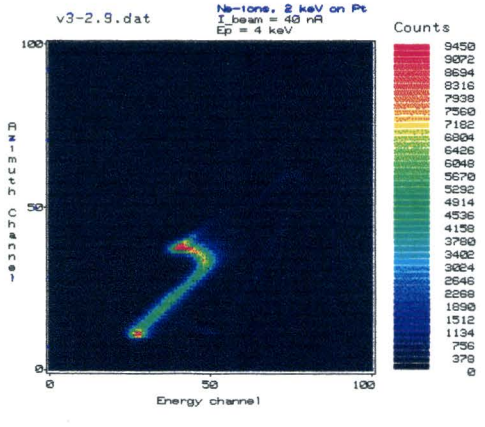
v3-2.9.dat
Ne-ions, 2 keV on Pt
I_beam = 40 nA
Ep = 4 keV
Counts
9450
9072
8694
8316
7938
7560
7182
6804
6426
6048
5670
5292
4914
4536
4158
3780
3402
3024
2646
2268
1890
1512
1134
756
378
0
Energy channel
0
50
100

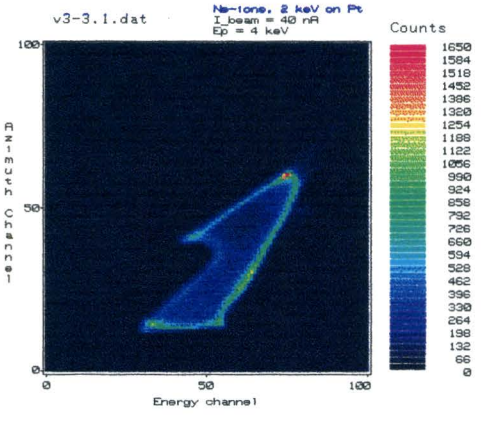
v3-3.1.dat
Ne-ions, 2 keV on Pt
I_beam = 40 nA
Ep = 4 keV
Counts
1650
1584
1518
1452
1386
1320
1254
1188
1122
1056
990
924
858
792
726
660
594
528
462
396
330
264
198
132
66
0
Energy channel
0
50
100

Fig. 8.7. (Previous page) The collected EARISS spectra at different settings of the acceleration potential on the zoomlens. For a further explanation see text.

When we start increasing the accelerating voltage, we see that the right edge of the active area receives more counts. The background seems to be disappearing because each picture is scaled with respect to the maximum number of counts. At an accelerating voltage V_3 = -2.4 kV we start seeing the same ridge we observed earlier in figure 8.4. This is an indication that the ions backscattered from the Pt surface are now imaged at the outer edge of the first MCP (compare with figure 4.8). Increasing the accelerating voltage shows that the ridge starts moving to the left in the MCA memory. This is in agreement with the shift we were expecting to observe. Each 100 V step in the voltage causes the ridge to shift approximately over 10 channels to the left. The shifting stops at an acceleration voltage of -2.9 kV (picture g). At this point the ridge is at the left edge of the active area of the collector. The upper part of the ridge at this point shows a strong bending to the left. The last picture (h) again shows the whole active detector area. The overall number of collected counts is much lower than in the previous picture, thus indicating that we are starting to observe sputtered ions (fig. 4.8). These sputtered ions also cause the right edge of the detector to receive more counts.

From this series of pictures we can conclude firstly that the energy dependence can be observed, and secondly that the shift is in the right direction. Within the resolution we can reach at this moment the observed shifts are linear over the whole detector range.

Another experiment we did was to close the second slit. The scattered ions can pass through two openings in this slit. This will yield two very narrow spots of ions imaged on the first MCP. The resulting peaks on the charge collector are shown in figure 8.8. As we can see in this figure, the two peaks are just a few channels wide in both the energy and the azimuthal direction.

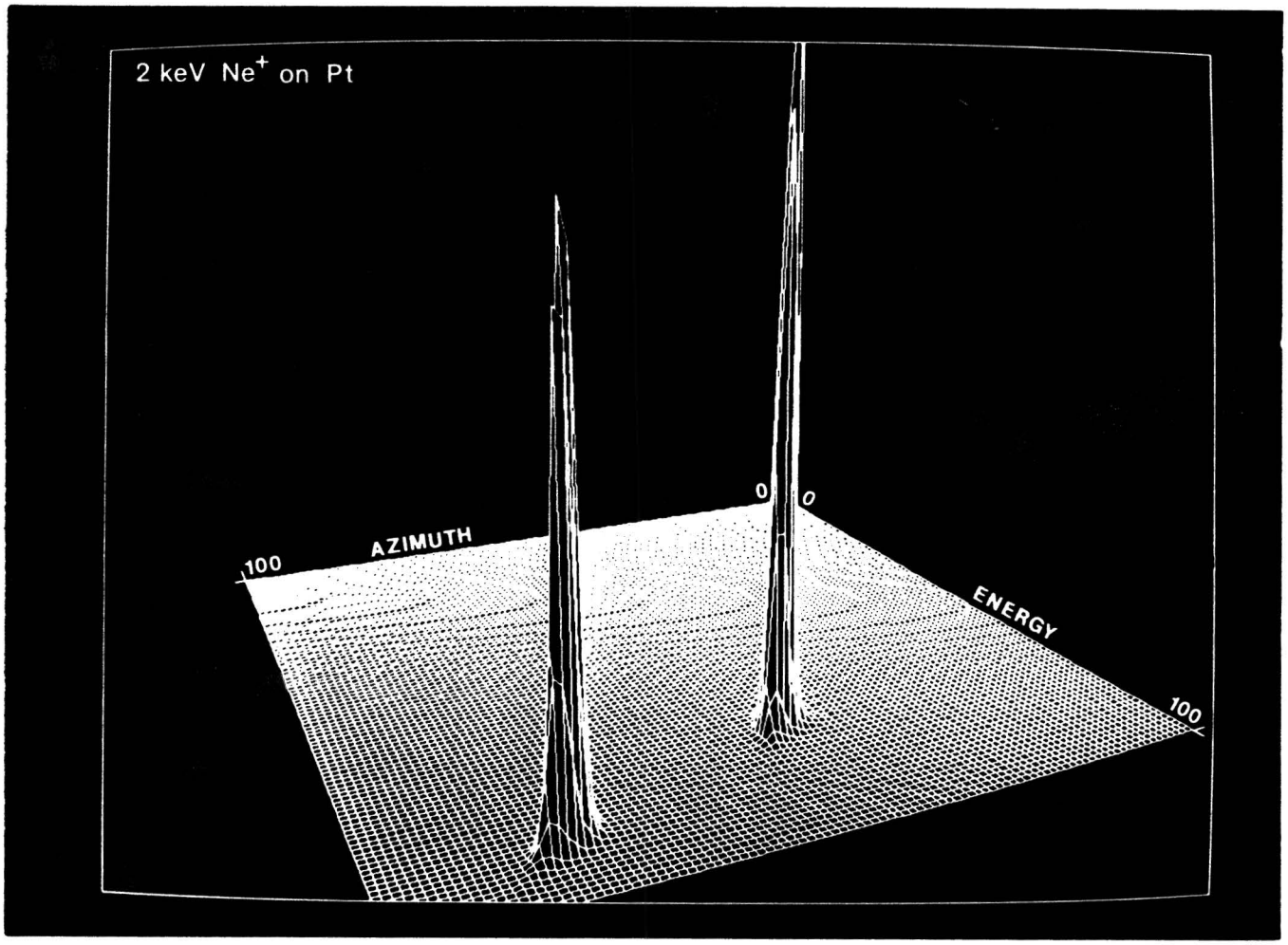

Fig. 8.8. Image of the two openings in the second slit from the collected counts in the MCA memory.

We have seen earlier that the detected energies on the collector range over about 30 channels in the MCA memory. This should correspond to a 480 eV range on the first MCP. The energy spread of the backscattered ions on the first MCP was estimated to be about 80 eV. From the above we can conclude that this would amount ot about 6 channels spread in the MCA memory. This is in close agreement with the width of the two peaks of figure 8.8 in the energy direction.

The openings in the second slit are only 2^{o} wide. The total opening azimuth of the analyzer is 320^{o}. We have seen that the azimuthal range in the MCA memory is roughly about 90 channels. Therefore the azimuthal spread of the imaged peaks in the MCA memory is estimated to be half a channel. From figure 8.8 we see that the

actual spread in the MCA memory is much larger, about 6 channels. The extra width is likely due to spiralling ion paths in the analyzer. This is quite possible since the azimuth selector which should eliminate such paths is not yet installed.

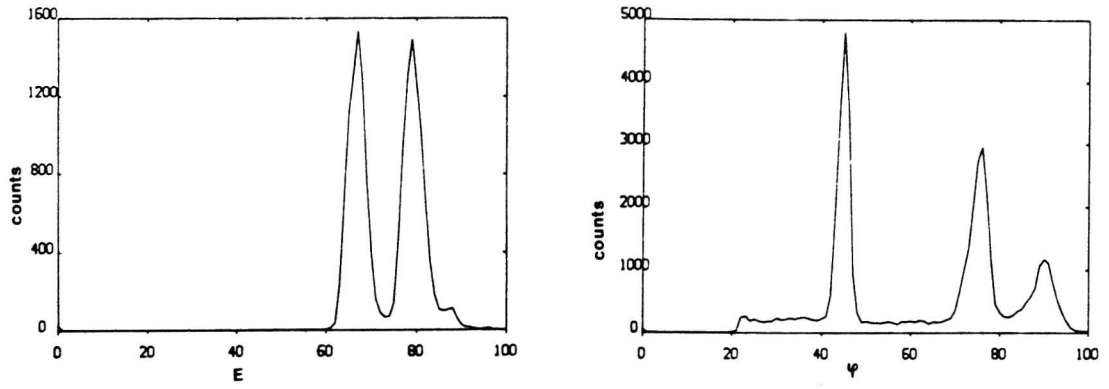

Fig. 8.9.a. Energy distribution of the collected counts with the second slit nearly closed.

Fig. 8.9.b. Azimuthal distribution of the collected counts with the second slit nearly closed.

If we start opening the second slit slightly we can see the other angles coming into view in the spectra (fig 8.9.a,b). We also observe some increase of the number of counts near the edge of azimuthal range, especially at large azimuthal angles.

From figure 8.8 and figure 8.9.b we can see clearly that although the two peaks resulting from the two openings in the detector should have been caused by ions with the same energy, the two spots on the collector are not detected at the same energy channel. This is again probably due to the cross-talk or to the size of the electron cloud.

We change the accelerating voltage to -3.1 kV. At this setting we start detecting sputtered ions as we discussed above. This means that we image a homogeneous energy distribution onto the first channel plate. But since the second slit is nearly closed we observe mostly those ions passing through the two openings and those ions close to the edge of the analyzer azimuthal range (0^{o} and 320^{o}, Fig. 8.3.a). The rest of the detector area shows a rather homogeneous energy distribution. From figure 8.10 (below fig. 8.5) we see that there is not much distortion at the lower edge of the detector area: the energy

ranges from channels 35-40 to channels 60-65 with almost no increase in the azimuthal direction, indicating a low cross-talk. At larger azimuthal channels we observe that the cross-talk increases since the azimuth increases with increasing energy. The lines of equal azimuth are tilted up to 35^{o} with respect to the lower lines of equal azimuth.

The azimuthal angle between the two openings in the second slit is 105^{o} (fig. 8.3.a). As we can see from figure 8.10, this corresponds to about 35 channels in the azimuthal direction in the MCA memory. The angle between the first opening in the slit and the lower edge of the analyzer range is 115^{o}. The above leads us to believe that this would correspond to about 38 channels in the MCA memory. However we observe in figure 8.10 that the lower edge of the area is separated about 25 channels from the first opening. It seems that the lower edge is compressed. Low azimuthal angles do not occur. The same holds for the upper edge of the analyzer range: this edge is spaced 100^{o} from the second opening, which should be about 33 channels in the MCA memory. The observed number of channels between the second opening and the upper edge is about 20 channels, which means that the upper part of the detector area also seems to be compressed.

In the next chapter we will summarize the conclusions from the measurements presented above and discuss some of the possibilities for improving the detection system.

9. Concluding Remarks.

In this thesis we have demonstrated that the EARISS apparatus is able to detect and process up to $4 \cdot 10^5$ backscattered ions per second. The energy and the azimuth of each backscattered ion can be determined simultaneously. The energy and azimuthal dependence have been observed in the first spectra, although some distortions still exist.

A large part of this work dealt with the problems we encountered during the first experiments with the EARISS apparatus. We have reduced the high frequency interference to an acceptable level. Furthermore we have found a way of operating the chevron construction of microchannel plates in a space charge saturated mode. Thereafter we have discovered that the size of the charge cloud arriving on the collector is still too large.

Some suggestions concerning further improvements of the EARISS detector will be discussed in this chapter. We will distinguish improvements that can be made in the detector assembly, in the electronic circuit and in the divider and the multichannel analyzer memories.

9.1 *Detector assembly*

The most important result of our experiments is that the distance between the second microchannel plate (MCP) and the charge collector should be reduced. We suggest to reduce this distance of about 7 mm. This will result in a charge cloud diameter of about 1.4 to 2.4 mm (1/e radius of 0.7 to 1.2 mm) on the charge collector at a 200 V accelerating voltage.

Another possible change in the detector assembly is related to the conducting layers. Care should be taken that the electrical field between the second MCP and the collector is absolutely homogeneous with an emphasis on the region close the MCP. The radial field strength should be kept at least two orders of magnitude smaller than the axial field strength in order to prevent distortions in the image. Therefore, we suggest to make the distance between the top of the conducting layers and the back of the second MCP as short as possible, thereby reducing the effect of fringing fields.

A third suggestion is to disconnect these conducting layers from the ground strips and the holder of the collector. This connection could then be made outside the vacuum system which would improve the flexibility of the experiments meant to get insight in the grounding of the collector.

The neon discharge tube that protects the goldplated ring between the two MCP's could be placed outside the vacuum system. The disadvantage of this change would be that when a discharge occurs it will take about 4 ns extra time for the neon tube to react. An important advantage would be that a more reliable kind of neon discharge tube can be used.

We would again like to emphasize that two collectors, which are each others mirror image, are in use. Care should be taken not to confuse the E- and φ-strips.

9.2 *Analog circuit*

The grounding capacitor should have a capacitance of at least 20 nF. Due to the inductance of such capacitors the grounding is not optimal. This caused the distortions in the pulses measured from the E- and φ-strips. A better capacitor should be sought with a low inductance. This capacitor has to be placed as close to the collector as possible. The connecting wire should have a very low inductance; a copper strip could probably be used. It is important to gain more insight in the behaviour of the ground strip at high frequencies. Attention should also be paid to the way in which the deposited charges are fed into the preamplifiers. Furthermore, the way in which the preamplifiers charge their input capacitances influences the distribution of charges. More insight in the dynamic characteristics (especially the dynamic capacitance) of the preamplifiers should be obtained.

A suggestion would be to connect the ground strips to a third preamplifier. This would mean that the capacitance to ground of each strip is exactly the same, and remains the same during the transfer of the collected charges to the preamplifiers. This would mean that charge shifts through the detector capacitances would be kept to a minimum. This test would require the disconnection of the collector

holder from the conducting layers, which is the reason why this experiment has not yet been done.

9.3 *Digital circuit*

In chapter 7 we have discussed the effects which occur during an integer division. The analog to digital converters (ADC's) we use at this moment need adjustment. Furthermore it could be worthwhile to use 10 bit ADC's. This would increase the dynamic range of the dividers. It would then be necessary to use 1 MB divider memories. However, the multichannel analyzer would not require adjustments since the divider outputs would still be 8 bits numbers. Another improvement would then be to accumulate simultaneously the pulse height distribution of Q_T. This would yield a correction factor for each divider row and the inhomogeneities in the divider output could be corrected for.